KLOE Note 204

Measurements of the Absolute Branching Ratios for Dominant K_L Decays, the K_L Lifetime, and V_{us} with the KLOE Detector

M. Antonelli [a], P. Beltrame [b], M. Dreucci [a], M. Moulson [a], M. Palutan [a], A. Sibidanov [a,c]

[a] *Laboratori Nazionali di Frascati dell'INFN, Frascati, Italy.*

[b] *Institut für Experimentelle Kernphysik, Universität Karlsruhe, Germany.*

[c] *Permanent address: Budker Institute of Nuclear Physics, Novosibirsk, Russia*

Abstract

From a sample of about 10^9 ϕ mesons produced at DAΦNE, we have selected K_L mesons tagged by observing $K_S \to \pi^+\pi^-$ decays. We present results on the major K_L branching ratios, including those of the semileptonic decays needed for the determination of $|V_{us}|$. A measurement of the K_L lifetime is also given.

1 Introduction

In the following, we describe the measurement of the absolute branching ratios for K_L decays to $\pi^\pm e^\mp \nu$, $\pi^\pm \mu^\mp \nu$, $\pi^+\pi^-\pi^0$, and $\pi^0\pi^0\pi^0$. These branching ratios are fundamental experimental parameters used to determine the CKM matrix element $|V_{us}|$. There are no good measurements of the absolute values of these branching ratios; at present, the PDG "fit" values for these branching ratios have 0.5–2% relative errors, and are obtained from various measurements of K_L branching ratios and rates [1]. Recent analyses from KTeV [2] and NA48 [3] of the relative branching ratios for dominant K_L decays have shown discrepancies with respect to the PDG values of up to 8% depending on the channel.

2 Measurement of absolute branching ratios

The measurement of the absolute K_L branching fractions is a unique possibility of the ϕ factory. A pure sample of nearly monochromatic[1] K_L's can be selected by identification of K_S decays. The absolute K_L branching ratios can be determined using a sample of tagged K_L events by counting the fraction of K_L decays in each channel and correcting for acceptances, reconstruction efficiencies and background. However, the tagging procedure is not perfect, because the tagging efficiency depends slightly on the evolution of the K_L. We include events in which the K_L interacts in the calorimeter, escapes the detector, or decays to any final state. The difference in tagging efficiency in each case depends on the tagging algorithm; the minimization of such differences is used to optimize the tagging criteria. To correct for this effect, we define the *tag bias* for the detection of K_L decays to a final state k as the ratio of the tagging efficiency for $K_L \rightarrow k$ in the fiducial volume to the overall tagging efficiency, determined without regard to the evolution of the K_L. The tag bias for channel k is thus $\varepsilon_{\text{tag}_k} / \varepsilon_{\text{tag}_\text{tot}}$, and

$$\text{BR}(K_L \rightarrow k) = \frac{N_k}{\varepsilon_{\text{tag}k}/\varepsilon_{\text{tag}_\text{tot}}\, N_\text{tag}\, \varepsilon_\text{FV}\, \varepsilon_{\text{rec}k}}, \tag{1}$$

where N_k is the number of K_L decays to k, N_tag is the number of tagged K_L's, ε_FV is the geometrical efficiency of the fiducial volume, and $\varepsilon_{\text{rec}k}$ is the reconstruction efficiency.

Knowledge of the K_L lifetime $\tau(K_L)$ is very important not only for the determination of $|V_{us}|$, but is also necessary for the measurement of the absolute branching ratios. $\tau(K_L)$ can be obtained from the K_L proper time distribution and also, with better accuracy, by measuring all K_L decay branching ratios in a given fiducial volume (FV) and requiring they sum to unity. Results obtained using the second method will be given.

3 Data and Monte Carlo samples

For the analysis presented, we have used all data collected by KLOE at DAΦNE during the years 2001 and 2002 satisfying the basic data-quality criteria described in the following. This data set corresponds to an integrated luminosity of about 328 pb^{-1}.

Runs were first arranged into groups with consistent values of $\sqrt{s}$. An attempt was made to ensure sufficient statistics in each group. When an isolated run with

[1] ϕ mesons at DAΦNE are produced nearly at rest with a small horizontal momentum of about 12 MeV.

a value of $\sqrt{s}$ very different from that of the other members of the run group was found, it was rejected. Cuts on the integrated luminosity for each group were then applied; only groups with more than about 20 nb^{-}1 were retained. The formation of run groups is illustrated in Fig. 1.

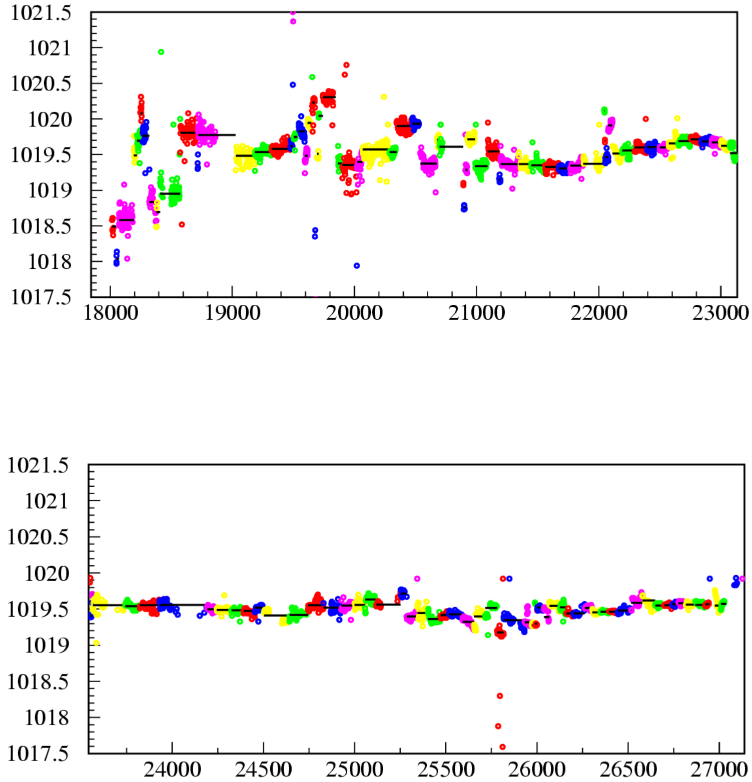

Fig. 1. Values of $\sqrt{s}$ for 2001–2002 runs. Colors indicate different run groups used for the analysis. Black lines indicate mean $\sqrt{s}$ values for each group.

Each run in the data set is further required to have been simulated using the standard KLOE Monte Carlo production procedure, in which individual runs are simulated [4] A set of requirements is also imposed on the kinematics of the e^+e^- system in the initial state, as determined for each run using Bhabha scattering events: the mean y and z components of the total momentum must satisfy $|\mathbf{p}_{\phi\, y,z}| < 3$ MeV; the mean total center-of-mass energy must satisfy $|\sqrt{s} - 1020| < 5$ MeV; the mean position of the luminous point must satisfy $|x| < 3$ cm, $|y| < 3$ cm, and $|z| < 5$ cm; and the spread of the luminous region must satisfy $\sigma_x < 3$ cm and $\sigma_z < 3$ cm, as obtained from the standard deviation of a Gaussian fit. Finally, a small number of runs were eliminated from the data set because the trigger was known to be operating improperly or good timing calibrations were not available.

Each run used in the analysis was simulated with the KLOE Monte Carlo, GEANFI [4], using the known values of the relevant machine parameters such as $\sqrt{s}$ and $\mathbf{p}_\phi$. Machine background from the data set is inserted into Monte Carlo events on a run-by-run basis. The number of events simulated for each run in the data set is equivalent to that expected on the basis of the run luminosity. For this analysis, we use a set of Monte Carlo events consisting of $\phi \to K_S K_L$ decays, with the K_S and K_L decaying in accordance with their natural branching ratios. The effects of initial- and final-state radiation are included in the simulation. In particular, the treatment of final-state radiation in K_S and K_L decays is discussed in Ref. 5. This set of Monte Carlo events provides both signal and background samples for this analysis.

Good runs from the run groups formed as described above, together with the corresponding Monte Carlo runs, were then organized into 14 run periods. For the 2001 data, trigger settings were the determining factor in establishing the boundaries of the run periods. In 2002, trigger conditions were stable, so run periods were divided on the basis of integrated luminosity, each period representing about 25 pb^{-1}. The run periods are listed in Table 1.

The complete branching ratio analysis was performed on the data for each of the 14 run periods; the averages over the 14 periods are used to quote final results. One-fourths of the available data have been used to compute various corrections; the remaining sample has been used for the actual signal counting for the evaluation of the K_L branching ratios.

4 The K_L tag

Candidate events are identified by the presence of a $K_S \to \pi^+\pi^-$ decay. We require a vertex with two tracks of opposite curvature with origins within a cylindrical FV of radius $r_{xy} < 10$ cm and length $\Delta z < 20$ cm, centered on the collision region, as determined for each run using Bhabha events. The two-track invariant mass, calculated assuming the pion mass for both tracks, must be within 5 MeV of m_{K_S}. The magnitude of the total momentum of the two tracks must be within 10 MeV of the value expected from two-body ϕ decay kinematics and the value of $\mathbf{p}_\phi$. If more than one vertex satisfies these criteria, that closest to the nominal ϕ vertex position is identified as the K_S.

The best estimate of the magnitude of the K_S momentum, p_{K_S}, is obtained from the kinematics of the $\phi \to K_S K_L$ decay, using the K_S direction reconstructed from the measured momenta of the $\pi^+\pi^-$ tracks and the known value of $\mathbf{p}_\phi$. This is because the components of the pion track momenta along the K_S line of flight and the opening angle between the pion tracks are somewhat anticorrelated in the reconstruction of the K_S vertex, but this correlation does not affect the accuracy of the determination of the direction of the K_S. Figure 2(a) shows the difference

Run-period	Runs	Integrated luminosity (nb^{-1})
1	19000–20000	19707.9
2	20000–21000	22507.3
3	22382–22828	22647.2
4	22828–23028	11900.5
5	23542–23970	25121.6
6	23970–24381	25196.7
7	24381–24875	24980.1
8	24875–25210	25141.2
9	25210–25535	25164.1
10	25535–25937	25169.3
11	25937–26196	25174.1
12	26196–26497	25210.2
13	26497–26766	25110.6
14	26766–28000	25412.9

Table 1
List of run periods used for the analysis, with beginning and ending runs for each period and the corresponding integrated luminosity.

between the reconstructed value of p_{K_S} and the true value as obtained from Monte Carlo, with $p_{K_S,\mathrm{rec}}$ determined from the both the momenta of the $\pi^+\pi^-$ tracks, $p_{K_S,\mathrm{momenta}}$, and from the K_S direction with respect to the ϕ momentum, $p_{K_S,\mathrm{boost}}$.

The resolution on the K_S momentum obtained with this method is dominated by the beam-energy spread. The value of p_{K_S} is very sensitive to the value of the K_S mass:

$$\frac{\delta P}{P} \sim \frac{1}{\beta^2} \cdot \frac{\delta M}{M}, \tag{2}$$

where β is the kaon velocity. For this reason, we use the KLOE measurement [6] for the value of the K_S mass. Figure 2(b) shows the distribution of $p_{K_S,\mathrm{momenta}} - p_{K_S,\mathrm{boost}}$ obtained using the PDG and KLOE values of the neutral kaon mass. The difference in the mean value of the reconstructed momentum is about 0.6 MeV, in agreement with the formula given above.

The position of the ϕ production point, $\mathbf{x}_\phi$, is determined as the point of closest approach of the K_S momentum, propagated backwards from the K_S vertex, to the beam line. The K_L line of flight is then constructed from the K_L momentum, $\mathbf{p}_{K_L} = \mathbf{p}_\phi - \mathbf{p}_{K_S}$, and the position of the production vertex, $\mathbf{x}_\phi$.

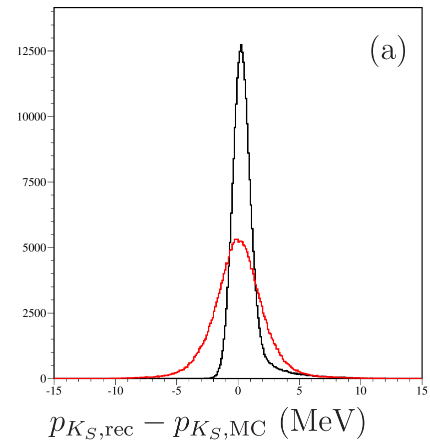

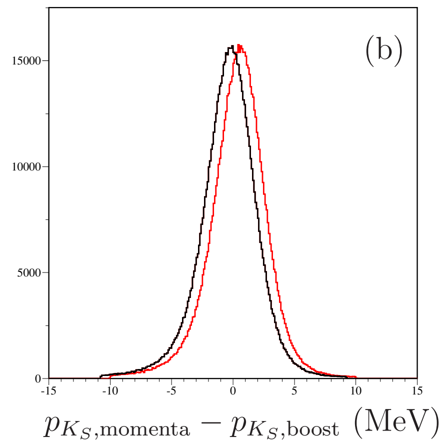

Fig. 2. (a) Distribution of the difference between the reconstructed value of p_{K_S} and the true value as obtained from Monte Carlo, with $p_{K_S,\mathrm{rec}}$ determined from the both the momenta of the $\pi^+\pi^-$ tracks, $p_{K_S,\mathrm{momenta}}$ (solid red line), and from the K_S direction with respect to the ϕ momentum, $p_{K_S,\mathrm{boost}}$ (solid black line). (b) $p_{K_S,\mathrm{momenta}} - p_{K_S,\mathrm{boost}}$ using the value of the neutral kaon mass from the PDG (solid red line) and the value measured by KLOE (solid black line).

4.1 Extrapolation of tracks from K_S decay to the calorimeter

Successful calculation of $\mathbf{p}_{K_L}$ is the minimal requirement for a K_L tag. However, we seek to obtain additional information using the K_L tag: the event t_0, and whether or not the clusters from the K_S unambiguously satisfy the calorimeter trigger.

To determine the event t_0, each of the tracks from the K_S vertex are extrapolated to the calorimeter. The tracks are first organized into "trees," defined as a series of "branches" connected by vertices. If a tree has only one branch, that branch is analytically extrapolated to its first intersection with the calorimeter surface. If a tree has exactly two branches, the extrapolation is performed from the second branch if the topology is identified as a π-μ kink, *i.e.*, if the missing momentum at the vertex is greater than 10 MeV and the squared mass of the secondary track is within 1000 MeV^2 of m_μ^2, calculated assuming the parent particle is a pion and the missing mass is zero. These criteria for the identification of π-μ kinks are justified in Ref. 7. If the tree has two branches and these criteria are not satisfied, or if the tree has more than two branches, the extrapolation is performed from the first branch.

In this analysis, two track-cluster residuals are defined for the purposes of track-to-cluster association: d_{TCA}, the distance from the extrapolated impact point on the calorimeter to the cluster centroid; and $d_{\mathrm{TCA}}^{\perp}$, the component of this distance in the plane transverse to the momentum of the track at impact.

4.2 Determination of the event t_0

As a result of the DAΦNE bunch-crossing period, which is short relative to the trigger-formation time, the experiment cannot be triggered with every bunch crossing. The level-1 trigger is rephased with the bunch-crossing time, and the bunch crossing which originated a given event is determined offline [4,8]. For this analysis, we determine the event t_0 using the tracks from the K_S. We begin by considering clusters with $d^{\perp}_{\mathrm{TCA}} < 30$ cm about the extrapolation of each track. We only consider clusters with $E > 50$ MeV. If there is more than one candidate, we use the cluster nearest to the track, *i.e.*, that for which $d^{\perp}_{\mathrm{TCA}}$ is smallest.

If a cluster is successfully associated to the track, the difference between the measured time of flight and that predicted on the basis of path-length and momentum measurements is used to estimate the event t_0. For the case in which the extrapolation is made from the first branch of the tree, which is assumed to be a pion track, this difference is:

$$\Delta\mathrm{TOF} = t_{\mathrm{cl}} - \left[\frac{L_{K_S}}{\beta_{K_S} c} + \frac{L_\pi}{\beta_\pi c} + \delta t_{\mathrm{int}}\right], \tag{3}$$

where L_{K_S} is the distance between the K_S vertex and the ϕ vertex calculated for the event ($\mathbf{x}_\phi$), β_{K_S} is calculated from the magnitude of the tagging momentum, L_π refers to the entire path length of the extrapolated pion track, including the reverse extrapolation to the K_S vertex and the forward extrapolation to the calorimeter, as well as the length of the pion track itself, and δt_{int} is a tunable parameter on the order of 400 ps which is intended to take into account the mean residual between calorimeter-impact and cluster-centroid times. Any previous estimate of the event t_0 is resummed into t_{cl} before evaluating ΔTOF. For the case in which the extrapolation is made from the second branch of the tree, corresponding to the muon track emerging from a π-μ kink, an additional term is added to Eq. (3):

$$\Delta\mathrm{TOF} = t_{\mathrm{cl}} - \left[\frac{L_{K_S}}{\beta_{K_S} c} + \frac{L_\pi}{\beta_\pi c} + \frac{L_\mu}{\beta_\mu c} + \delta t_{\mathrm{int}}\right]. \tag{4}$$

From each value of ΔTOF, an estimate of the event t_0 is obtained in the usual way, *i.e.*, by first calculating the trigger time, t_{trig}, as

$$t_{\mathrm{trig}} \equiv T_{\mathrm{expected}} + \Delta t_{\mathrm{cal}} - t_{\mathrm{cl}} = \Delta t_{\mathrm{cal}} - \Delta\mathrm{TOF},$$

where Δt_{cal} is a time delay associated with the calorimeter readout (frequently referred to in KLOE as "Delta Cavi Calo"); and then by rounding t_{trig} to an integer number of RF buckets and subtracting Δt_{cal}.

If both pion tracks are associated to clusters, two estimates of the event t_0 are obtained. If exactly one of the tracks was extrapolated to the calorimeter in a single shot (*i.e.*, if it was the only branch of the tree into which it was expanded, or more precisely still, if the extrapolation was "golden" by the criteria of Ref. 7), then the final t_0 estimate is taken from that track. If both tracks are extrapolated in a single shot, or if neither track is, then the t_0 estimate from the cluster with the smaller absolute value of ΔTOF is used.

Once a good estimate of the event t_0 has been obtained, all cluster times are adjusted accordingly.

4.3 K_S topologies which satisfy the calorimeter trigger

The main source of tag bias is the dependence of the trigger efficiency on the K_L behavior. The hardware calorimeter trigger [9], which requires two local energy deposits above some threshold (50 MeV on the barrel and 150 MeV on the end caps), is used for the present analysis.

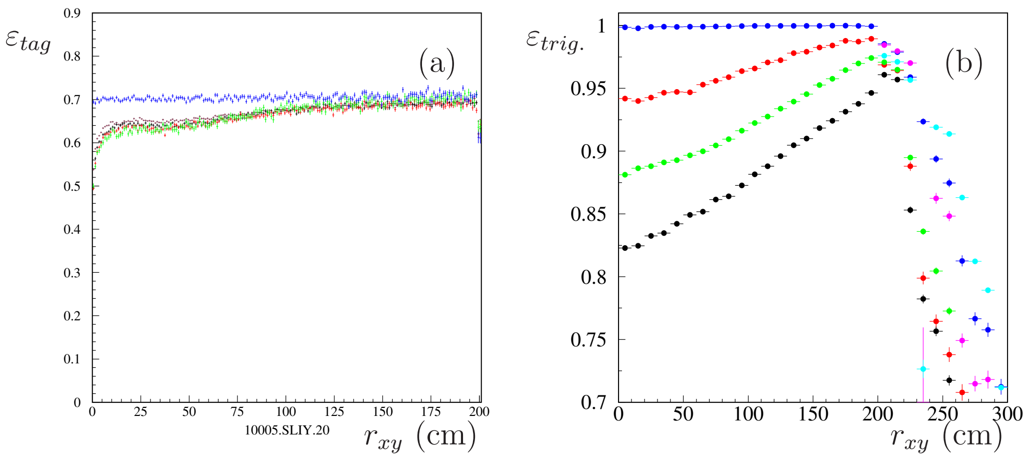

Fig. 3. (a) Tagging efficiency vs r_{xy}; (b) Trigger efficiency vs r_{xy} for tagged events. Different colors are used for different channels: blue for $\pi^0\pi^0\pi^0$, red for $\pi^+\pi^-\pi^0$, green for $\pi^\pm e^\mp\nu$, black for $\pi^\pm\mu^\mp\nu$, and cyan for nuclear interactions in the calorimeter.

The trigger efficiency is essentially 100% for events in which the K_L decays to $\pi^0\pi^0\pi^0$, between 85-95% for events in which the K_L decays to charged daughters, and lower for events in which the K_L interacts in the calorimeter or escapes. This diffrence in trigger efficiency translates into the following values for the tag bias of the charged and neutral decay modes. From Monte Carlo studies, we evaluate a tag bias value of about 0.99 and 1.06 for K_L decays to charged particles and to $3\pi^0$, respectively. However, the present accuracy of about of 30% on the K_L-nuclear interaction cross section would translate into an uncertainty of about 3%

in the absolute branching ratio measurements if it were necessary to obtain the absolute values of the trigger efficiencies from the Monte Carlo.

The difference in the tagging efficiency also depends on the position of the K_L decay vertex. Figure 3(a) shows the tagging efficiency as function of the transverse radial position of the K_L decay vertex for the dominant decay modes. This effect is mainly due to the use of position-dependent trigger thresholds. The variation of the trigger efficiency as a function of the transverse radial position of the K_L decay vertex is shown in Figure 3(b), both for the dominant K_L decay modes and for K_L-nuclear interactions.

Therefore, it is fundamental to know whether the K_S alone can satisfy the calorimeter trigger in order to reduce the tag bias.

To identify events in which the K_S alone satisfies the calorimeter trigger, a minimal requirement is the presence of two clusters from the $K_S \to \pi^+\pi^-$ decay associated with fired trigger sectors. For the present analysis, this requirement has been reinforced by verifying the trigger with a lower cut on the cluster energies $E_{\text{cluster}} > E_{\text{threshold}}$, where $E_{\text{threshold}}$ is the energy at which the trigger-sector efficiency reaches its plateau value. This condition is sufficient to ensure the satisfaction of the trigger criteria at the 99.8% level. For this analysis, only events with a barrel-barrel trigger configuration are used. A value of 100 MeV has been used for $E_{\text{threshold}}$ and a value of 15 cm has been used for the upper cut on $d^{\perp}_{\text{TCA}}$.

The resulting overall tagging efficiency is about 12%, but the difference between the tag bias values among the various channels is reduced: the average value of the tag bias for decays to charged particles is 0.98 and that for the $3\pi^0$ mode is 1.02.

Another contribution to the tag bias is the dependence of the reconstruction efficiency for the pion tracks from $K_S \to \pi^+\pi^-$ on the presence of other tracks in the drift chamber. We refer to this effect as *tracking interference*. This effect produces a difference in the tagging efficiencies for events with K_L decays to charged particles and to $3\pi^0$; this contribution to the tag bias additionally depends on the position of the K_L decay point. The effect is smaller when the pions from K_S decay are emitted orthogonally to the K_S direction. A cut on the difference of the pion momenta, $|\Delta P_{track}| < 60$ MeV, further reduces the difference in the tag bias values. As a result, the efficiency of the tag is about 9%, the tag bias for K_L decays to charged particles is about 0.97, and that for decays to $3\pi^0$ is about 1.00.

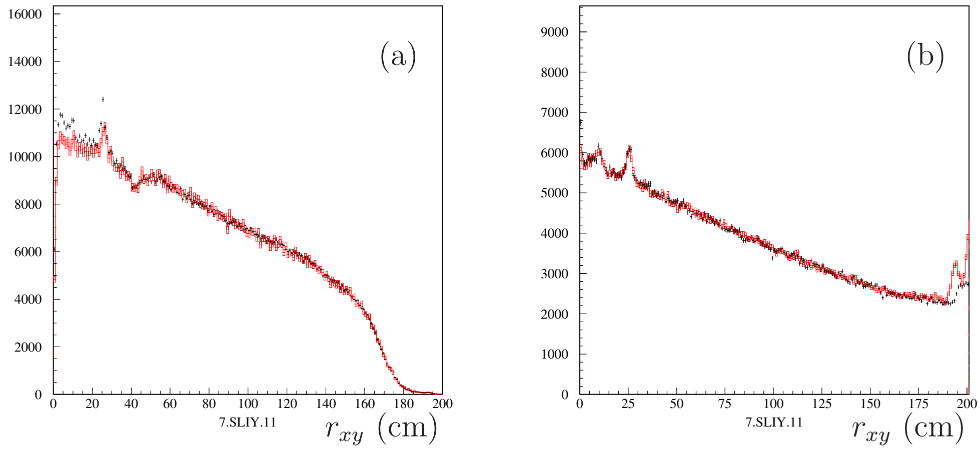

Fig. 4. Reconstructed r_{xy} distributions for K_L decays to (a) charged particles and (b) $3\pi^0$, for data (black) and Monte Carlo (red).

4.4 Evaluation of the tag bias

The tag bias has been evaluated with the KLOE Monte Carlo (MC) simulation, GEANFI [4]. A very small fraction of events tagged by the K_S decay are rejected because the cosmic-ray veto is satisfied by the K_L decay products. The value of the tag bias is corrected using a subsample of events for which the cosmic-ray veto decision was recorded but not enforced. This study shows that only for the K_L-crash topology is there a non-negligible effect on the tagging efficiency; the value of $\varepsilon_{\mathrm{tag_{tot}}}$ (Eq. [1]) increases by a factor of 1.002, with a negligible statistical uncertainty.

A data-MC comparison of the K_L vertex position distribution for charged and neutral modes is used to validate and correct the Monte Carlo results. Figure 4(a) shows the distribution of the transverse radius, r_{xy}, of the reconstructed vertex position for K_L decays to charged particles (see Sec. 6 for a description of the reconstruction of such decays), both for data and Monte Carlo. Only loose K_L-tag requirements have been applied; in particular, a self-triggering K_S decay is not required. The overall agreement is good, but there is a small discrepancy at low values of r_{xy}. Before applying any corrections for this effect, we have attempted to understand its origin in terms of data-MC differences in the tracking efficiency, incorrect treatment of K_L nuclear interactions in the MC, and data-MC differences in the effects of tracking interference.

The Monte Carlo distribution in Figure 4(a) has been produced using the efficiency corrections obtained from data (see Sec. 6). The effects of the corrections are illustrated in Figure 5, which shows the data-Monte Carlo ratio of the r_{xy} distributions without tracking-efficiency corrections. Without corrections, the deviation from unity is much larger at high values of r_{xy} (*i.e.*, close to the outer wall of the drift chamber), where the tracking efficiency is low because of the reduced geometrical acceptance. This disagreement is not seen in Figure 4(a), where tracking efficiency corrections are applied. We conclude that if a tracking efficiency problem is successfully addressed in a region with low efficiency, the same corrections should work equally well in regions with high efficiency. For this reason, we exclude the hypothesis that data-MC differences in the tracking efficiency are the cause of the effect at low r_{xy}.

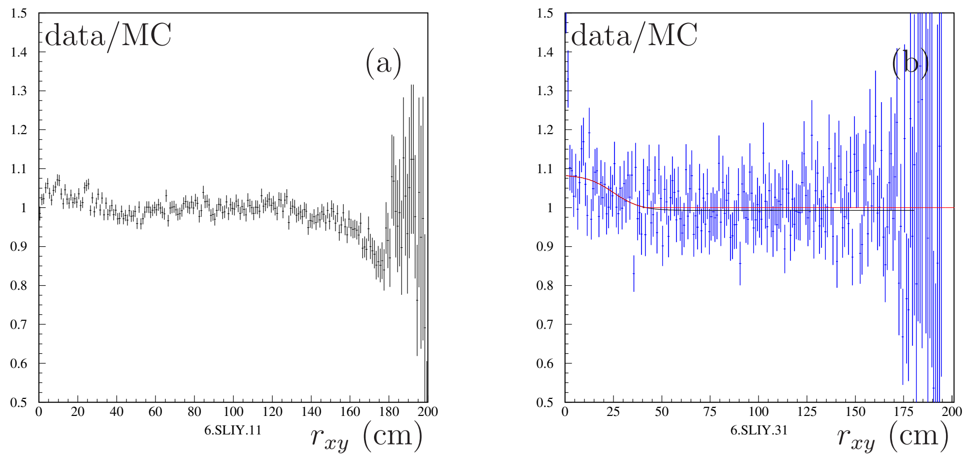

Fig. 5. Data-Monte Carlo ratio of reconstructed r_{xy} distributions for K_L decays to charged particles: (a) without tracking efficiency corrections and with loose K_L-tag requrements; (b) with tracking efficiency corrections and a self-triggering K_S decay.

To disprove the hypothesis that the effect at low r_{xy} is due to inaccurate treatment of K_L-nuclear interactions, in Figure 4(b) we show the r_{xy} distribution for $K_L \to \pi^0\pi^0\pi^0$ decays (see Sec. 7) both for data and Monte Carlo. Good agreement is observed, extending to the low r_{xy} region.

We are left with the tracking-interference hypothesis. This hypothesis is supported by the following observations. The vertex-finding algorithm used in the standard KLOE reconstruction procedure [4] searches for a vertex in three different regions: inside the beam pipe ($(x^2 + y^2 + z^2)^{1/2} < 10$ cm), between the beam pipe and the inner wall of the drift chamber at $r_{xy} = 25$ cm, and inside the drift chamber. Tracks are first used to form vertices in the innermost region. Since tracks associated to a reconstructed vertex cannot be used to form other vertices, it is possible to misreconstruct a vertex with one track from a K_S decay and one track from a K_L decay. This hypothesis is consistent with the r_{xy} dependence of the data-MC difference in the K_L vertex position distributions: the difference becomes apparent for r_{xy} values just below 25 cm (the outer border of the second region used by the vertex-finding algorithm) and increases slightly for r_{xy} below 10 cm (the outer border of the innermost region used by the vertex-finding algorithm).

Data period	$\varepsilon\mathrm{tag}_{\pi^\pm e^\mp \nu}$ / $\varepsilon\mathrm{tag}_{\mathrm{tot}}$	$\varepsilon\mathrm{tag}_{\pi^\pm \mu^\mp \nu}$ / $\varepsilon\mathrm{tag}_{\mathrm{tot}}$	$\varepsilon\mathrm{tag}_{\pi^+\pi^-\pi^0}$ / $\varepsilon\mathrm{tag}_{\mathrm{tot}}$	$\varepsilon\mathrm{tag}_{\pi^0\pi^0\pi^0}$ / $\varepsilon\mathrm{tag}_{\mathrm{tot}}$
1	0.970 ± 0.003	0.978 ± 0.003	0.978 ± 0.005	1.007 ± 0.004
2	0.972 ± 0.003	0.970 ± 0.003	0.980 ± 0.005	1.004 ± 0.004
3	0.972 ± 0.003	0.971 ± 0.003	0.982 ± 0.005	0.997 ± 0.004
4	0.971 ± 0.004	0.970 ± 0.004	0.982 ± 0.006	1.005 ± 0.005
5	0.970 ± 0.003	0.976 ± 0.003	0.981 ± 0.004	1.002 ± 0.003
6	0.974 ± 0.003	0.975 ± 0.003	0.983 ± 0.004	1.003 ± 0.003
7	0.972 ± 0.003	0.974 ± 0.003	0.980 ± 0.004	1.001 ± 0.003
8	0.971 ± 0.003	0.979 ± 0.003	0.979 ± 0.004	1.002 ± 0.003
9	0.973 ± 0.003	0.974 ± 0.003	0.985 ± 0.004	1.002 ± 0.003
10	0.972 ± 0.003	0.973 ± 0.003	0.987 ± 0.004	1.003 ± 0.003
11	0.972 ± 0.003	0.979 ± 0.003	0.981 ± 0.004	1.004 ± 0.003
12	0.969 ± 0.003	0.975 ± 0.003	0.981 ± 0.004	1.008 ± 0.003
13	0.972 ± 0.003	0.977 ± 0.003	0.980 ± 0.004	0.998 ± 0.003
14	0.977 ± 0.003	0.977 ± 0.003	0.974 ± 0.004	1.002 ± 0.003

Table 2
Values of the tag bias for different channels, by run period. The errors reflect only Monte Carlo statistics.

The correction to the tag-bias values for this effect is obtained by fitting the data-Monte Carlo ratio of the r_{xy} distributions with a Fermi-Dirac-like function:

$$p_1 - p_2 \left(1 - \frac{1}{1 + e^{-(r_{xy}-25)/p_3}}\right).$$

The value of the correction is run-period dependent and amounts typically to 0.5%. An example of one such fit is shown in Figure 5(b).

The values of the tag bias for the various decay modes are listed by data-taking period in Table 2. The statistical uncertainty on the tracking-interference correction deriving from the errors on the parameters of the fits to the ratio of r_{xy} distributions ranges between 0.2% and 1% depending on the run period. It is not included in Table 2.

5 Fiducial-volume efficiency

The fiducial volume (FV) used for the analysis lies completely within the drift chamber and is defined by $35 < r_{xy} \equiv \sqrt{x^2 + y^2} < 150$ cm and $|z| < 120$ cm, where (x, y, z) are the coordinates of the K_L decay vertex position. Since the mean K_L decay length in our experiment is 340 cm, the FV contains ∼26.1% of the K_L decays. This choice minimizes the difference in tag bias among decay modes. The fiducial volume efficiency depends on the K_L lifetime. Figure 6 shows the variation of the fiducial volume efficiency with the mean K_L decay length, for a spherical fiducial volume with boundaries at $r = 35$ cm and $r = 150$ cm. This dependence has been better studied using the GEANFI K_S, K_L generator.

We observe a linear dependence,

$$\varepsilon_{\rm FV}/\varepsilon^0_{\rm FV} = 1 + 0.0128\left[\tau^0 - \tau\right], \tag{5}$$

for $\tau(K_L)$ values around 50 ns (here, $\varepsilon^0_{\rm FV}$ refers to the FV efficiency calculated using $\tau^0 = 51.7$ ns). The loss of K_L's to nuclear interactions in the beam pipe wall, drift chamber wall, and drift chamber gas affects the evaluation of the fiducial volume efficiency. These losses are taken into account in GEANFI, and corrections obtained from data are applied (see Sec. 8).

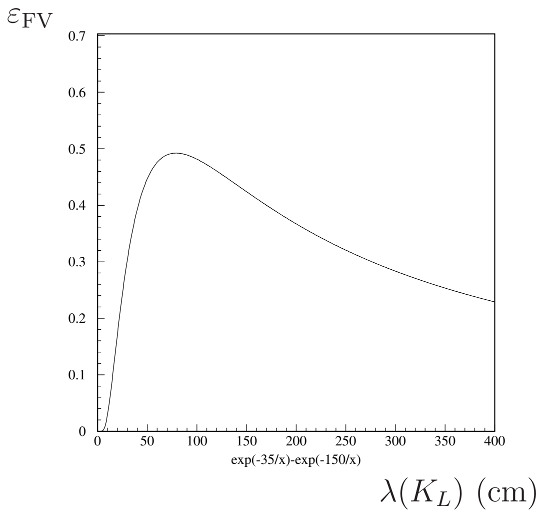

Fig. 6. Dependence of the fiducial volume efficiency on the mean K_L decay length for a spherical fiducial volume.

6 K_L decays into charged particles

6.1 Extrapolation and consolidation of tracks from K_L decay

All tracks in the chamber, after removal of those from the K_S decay and their descendants, are extrapolated to their points of closest approach to the line of flight of the K_L (also referred to as the *tagging line*). Each track can be extrapolated in four possible ways: in either of two senses (away from the track or along the track) starting from either end of the track. It is important to consider all four possibilities. Even if the correct end of the track is chosen, it is possible for the point of closest approach (PCA) to the tagging line to be found at a negative extrapolation length, *i.e.*, along the reconstructed track itself, since the tagging line is reconstructed with finite resolution. The correct extrapolation is identified as follows. At each end of the track, the correct sense of the extrapolation (forwards or backwards) is identified as that which minimizes the distance from the PCA to the tagging line, d_c. Then, the correct end of the track is identified as that from

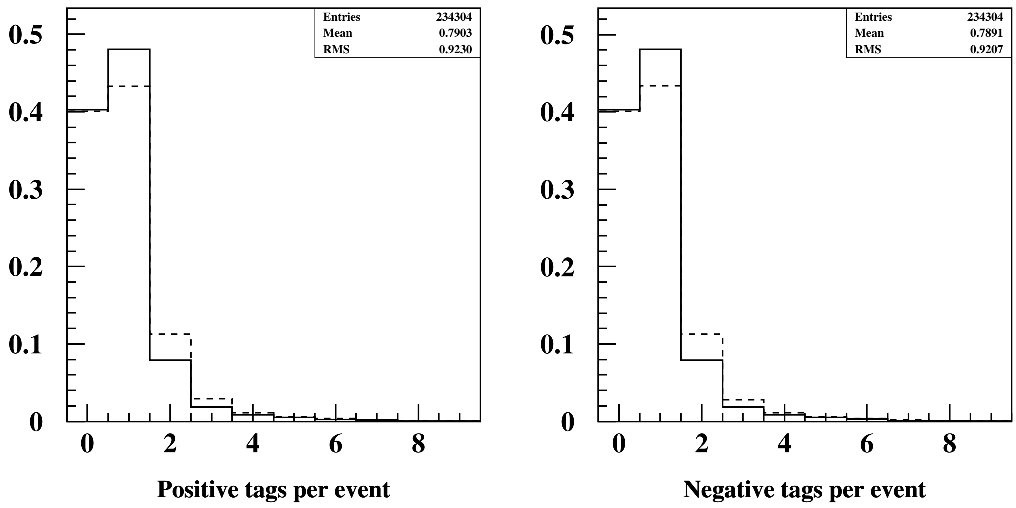

Fig. 7. Number of positive (left) and negative (right) tags per MC $K_L \to \pi^+\pi^-$ event, before (dashed) and after (solid) collection of candidate tracks into trees.

which the extrapolation to the tagging line is shorter in arc length, l_c. For any of the four possible extrapolations, if the position of the PCA, $\mathbf{x}_c$, is found outside of the volume of the drift chamber (*i.e.*, with $r_{xy} > 195$ cm or $|z| > 165$ cm), or if $\mathbf{x}_c$ is found on the same side of the chamber as the K_S (*i.e.*, $\mathbf{x}_c \cdot \mathbf{p}_{K_L} < 0$), that extrapolation is excluded when applying the above logic. For each candidate track, this procedure results in estimates of $\mathbf{x}_c$; the momentum of the track at $\mathbf{x}_c$, $\mathbf{p}_c$; the distance of closest approach, d_c; and the extrapolation length, l_c.

At this point, it is quite possible for there to be more than one candidate track for each sign of charge, even for signal events. The secondaries from K_L decay can themselves undergo decay in flight. Tracks can also be split by the reconstruction algorithm (particularly if they spiral). There may be interference from K_S secondaries not attached to their trees because of vertex reconstruction inefficiencies. There may even be spurious tracks in the event (*e.g.*, from cosmic rays). The situation is illustrated in Fig. 7, in which the dashed histograms show the multiplicity distributions for tags of each sign of charge in MC $K_L \to \pi^+\pi^-$ events.

In order to reduce the overall tag-candidate multiplicity and increase the probability of choosing the correct tagging tracks, we seek to make use of the available topological information by consolidating the candidate tracks into decay trees. After the collection process, the tag candidates are the “trunks” of each tree, rather than the individual K_L candidate tracks in the event, where the trunk of the tree is defined as the branch with the smallest distance of closest approach to the tagging line, d_c, when extrapolated as described above. (A tree can obviously consist of a single branch.) After the consolidation process, the tag-candidate multiplicity is reduced somewhat, as seen in the solid histograms in Fig. 7. For a each sign of charge, a larger fraction of events have only one tag while the fraction

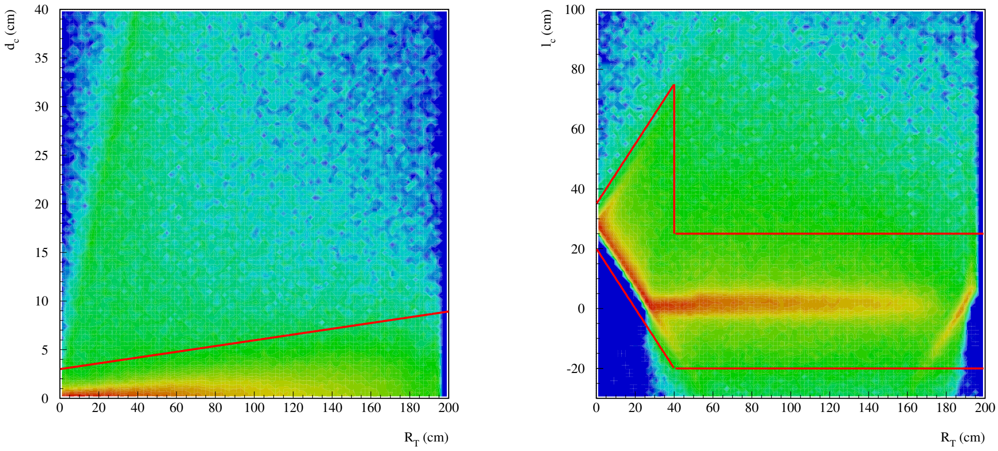

Fig. 8. Distributions of (a) d_c and (b) l_c vs. r_{xy}, for true tags, obtained with the Monte Carlo. Logarithmic scales are used for the third axis in each plot.

of events with no tags is not substantially increased.

For each tag candidate, we obtain the point of closest approach to the K_L line-of-flight, $\mathbf{x}_\mathrm{c}$. We then compute the distance of closest approach, d_c, the momentum $\mathbf{p}_\mathrm{c}$ of the track at $\mathbf{x}_\mathrm{c}$ and the extrapolation length, l_c. The most discriminating variable is d_c. For true tags, the resolution on d_c is determined by the quality of the extrapolation (or equivalently, the reconstruction) of the track which defines the tag, and by the finite resolution on the determination of the tagging line. This latter is an angular effect, and so we expect the distribution in d_c to broaden for K_L decays at increasing distance from the origin. In Fig. 8(a), we present the two-dimensional distribution of d_c vs. r_{xy} for true tags, as obtained with the Monte Carlo. The effect of the finite resolution is prominent. The analogous distribution of l_c vs. r_{xy} is presented in Fig. 8(b)

We consider the one "true" tag for each sign of charge to be the tag with the smallest value of d_c. Tracks satisfying $d_\mathrm{c} < ar_{xy} + b$, with $a = 0.03$ and $b = 3$ cm, and -20 cm $< l_\mathrm{c} <$ 25 cm are accepted as K_L decay products. These cuts are indicated in Fig. 8 by red lines.

To improve the reconstruction of K_L decays into charged particles the KLOE vertex-reconstruction algorithm VTXFIN has been used for events with two good tracks from a K_L decay. The intrinsic VTXFIN efficiency for the reconstruction of a true K_L decay vertex using two tracks satisfying the cuts described above is quite high. Much of the vertex-reconstruction inefficiency at the initial data reconstruction stage can be ascribed to combinatorial problems in identifying the correct tracks to associate to the vertex in the first place. With these considerations in mind, we adopt the following approach. Selection of the positive and negative tracks from the K_L decay proceeds as described above. If we find that during data reconstruction, VTXFIN has reconstructed a vertex from the two tracks selected, then that vertex is used. Otherwise, the relevant VTXFIN routines are directly called to form a vertex from the two selected tracks. This procedure results in an efficiency of approximately 97% for the reconstruction of a vertex from the selected tracks.

For the analysis, then, we require two good K_L decay tracks forming a vertex. The average efficiency for the track and vertex reconstruction is 54% for K_{e3} 52% for $K_{\mu 3}$ and 38% for $\pi^+\pi^-\pi^0$ as evaluated from Monte Carlo simulation. These efficiencies are then corrected as described in the following; the corrections range between 1.03 and 0.99 and depend on the channel and on the subsample.

6.2 Reconstruction efficiency for single tracks

The tracking efficiency can be determined by counting the number of events in which there is a K_L decay track of at least one sign and the number of events in which there are two decay tracks of opposite sign. The data-MC difference in the single-to-double ratio is then used to correct the MC estimate for the tracking efficiency. This correction is evaluated as function of the track momentum using $K_L \to \pi^+\pi^-\pi^0$ and $\pi^\pm e^\mp \nu$ events. In $K_L \to \pi^+\pi^-\pi^0$ events, the momentum of one decay track is calculated with a resolution of about 10 MeV using the two photons from the π^0 decay and the momentum of the other decay track. In order to obtain the correction for higher momentum tracks (above $\sim$ 150 MeV), $\pi^\pm e^\mp \nu$ decays are used, in which the electrons are identified by time of flight with a purity of ~95%. The momentum of the pion track from the K_L is then evaluated from the missing energy with a resolution of about 30 MeV.

To select $K_L \to \pi^+\pi^-\pi^0$ events, we require at least one good K_L decay track and two photons from a π^0 decay. To reject background, cuts are applied on the two-photon invariant mass and on the times of flight of the photons.

The direction of the i^{th} photon, $\hat{\mathbf{n}}_{\gamma i}$, is derived from the position of the point of closest approach to the K_L line-of-flight, $\mathbf{x}_{\text{c}}$, and the position of the centroid of the i^{th} cluster, $\mathbf{x}_{\text{cl}\,\gamma i}$:

$$\hat{\mathbf{n}}_{\gamma i} = \frac{\mathbf{x}_{\text{cl}\,\gamma i} - \mathbf{x}_{\text{c}}}{d_{\gamma i}}, \tag{6}$$

where $d_{\gamma i}$ is the photon path length,

$$d_{\gamma i} = |\mathbf{x}_{\text{cl}\,\gamma i} - \mathbf{x}_{\text{c}}|. \tag{7}$$

The difference between the two-photon invariant mass evaluated from the photon directions and energies and the π^0 mass is required to be within 40 MeV:

$$|M_{\gamma\,1\,2} - m_{\pi^0}| < 40\,\mathrm{MeV} \tag{8}$$

In addition, the difference of the residuals between the expected and measured times of flight must be smaller than 1 ns:

$$|(t_{\exp\gamma\,1} - t_{\mathrm{cl}\,\gamma\,1}) - (t_{\exp\gamma\,2} - t_{\mathrm{cl}\,\gamma\,2})| < 1\,\mathrm{ns} \tag{9}$$

where $t_{\mathrm{cl}\,\gamma\,i}$ is the measured arrival time for photon i, and $t_{\exp\gamma\,i}$ is the expected arrival time, $t_{\exp\gamma\,i} = d_{\gamma\,i}/c$.

Finally, the distance between the point of closest approach of the track to the K_L line-of-flight and the energy-weighted average of the neutral vertices for each of the two photons is required to be smaller than 10 cm. (Neutral vertices are the reconstructed origins of photons assumed to come from K_L decay, and are reconstructed from time-of-flight measurements as discussed in Refs. 4 and 8.)

The momentum of the "missing" track can be evaluated a priori from kinematics. We perform a kinematic fit to improve the determination of the photon energies. The χ^2 used in the fit is

$$\chi^2 = \sum_{i=1}^{2} \left(\frac{E_{x\,\gamma\,i} - E_{\mathrm{cl}\,\gamma\,i}}{\sigma_{E\,i}} \right)^2 + \left(\frac{M_{x\,\gamma\,1\,2} - m_{\pi^0}}{2\ \mathrm{MeV}} \right)^2 + \left(\frac{M_{\mathrm{trk\,miss}} - m_{\pi^\pm}}{2\ \mathrm{MeV}} \right)^2 \tag{10}$$

where $E_{x\,\gamma\,i}$ and $E_{\mathrm{cl}\,\gamma\,i}$ are the fitted and the measured photon energies, $\sigma_{E\,i}$ is the expected energy resolution ($\sigma_E/E = 5.7\%/\sqrt{E(\mathrm{GeV})}$), $M_{x\,\gamma\,1\,2}$ is the two-photon invariant mass, and $M_{\mathrm{trk\,miss}}$ is the missing mass (the mass of the "would-be-detected pion") evaluated from:

$$M^2_{\mathrm{trk\,miss}} = E^2_{\mathrm{miss}} - p^2_{\mathrm{miss}}$$

where

$$E_{\mathrm{miss}} = E_{K_L} - E_{\pi^0} - E_{\mathrm{trk}}. \tag{11}$$

In Eq. (11), the K_L momentum is obtained from the tag, E_{π^0} is the sum of the photon energies, and E_{trk} is calculated from the track momentum in the charged-pion mass hypothesis. The requirement $\chi^2 < 5$ further reduces the background. The resolution on the a priori evaluation of the momentum is about 10 MeV. Figure 9 shows the distribution of the difference between the expected and measured momenta for both data and Monte Carlo. The data-MC agreement is adequate for our purposes.

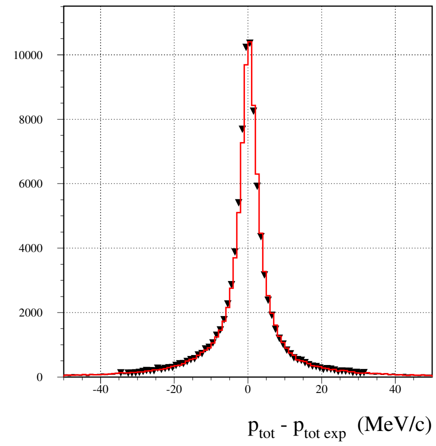

Fig. 9. Distribution of the difference between the expected and measured track momenta for $K_L \to \pi^+\pi^-\pi^0$ decays in data (triangles with errors) and Monte Carlo (solid line).

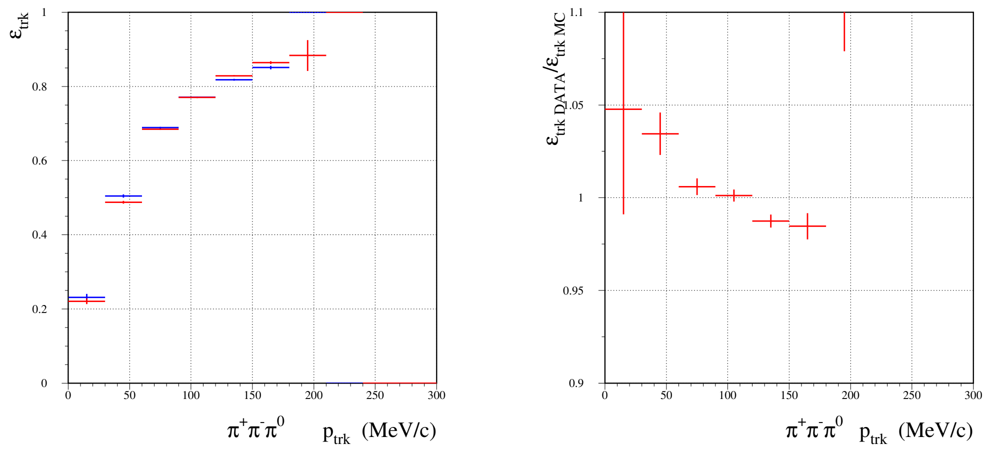

Fig. 10. Left: Tracking efficiency obtained from $K_L \to \pi^+\pi^-\pi^0$ decays as a function of momentum for data (red) and Monte Carlo (blue). Right: Data-Monte Carlo ratio of tracking efficiencies.

Figure 10, left, shows the tracking efficiency as a function of the track momentum, both for data and Monte Carlo. The ratio of the efficiencies is shown in Fig. 10, right. These results are obtained for the same fiducial volume used for the analysis.

$K_L \to \pi^\pm e^\mp \bar{\nu}_e(\nu_e)$ are selected by identifying the electrons by time of flight. The candidate electron track is extrapolated to the calorimeter and the track-to-cluster association procedure described in Sec. 4.1 is applied. The expected time of flight for an electron with momentum $\mathbf{p}_\mathrm{c}$ at the point of closest approach to the K_L line of flight, $\mathbf{x}_\mathrm{c}$, is

$$t_{e\,\mathrm{exp}} = \frac{L}{\beta_e c}, \tag{12}$$

where $\beta_e = |\mathbf{p}_\mathrm{c}|/E_e$ with $E_e = (\mathbf{p}_\mathrm{c}^2 + m_e^2)^{1/2}$, and L is the length of the electron trajectory from the point $\mathbf{x}_\mathrm{c}$ to the calorimeter.

The expected K_L time of flight is given by

$$t_{K_L\,\mathrm{exp}} = \frac{|\mathbf{x}_\phi - \mathbf{x}_\mathrm{c}|}{\beta_{K_L} c} \tag{13}$$

where $\mathbf{x}_\phi$ is determined as described in Sec. 4. The value of β_{K_L} is calculated from global momentum balance as described in Sec. 4.

K_{e3} decays are identified by the requirement

$$\Delta t_e = |t_{\mathrm{cl\,trk}} - (t_{e\,\mathrm{exp}} + t_{K_L\,\mathrm{exp}})| < 0.5\,\mathrm{ns}. \tag{14}$$

The purity of this K_{e3} sample is about 95%. The remaining background is due mostly to $K_{\mu 3}$ decays. The momentum of the "missing" pion can be inferred from the missing energy, using the momenta of the K_L and of the candidate electron track, $\mathbf{p}_\mathrm{c}$:

$$E_\mathrm{miss} = \sqrt{\mathbf{p}_{K_L}^2 + m_{K_L}^2} - \sqrt{\mathbf{p}_\mathrm{c}^2 + m_e^2}.$$

The average magnitude of the pion momentum is linearly related to the missing energy with a large spread due to the presence of the undetected neutrino, as illustrated in Fig. 11:

$$\mathbf{p}_{\pi^\pm} = a + bE_\mathrm{miss}. \tag{15}$$

A fit to the two-dimensional distribution of $E_\mathrm{miss} - |\mathbf{p}_{\pi^\pm}|$ has been performed to determine the values of the coefficients a and b. The resulting values are -150 MeV/c and $0.95c^{-1}$, respectively.

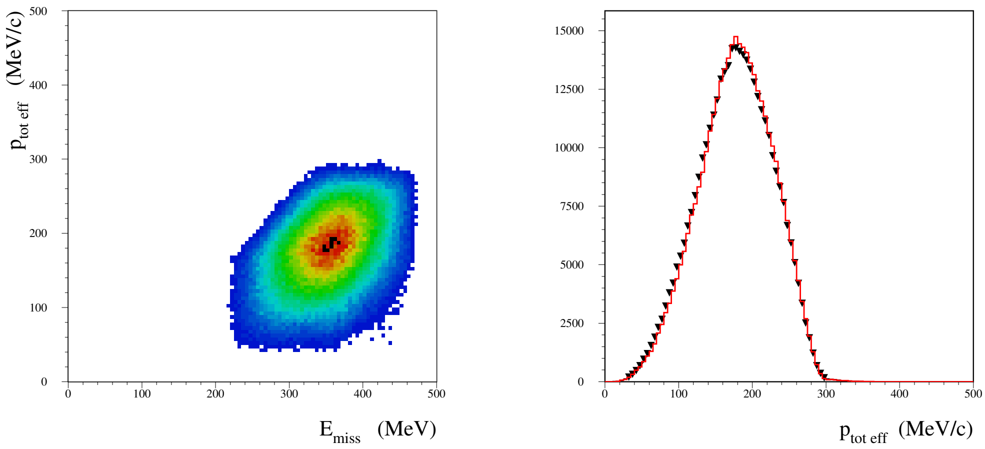

Fig. 11. Left: Momentum of the pion track, $|\mathbf{p}_{\pi^\pm}|$, as a function of the missing energy E_{miss}, in $K_L \to \pi^\pm e^\mp \bar{\nu}_e(\nu_e)$ events. Right: Comparison of the distributions of $|\mathbf{p}_{\pi^\pm}|$ for data (black triangles) and Monte Carlo (red solid line).

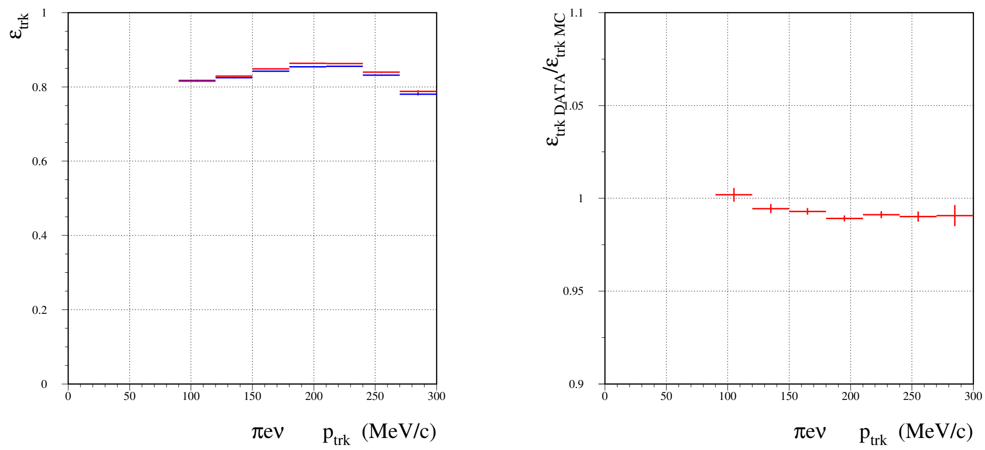

Fig. 12. Left: Tracking efficiency from $K_L \to \pi^\pm e^\mp \bar{\nu}_e(\nu_e)$ events, for data (red) and Monte Carlo (blue). Right: Data-Monte Carlo ratio of tracking efficiencies.

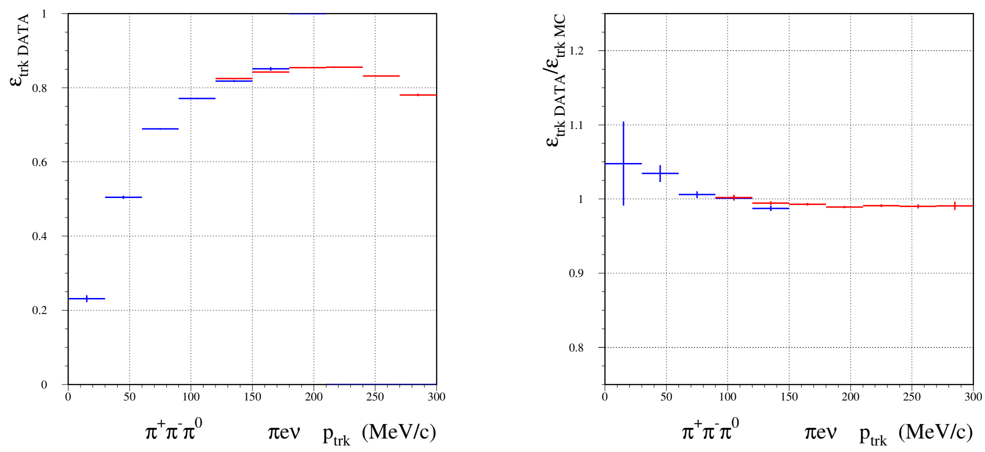

Fig. 13. Left: Tracking efficiency from $K_L \to \pi^+\pi^-\pi^0$ (blue) and $K_L \to \pi^\pm e^\mp \bar{\nu}_e(\nu_e)$ (red) events, for data. Right: Data-Monte Carlo ratio of tracking efficiencies for the two samples.

The tracking efficiency as a function of momentum obtained with $K_L \to \pi^\pm e^\mp \bar{\nu}_e(\nu_e)$ events is shown in Fig. 12 both for data and Monte Carlo. The comparison of the tracking efficiency obtained from $K_L \to \pi^\pm e^\mp \bar{\nu}_e(\nu_e)$ events in Fig. 12 and that obtained from $K_L \to \pi^+\pi^-\pi^0$ events in Fig. 10 shows good agreement in the overlap region 100–150 MeV (see also Fig. 13). In the region below 100 MeV, the conditional tracking efficiency from $K_L \to \pi^\pm e^\mp \bar{\nu}_e(\nu_e)$ events is systematically lower than that from $K_L \to \pi^+\pi^-\pi^0$ events. This effect is due both to the differences in the selection criteria and to worse resolution in the expected track momentum in $K_L \to \pi^\pm e^\mp \bar{\nu}_e(\nu_e)$ events at small expected momentum.

It should be emphasized that these procedures result in estimates of the *conditional* tracking efficiency. The results are used only to evaluate the correction to be applied to the tracking efficiency estimates obtained from Monte Carlo. Good agreement between the results obtained using $K_L \to \pi^+\pi^-\pi^0$ events and $K_L \to \pi^\pm e^\mp \bar{\nu}_e(\nu_e)$ events is obtained for the data-Monte Carlo ratio of the tracking efficiency over the entire momentum spectrum, as seen from Figs. 10 and 12. Because the expected momentum is determined with better precision in $K_L \to \pi^+\pi^-\pi^0$ events at low momentum, for momenta smaller than 150 MeV, we use the correction obtained from this sample, while for momenta greater than 150 MeV, we use the correction obtained from $K_L \to \pi^\pm e^\mp \bar{\nu}_e(\nu_e)$ events. It can be seen from Fig. 12 that the both the tracking efficiency and the correction are nearly constant above 150 MeV, so that the poor resolution on the determination of the expected momentum is less important in this case.

The correction is calculated as

$$f_{\text{trk corr}}(\mathbf{p}_{\text{trk}}) = \varepsilon_{\text{data}}/\varepsilon_{\text{MC}} \tag{16}$$

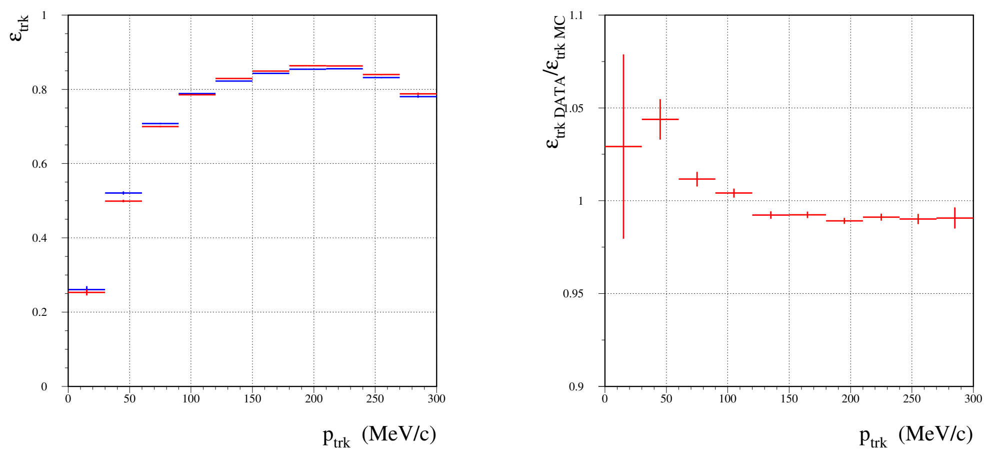

Fig. 14. Left: Tracking efficiency estimated using $K_L \to \pi^+\pi^-\pi^0$ and $K_L \to \pi^\pm e^\mp \bar{\nu}_e(\nu_e)$ decays, as a function of expected track momentum, for Monte Carlo (red) and data (blue). Right: Data-Monte Carlo ratio of tracking efficiencies.

and is applied as a function of momentum in 30 MeV bins. It is shown in Fig. 14.

The quality of the tracking-efficiency correction may be checked in an inclusive manner by comparing the efficiencies evaluated directly from the data with those obtained using Monte Carlo events and applying the data-MC correction. We examine the tracking efficiency as a function of p^* of the *tagging* track, where p^* is the track momentum transformed to the K_L center-of-mass frame. The conditional efficiency examined in this case is simply $\varepsilon_{\rm incl} = 2N_2/N_1$, with N_1 the number of tagging tracks reconstructed (up to a maximum of two per event, one of each sign), and N_2 the number of events in which two tagging tracks of opposite sign are reconstructed. Only charge conservation is assumed at the K_L decay vertex—to the extent that $\varepsilon_{\rm incl}$ is parameterized by the value of p^* for the tagging tracks, no assumptions about the decay kinematics are necessary. The tagging tracks are assumed to have the pion mass for the transformation into the K_L rest frame.

Figure 15 shows the results of such a comparison for a single run period. The first panel shows the distribution of p^* for tagging tracks at the K_L decay vertex. The second panel shows the comparison between $\varepsilon_{\rm incl} = 2N_2/N_1$ for data, and the same quantity for Monte Carlo but weighted by the data-MC corrections to the tracking efficiency of Fig. 14, right. The third panel shows the ratio of the points for data to those for Monte Carlo, and demonstrates that the corrected inclusive MC efficiency matches well with the inclusive efficiency obtained directly from data.

The effects of the tracking efficiency on the tag bias have been studied by com-

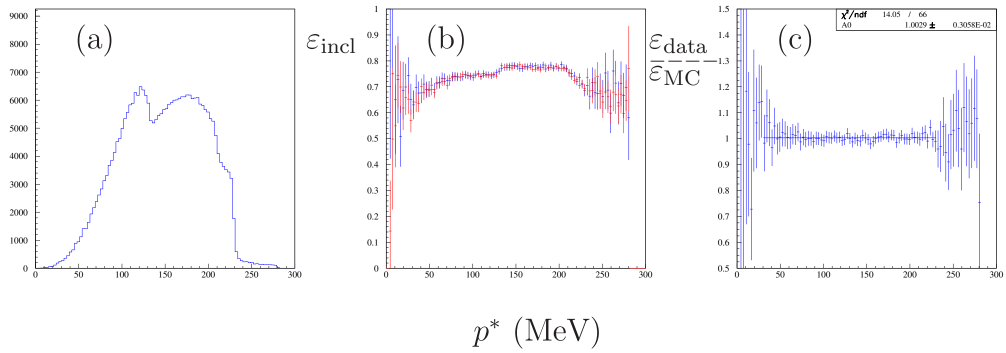

Fig. 15. Inclusive tracking efficiency as a function of p^*. (a) Distribution of p^* for single tracks at the $K_L$vertex in data; (b) Inclusive tracking efficiency as a function of p^* for data (blue) and Monte Carlo (red), with data-MC correction factors applied in the latter case; (c) Ratio of inclusive tracking efficiency for data to that for corrected Monte Carlo, as a function of p^*.

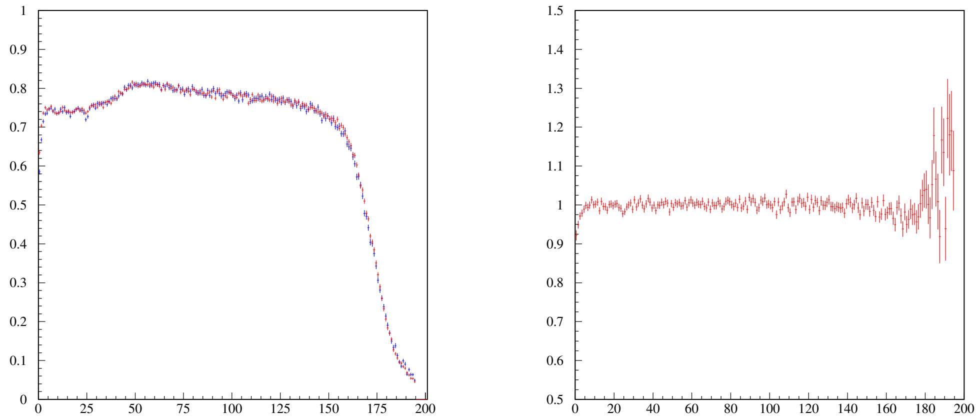

Fig. 16. Left: Tracking efficiency as a function of the transverse vertex position for data (blue) and Monte Carlo (red). Right: Data-Monte Carlo ratio of tracking efficiencies as a function of the transverse vertex position.

paring the K_L vertex-position distributions for data and Monte Carlo, and by measuring the K_L lifetime (see Sec. 9.1). For these purposes, the correction to the Monte Carlo tracking efficiency has been evaluated as a function of the vertex position, using an inclusive sample of all K_L decays into charged particles. An example of this analysis is shown in Fig. 16, where the tracking efficiencies for data and MC (left) and their ratio (right) are shown as a function of the transverse vertex position.

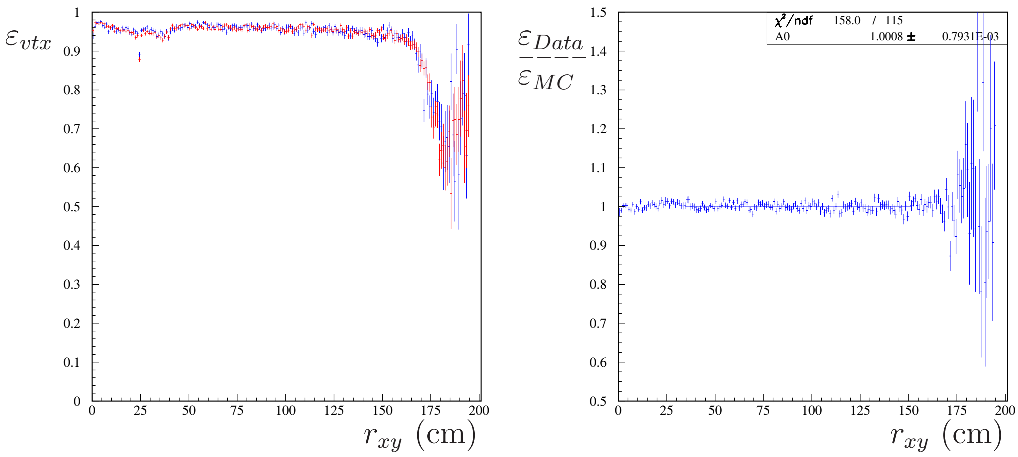

Fig. 17. Left: Vertex efficiency as a function of the transverse radius for data (blue) and Monte Carlo (red). Right: Data-Monte Carlo ratio of vertex efficiencies as a function of the transverse radius.

6.3 Vertex-reconstruction efficiency

The vertex efficiency is the ratio of the number of events with at least two good K_L decay tracks of opposite charge that form a vertex to the number of events with at least two good K_L decay tracks of opposite charge. As shown in Fig. 17, the vertex efficiency is close to 100%, and the values obtained from Monte Carlo are in agreement with those for data to within 0.1%. We have also examined the consistency between data and Monte Carlo for each individual K_L decay mode identified by the value of $\Delta_{\mu\pi}$ as discussed in the following section.

The values of tracking plus vertex efficiency are given in Table 3.

6.4 Identification of K_L decays into charged particles

Monte Carlo studies have shown that the best discriminant amongst the K_L decay modes into charged particles is the smaller of the two possible values of $\Delta_{\mu\pi}=|\mathbf{p}_{\text{miss}}|-E_{\text{miss}}$, where $\mathbf{p}_{\text{miss}}$ and E_{miss} are the missing momentum and energy at the K_L vertex, evaluated by assigning one track the pion mass and one track the muon mass. The shape of the $\Delta_{\mu\pi}$ spectrum is very sensitive to the radiative corrections to K_L decay processes. This is particularly evident for K_{e3} decays. The KLOE Monte Carlo includes very accurate generators for the radiative channels, as described in [5].

The residual background consists of events with two good K_L decay tracks forming a vertex not due to K_{e3}, $K_{\mu3}$, or $\pi^+\pi^-\pi^0$ decays. The primary sources of such background are $K_L \to \pi^+\pi^-$ decays, $K_L \to \pi^0\pi^0\pi^0$ decays with $\pi^0\pi^0 \to e^+e^-\gamma$,

Data period	$\varepsilon_{\mathrm{trk}_{\pi^\pm e^\mp \nu}}$	$\varepsilon_{\mathrm{trk}_{\pi^\pm \mu^\mp \nu}}$	$\varepsilon_{\mathrm{trk}_{\pi^+ \pi^- \pi^0}}$
1	0.538 ± 0.004	0.520 ± 0.004	0.373 ± 0.005
2	0.531 ± 0.004	0.510 ± 0.004	0.365 ± 0.005
3	0.543 ± 0.003	0.523 ± 0.004	0.377 ± 0.004
4	0.545 ± 0.005	0.525 ± 0.005	0.380 ± 0.006
5	0.549 ± 0.003	0.530 ± 0.004	0.379 ± 0.005
6	0.556 ± 0.003	0.535 ± 0.003	0.390 ± 0.004
7	0.555 ± 0.003	0.533 ± 0.004	0.384 ± 0.004
8	0.550 ± 0.003	0.529 ± 0.004	0.386 ± 0.005
9	0.550 ± 0.003	0.530 ± 0.003	0.380 ± 0.004
10	0.553 ± 0.003	0.533 ± 0.004	0.392 ± 0.005
11	0.545 ± 0.003	0.530 ± 0.004	0.380 ± 0.004
12	0.547 ± 0.003	0.531 ± 0.004	0.386 ± 0.005
13	0.544 ± 0.003	0.523 ± 0.004	0.379 ± 0.005
14	0.551 ± 0.003	0.533 ± 0.004	0.385 ± 0.004

Table 3
Values of tracking plus vertex efficiency for different channels.

$K_L \to K_S \to \pi^+\pi^-$ regeneration, and Λ, Σ production from K_L nuclear interactions. The total amount is about 0.5%. Figure 18 shows the $\Delta_{\mu\pi}$ distribution from Monte Carlo for the dominant K_L decays and the residual background. The Monte Carlo evaluation is scaled according to the results of the study described in Sec. 8.

The momentum resolution in the Monte Carlo is slightly better than in data, and the reconstructed track momenta for Monte Carlo events have been additionally smeared to obtain better agreement with data. The fact that the momentum resolution is better in the Monte Carlo is due both to differences in the hit resolution in data and in the Monte Carlo and to the limited knowledge of the magnetic field map [10]. The latter effect increases with r_{xy}, where the corrections due to the misalignment of the field probes are larger. For this reason, we evaluate the smearing parameters for two different regions. For $r_{xy} < 50$ cm, an additional Gaussian smearing of 0.15% has been applied to the transverse momentum of the Monte Carlo tracks. For $r_{xy} > 50$ cm, an additional smearing with two Gaussians has been applied for a small fraction of events. The values of the smearing parameters and the fraction events smeared have been evaluated by fitting the $|\mathbf{p}_{\mathrm{miss}}| - E_{\mathrm{miss}}$ distribution for data with a linear combination of Monte Carlo distributions for $K_L \to \pi^\pm e^\mp \nu$, $K_L \to \pi^\pm \mu^\mp \nu$, and $K_L \to \pi^+\pi^-\pi^0$ events. The complex minimization problem has been handled using a genetic algorithm [11].

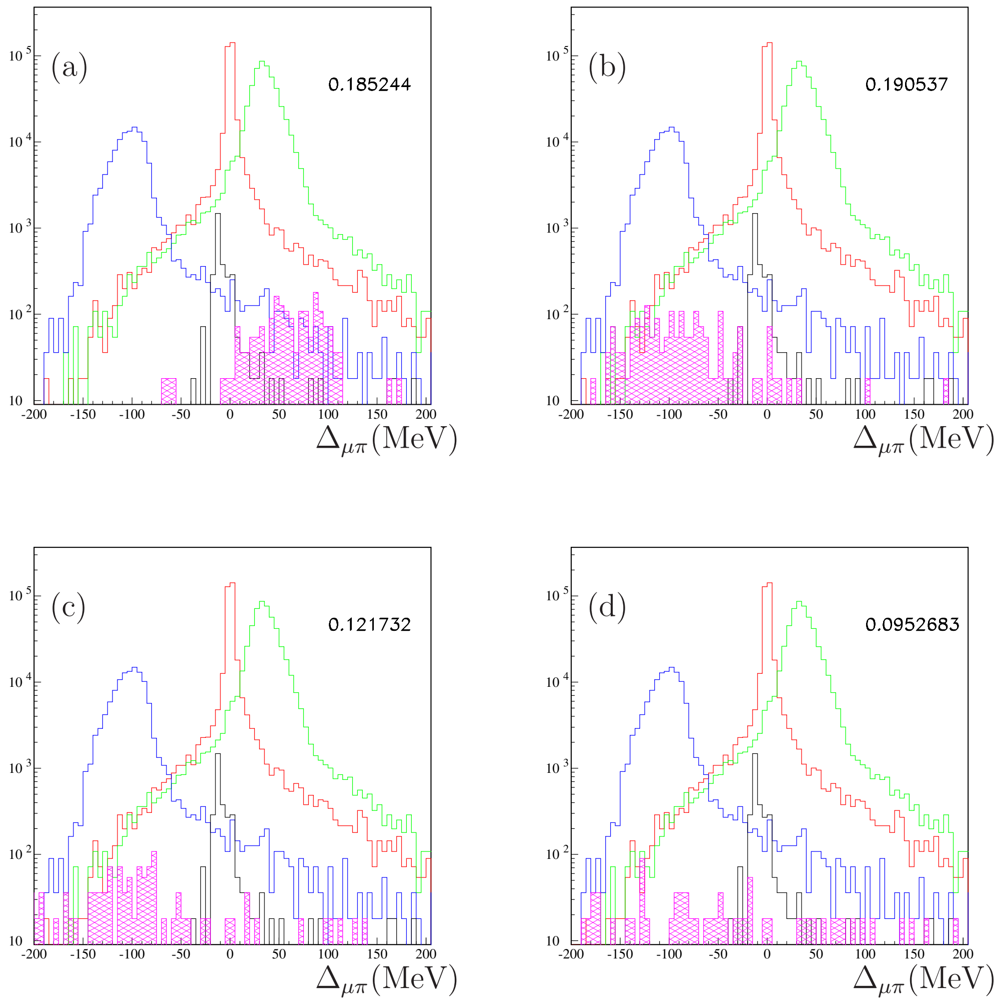

Fig. 18. $\Delta_{\mu\pi}$ distribution for $\pi^{\pm}e^{\mp}\nu$ (green), $\pi^{\pm}\mu^{\mp}\nu$ (red), $\pi^{+}\pi^{-}\pi^{0}$ (blue), and $\pi^{+}\pi^{-}$ (black) from Monte Carlo. The shaded pink histograms indicate the residual background distribution for regeneration (a) Λ, Σ production (b), $K_L \to \pi^0\pi^0\pi^0_{\mathrm{D}}$ (c), other processes (d). The number at the top left of each plot is the background fraction in percent.

region	event fraction	$\sigma(\mathbf{p}_\perp)/\mathbf{p}_\perp$	event fraction	$\sigma(\mathbf{p}_\perp)/\mathbf{p}_\perp$
50 cm $< r_{xy} <$95 cm	0.056	0.017	0.012	0.267
95 cm $< r_{xy} <$180 cm	0.080	0.028	0.014	0.323

Table 4
Parameters used to smear the transverse momentum of tracks in the Monte Carlo.

The results are shown in Table 4.

The data set used to evaluate the smearing parameters (including the set of Monte Carlo events from the 2003 production campaign used for this purpose) has been excluded from the analysis.

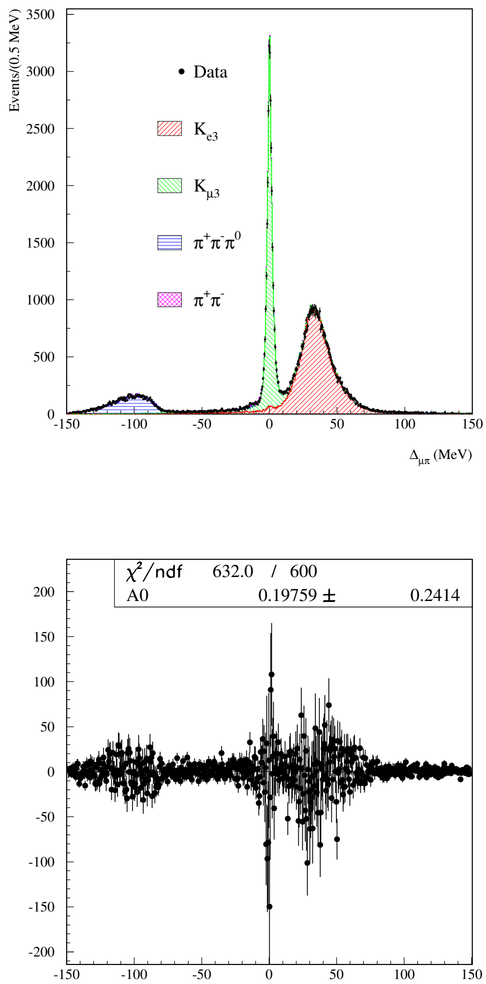

Fig. 19. Top: Distribution of $\Delta_{\mu\pi}$ for a single run period, with fit to Monte Carlo distributions for different decay channels. Bottom: MC − data residuals after fit.

The numbers of $K_L \to \pi^\pm e^\mp \nu$, $K_L \to \pi^\pm \mu^\mp \nu$, and $K_L \to \pi^+\pi^-\pi^0$ events are obtained from fits to the the $|\mathbf{p}_{\rm miss}| - E_{\rm miss}$ distributions with a linear combination of Monte Carlo distributions. An example of such a fit is shown in Fig. 19.

6.5 Study of signal shapes

The shapes of the $\Delta_{\mu\pi}$ distributions have been studied in data, selecting different K_L decay modes using the particle-identification capability of the KLOE calorimeter. Discrimination among the decay modes is based on time-of-flight measurements and energy deposition signatures.

The expected time of flight for a charged secondary from K_L decay is derived from the track momentum and path length for a given mass hypothesis:

$$t_{\exp\,\mathrm{trk}\,i}(m_\ell) = \frac{L_{\mathrm{extr\,trk}\,i}}{\beta_\ell c} \tag{17}$$

where ℓ is e or μ, and β_ℓ is the particle velocity evaluated from the measured track momentum:

$$\beta_\ell = \frac{|\mathbf{p}_\mathrm{c}|}{(\mathbf{p}_\mathrm{c}^2 + m_\ell^2)^{1/2}}.$$

In order to exclude possible systematics resulting from dependence on the determination of the event t_0, we consider the following quantities:

$$\Delta\mathrm{TOF}(\pi^- e^+) = (t_{\mathrm{cl\,trk}\,+} - t_{\exp\,\mathrm{trk}\,+}(m_e)) - (t_{\mathrm{cl\,trk}\,-} - t_{\exp\,\mathrm{trk}\,-}(m_\pi)), \tag{18}$$
$$\Delta\mathrm{TOF}(\pi^+ e^-) = (t_{\mathrm{cl\,trk}\,+} - t_{\exp\,\mathrm{trk}\,+}(m_\pi)) - (t_{\mathrm{cl\,trk}\,-} - t_{\exp\,\mathrm{trk}\,-}(m_e)), \tag{19}$$

where $t_{\mathrm{cl\,trk}\,i}$ is the measured time of cluster i. K_{e3} events are identified and the lepton charge is determined by combining the $\Delta\mathrm{TOF}(\pi^- e^+)$ and $\Delta\mathrm{TOF}(\pi^+ e^-)$ values. The two-dimensional distributions of $\Delta\mathrm{TOF}(\pi^- e^+)$ vs. $\Delta\mathrm{TOF}(\pi^+ e^-)$ are shown in Fig. 20 for K_{e3} events in data and Monte Carlo. On the basis of Monte Carlo studies, the following cuts have been applied to select πe events by charge state:

$$\begin{aligned} \pi^+ e^-: &\quad 2\,\mathrm{ns} < |\Delta\mathrm{TOF}(\pi^- e^+)| < 15\,\mathrm{ns},\ |\Delta\mathrm{TOF}(\pi^+ e^-)| < 0.8\,\mathrm{ns}; \\ \pi^- e^+: &\quad 2\,\mathrm{ns} < |\Delta\mathrm{TOF}(\pi^+ e^-)| < 15\,\mathrm{ns},\ |\Delta\mathrm{TOF}(\pi^- e^+)| < 0.8\,\mathrm{ns}. \end{aligned}$$

These cuts are indicated in Fig. 20 by the red lines.

In addition to time-of-flight information, energy-based cluster information is also used for discrimination among decay modes. The energy deposited and the position of the cluster centroid as a function of the particle momentum have been combined using a neural network. The technique used is discussed in detail in Ref. 12; here we emphasize only the aspects most relevant to the task of particle identification from calorimeter energy deposition. In particular, the value of the ratio between the cluster energy $E_{\mathrm{cl}\,i}$ and the particle momentum $|\mathbf{p}_{\mathrm{c}\,i}|$,

$$E/P_{\mathrm{trk}\,i} \equiv \frac{E_{\mathrm{cl}\,i}}{|\mathbf{p}_{\mathrm{c}\,i}|}, \tag{20}$$

depends on the particle type. In fact, $E_{\mathrm{cl}\,i}$ is proportional to the kinetic energy E_{kin} for completely absorbed particles. For electrons, $E/P_{\mathrm{trk}\,i}(e) \sim 1$, and for muons, $E_{\mathrm{cl}\,i} \sim f_{\mu/e} E_{\mathrm{kin}} = F(|\mathbf{p}_{\mathrm{c}\,i}|) < 1$. For pions, the relation is modified by the

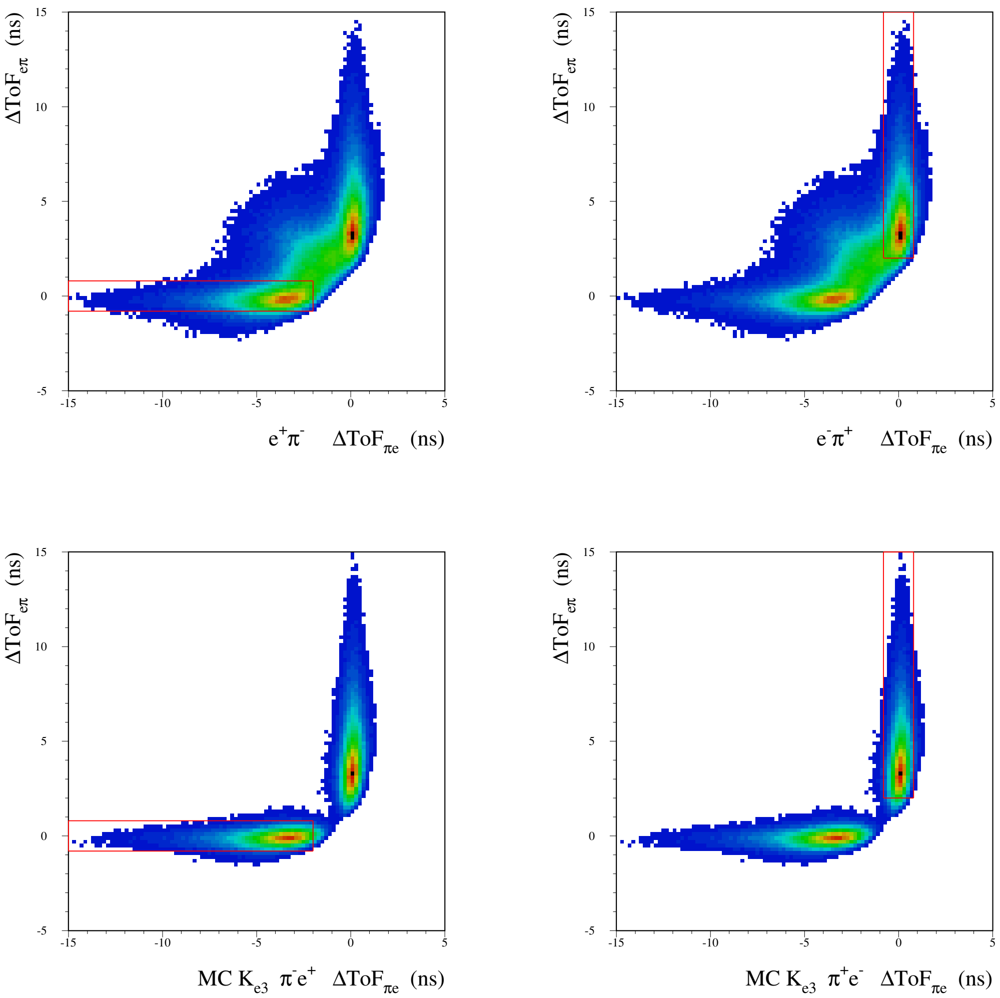

Fig. 20. Scatter plot of $\Delta\mathrm{TOF}(\pi^- e^+)$ vs. $\Delta\mathrm{TOF}(\pi^+ e^-)$ for K_{e3} events in data (top) and Monte Carlo (bottom). The cuts applied for K_{e3} event selection are shown by red lines.

presence of hadronic interactions: $E_{\mathrm{cl}\,i} > f_{\mu/e} E_{\mathrm{kin}}$ only in case of charge-exchange interactions, and and in general $E_{\mathrm{cl}\,i} < f_{\mu/e} E_{\mathrm{kin}}$ because of the undetected energy lost to fragmentation.

The position of the cluster centroid is also very powerful for particle-identification purposes. We compute the distance from the track intersection point on the calorimeter $\mathbf{x}_{\mathrm{imp\,trk}\,i}$ to the position of the cluster centroid $\mathbf{x}_{\mathrm{cl\,trk}\,i}$,

$$L_{\mathrm{cal\,trk}\,i} = |\mathbf{x}_{\mathrm{imp\,trk}\,i} - \mathbf{x}_{\mathrm{cl\,trk}\,i}|. \tag{21}$$

This quantity is expected to be weakly dependent on the particle momentum for

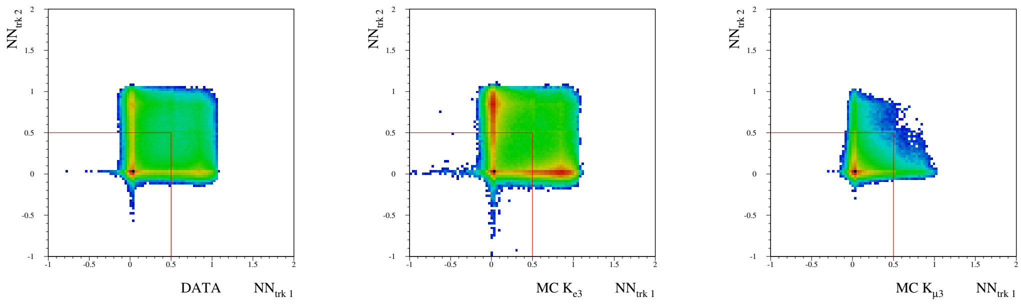

Fig. 21. Neural-net output (left to right) for data without cuts and for MC K_{e3} events and $K_{\mu3}$ events. The inputs to the neural net are the variables $E_{\mathrm{cl}\,i}$, $|\mathbf{p}_{\mathrm{c}\,i}|$, and $L_{\mathrm{cal\,trk}\,i}$. The MLP output value for the positive track is plotted on the abscissa; that for the negative track is plotted on the ordinate. A logarithmic scale is used for the third axis.

electrons:

$$X_{\mathrm{max}} = X_0 \log\left(\frac{E_{\mathrm{kin}}}{E_{\mathrm{c}}}\right) - t,$$

where X_0 is the radiation length, E_{c} is the critical energy, and $t = 1.1$ g cm^{-2}. For muons and pions we have:

$$L_{\mathrm{cal\,trk}\,i} \propto E_{\mathrm{kin}} \tag{22}$$

The neural network has been trained with data samples of $K_L \to \pi^\pm e^\mp \nu$, $K_L \to \pi^\pm \mu^\mp \nu$, $K_L \to \pi^+\pi^-\pi^0$, $K^\pm \to \pi^\pm\pi^0$, and $K^\pm \to \mu^\pm \nu$ events selected by kinematic criteria. The neural network is made of four layers with neuron multiplicities of 3, 30, 20, and 1, respectively. The training procedure attempts to "fit" the value of the multilayer perceptron function (MLP) to 1 for electrons and 0 for muons and pions [13]. The two-dimensional distribution of the MLP output values for the two charged particles is shown in Fig. 21 for data and Monte Carlo. The cut applied to select K_{e3} events is also shown. Figure 22 shows the distribution of the MLP output value for positively charged particles when the negative track is identified as a pion or muon by this technique ($-0.1 < \mathrm{MLP}_{\mathrm{trk}\,-} < 0.1$), for data and Monte Carlo. The agreement between data and Monte Carlo is adequate for our purposes.

To assess the uncertainty on the measurements of the K_{e3} and $K_{\mu3}$ branching ratios arising from limited knowledge of the momentum resolution and of the accuracy of simulation of final-state radiation, we have examined the agreement between the $|\mathbf{p}_{\mathrm{miss}}| - E_{\mathrm{miss}}$ distributions for data and Monte Carlo. The impacts on the results of the fits are estimated by repeating the fits with and without shape corrections to the Monte Carlo. These shape corrections are obtained for the K_{e3} and $K_{\mu3}$ decay modes using samples enriched in these decays selected using

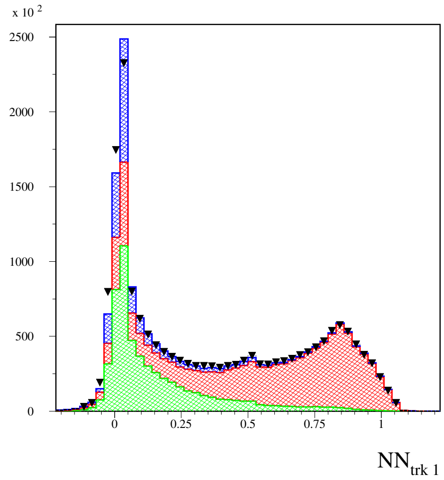

Fig. 22. Comparison of neural-net output for data (black triangles) and Monte Carlo (colored histograms). The distribution for data is obtained by projection of the scatter plot in the first panel of Fig. 21. The red, green, and blue MC histograms show the contributions from K_{e3}, $K_{\mu 3}$, and $\pi^+\pi^-\pi^0$ decays; the results for K_{e3} and $K_{\mu 3}$ decays are obtained by projection of the scatter plots in the second and third panels of Fig. 21.

the particle identification capabilities of the calorimeter as described above. The data-MC comparisons of the $|\mathbf{p}_{\text{miss}}| - E_{\text{miss}}$ distributions for the K_{e3}- and $K_{\mu 3}$-enriched samples are shown in Figs. 23 and 24, respectively. For the K_{e3}-enriched sample, the variable plotted in Fig. 23 is $\Delta_{e\pi}$, while for the $K_{\mu 3}$-enriched sample, the variable plotted in Fig. 24 is $\Delta_{\mu\pi}$. In each case, a shape correction to be applied to the Monte Carlo distributions used in the fits for signal extraction can be obtained from the data-MC ratio of the distributions in the corresponding variable ($\Delta_{e\pi}$ or $\Delta_{\mu\pi}$). The uncertainties in the numbers of signal counts from shape-related sources are estimated by studying the variation in fit results with and without the shape corrections. In all, five configurations have been studied: no shape corrections, shape corrections for all modes, shape corrections only for K_{e3}, shape corrections only for $K_{\mu 3}$, use of the alternative πe mass hypothesis.

7 $K_L \to \pi^0\pi^0\pi^0$ decays

The position of the K_L vertex for $K_L \to \pi^0\pi^0\pi^0$ decays is obtained from the arrival times of the photons at the calorimeter. The method is fully described in Refs. 4 and 8. The position of the K_L vertex is assumed to be along the K_L line of flight as reconstructed from the tagging $K_S \to \pi^+\pi^-$ decay. The arrival time of each photon gives an independent determination of the path length of the K_L, L_K, up to a two-fold ambiguity. One solution is easily discarded. The final value of L_K is obtained from the weighted average of the different measurements. The accuracy of the method is checked using $K_L \to \pi^+\pi^-\pi^0$ decays, by comparing the

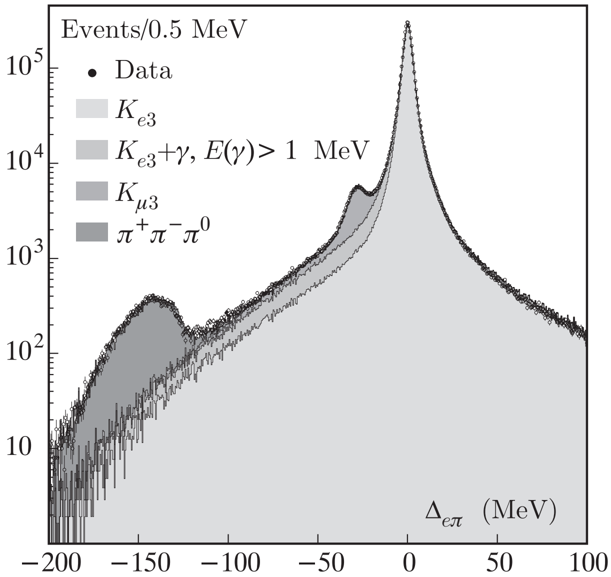

Fig. 23. Distribution of $\Delta_{e\pi}$ for a sample enriched in K_{e3} events using electron identification by calorimeter time-of-flight and energy deposition measurements, for the entire data sample and for Monte Carlo. The contribution from $K_{e3}\gamma$ events with $E_\gamma > 1$ MeV is also shown.

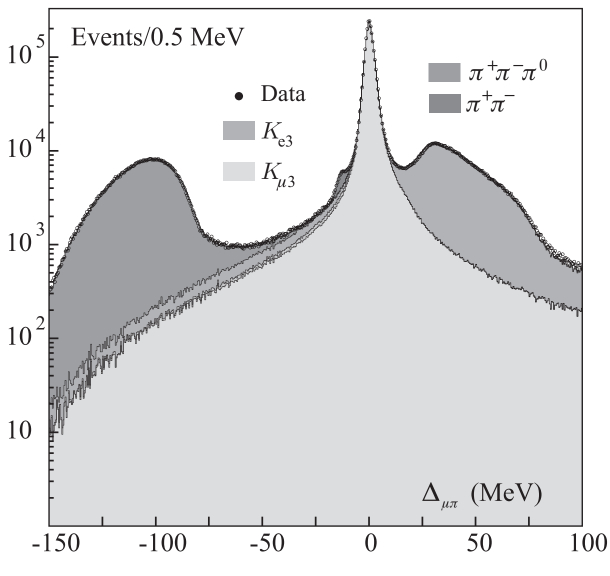

Fig. 24. Distribution of $\Delta_{\mu\pi}$ for a sample enriched in $K_{\mu3}$ events using μ/π identification by calorimeter time-of-flight measurements and energy deposition pattern, for the entire data sample and for Monte Carlo. The contributions from different channels are illustrated.

position of the K_L decay vertex from the reconstruction of the tracks from the $\pi^+\pi^-$ pair with the position obtained from photon arrrival-time measurements. Decays to $\pi^+\pi^-\pi^0$ are also used to measure the single-photon efficiency in order to correct the Monte Carlo simulation.

In this section, we discuss the measurement of the $K_L \to \pi^0\pi^0\pi^0$ branching ratio. The essential point is to determine the ratio of the number of $K_L \to \pi^0\pi^0\pi^0$ decays, denoted by N_k in Eq. (1), to the total number of K_L's in the sample, N_{tag}. The event counting is based on the reconstruction of the $K_L \to \pi^0\pi^0\pi^0$ vertex from single-photon vertex information. Important considerations are the calorimeter calibrations and the estimation of the spatial resolution. Because our measurement essentially reduces to counting photon clusters, we have studied the single-photon efficiency of the calorimeter in detail. The single-photon efficiency is estimated using the same technique both for Monte Carlo and for data; the values for ε_{rec} used in the analysis are obtained from Monte Carlo and corrected using the data-Monte Carlo efficiency ratio. A photon energy threshold, $E^{\gamma}_{\text{threshold}}$, of 20 MeV has been used in this analysis.

7.1 Single-photon vertex reconstruction quality

As stated above, the comparison of the charged-particle and photon vertex positions in $K_L \to \pi^+\pi^-\pi^0$ decays is used to study the performance of the single-photon vertex reconstruction. In particular, we obtain timescale corrections for single photons, which corresponds to calibrating the K_L path-length measurement, and study the resolution with which the path length is reconstructed.

7.1.1 Selection of $K_L \to \pi^+\pi^-\pi^0$ decays

The reconstruction of the tagging $K_S \to \pi^+\pi^-$ decay is described in Sec. 4. We apply the following cuts to select $K_L \to \pi^+\pi^-\pi^0$ decays.

First of all, we select events with a reconstructed vertex from the decay of a K_L into charged particles. The missing momentum in such events is

$$\mathbf{p}_{\text{miss}} = \mathbf{p}_{K_L} - \mathbf{p}_{\text{trk}\,1} - \mathbf{p}_{\text{trk}\,2}, \tag{23}$$

where $\mathbf{p}_{K_L}$ is the K_L momentum as obtained from reconstruction of the tagging $K_S \to \pi^+\pi^-$ decay, and $\mathbf{p}_{\text{trk}\,1}$ and $\mathbf{p}_{\text{trk}\,2}$ are the momenta of the positive and negative tracks associated to the K_L line of flight. The missing energy is given by the expression

$$E_{\text{miss}} = E_{K_L} - E_{\pi^+} - E_{\pi^-}, \tag{24}$$

where E_{K_L} is the energy of the K_L as calculated from $\mathbf{p}_{K_L}$, and E_{π^+} and E_{π^-} are the energies calculated for the positive and negative tracks, assigning the charged-pion mass to each. Using Eqs. (23) and (24), we obtain the missing mass

$$M^2_{\rm miss} = E^2_{\rm miss} - |\mathbf{p}_{\rm miss}|^2, \tag{25}$$

and select $K_L \to \pi^+\pi^-\pi^0$ events by applying the cut

$$|M_{\rm miss} - M_{\pi^0}| < 4\,\mathrm{MeV},$$

corresponding roughly to two standard deviations in the missing-mass distribution.

The sample used for single-photon efficiency determination is finally selected by requiring one tagging photon cluster having a neutral vertex within 5σ of the track vertex.

For studies of the spatial resolution for photon-vertex reconstruction, calibration of the absolute time scale, and the accuracy of the event t_0 determination, after the cut on the missing mass, we search for the two photon clusters from the π^0. The expected time for each cluster is obtained as

$$t_{\exp\,\gamma\,i} = L_{\gamma\,i}/c + L_{K_L}/\beta_{K_L}c \tag{26}$$

where $i = 1, 2$ is the cluster index, $L_{\gamma\,i}$ represents the distance traveled by the photon, i.e., the distance from the track vertex to the cluster centroid,[2] L_{K_L} is the distance between the ϕ decay position and the track vertex, and $\beta_{K_L}c$ is the velocity of the K_L, obtained from the two-body kinematics of the $\phi \to K_S K_L$ decay and the known values of $\sqrt{s}$, $\mathbf{p}_\phi$, and $\mathbf{p}_{K_S}$ as described in Sec. 4.

The expression for the expected energy of photon i can be obtained from kinematic considerations:

$$E_{\exp\,\gamma\,i} = \frac{m^2_{\pi^0}}{2(E_{\rm miss} - \mathbf{p}_{\rm miss}\cdot\boldsymbol{\omega}_{\gamma\,i})}, \tag{27}$$

where $\boldsymbol{\omega}_{\gamma\,i}$ is the unit vector describing the photon momentum, obtained from the positions of the cluster and of the track vertex. We use Eq. (27) in the calculation of the two-photon invariant mass, $M_{\gamma\,12} = 2E_{\exp\,\gamma\,1}E_{\exp\,\gamma\,2}\cos(1-\theta_{\gamma\,12})$, where $\theta_{\gamma\,12}$ is the opening angle between the photon clusters with respect to the K_L vertex position. To select $K_L \to \pi^+\pi^-\pi^0$ events, we require $|M_{\gamma\,12} - m_{\pi^0}| < 15\,\mathrm{MeV}$.

[2] We use the position of the track vertex because it is reconstructed with greater precision.

We also obtain $\vartheta_{\gamma\,12}$, the angle between the photon momenta in the rest frame of the π^0,

$$\cos\vartheta_{\gamma\,12} = 1 - \frac{(1-\beta_{\pi^0}^2)(1-\cos\theta_{\gamma\,12})}{(1-\beta_{\pi^0}\cos\alpha_{\gamma\pi^0\,1})(1-\beta_{\pi^0}\cos\alpha_{\gamma\pi^0\,2})},$$

where β_{π^0} is the velocity of the π^0 in the laboratory, as evaluated from the missing momentum at the track vertex, and $\alpha_{\gamma\pi^0\,1}$ and $\alpha_{\gamma\pi^0\,2}$ are the angles between the momentum of the π^0 and the momenta of photons 1 and 2. To select $K_L \to \pi^+\pi^-\pi^0$ events, we require $\cos\vartheta_{\gamma\,12} < -0.9$.

In addition to kinematic criteria, information about the cluster times is used at the event-selection stage. For each photon, we calculate $\Delta t_{\gamma\,i}$, the difference between the expected and measured cluster times:

$$\Delta t_{\gamma\,i} = t_{\exp_{\gamma\,i}} - t_{\mathrm{cl}\gamma\,i} \tag{28}$$

As noted in Sec. 4.2, the event-start time, t_0, is determined on an event-by-event basis using the pion tracks from the K_S. If the bunch crossing giving rise to the event is incorrectly identified, $\Delta t_{\gamma\,i}$ will differ from zero by an integer multiple of the time between adjacent bunch crossings (or more precisely, adjacent RF buckets):

$$\Delta t_{\gamma\,i} = n_{\gamma\,i} T_{\mathrm{RF}}$$

where n is an integer number and $T_{\mathrm{RF}} = 2.7$ ns. To ensure that the two photons come from the decay of the same π^0, we examine the difference between $\Delta t_{\gamma\,1}$ and $\Delta t_{\gamma\,2}$,

$$\Delta(\Delta t) \equiv \Delta t_{\gamma\,1} - \Delta t_{\gamma\,2} = (t_{\exp_{\gamma\,1}} - t_{\mathrm{cl}\gamma\,1}) - (t_{\exp_{\gamma\,2}} - t_{\mathrm{cl}\gamma\,2}). \tag{29}$$

While cuts on the individual values of $\Delta t_{\gamma\,i}$ select only events in which the bunch-crossing assignment is correct, the cut on $\Delta(\Delta t)$ allows us to identify photon pairs from the decay of the π^0 in $K_L \to \pi^+\pi^-\pi^0$ events without biasing the sample used to study the accuracy of the bunch-crossing assignment. Figure 25 shows the distribution of $\Delta t_{\gamma\,i}$ for events selected by the aforementioned kinematic cuts, subject to the condition that

$$|\Delta(\Delta t)| < 1\,\mathrm{ns}.$$

We fit this distribution using a function consisting of the sum of three double-Gaussians, shown as the red line in the figure. The three peaks are centered at -2.7, 0, and 2.7 ns; from their integrals we determine that the probability of

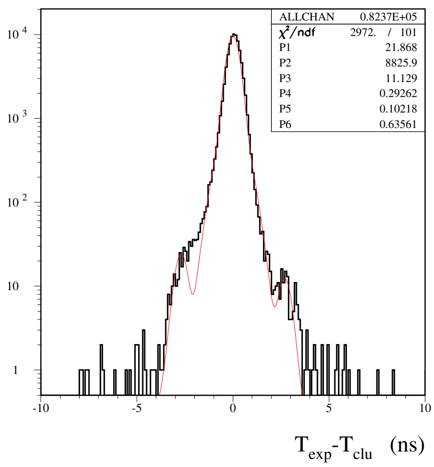

Fig. 25. Difference between the expected and measured cluster times for photon clusters from $K_L \to \pi^+\pi^-\pi^0$ decays. The red line represents a fit with the sum of the three double-Gaussians. The two components of each double-Gaussian have a common mean; the three peaks are centered at -2.7, 0, and 2.7 ns. The six free parameters in the fit are then the overall normalization of each peak, $P1$–$P3$; the standard deviations of the two Gaussian contributions to each peak, $P4$ and $P5$ (the same for all three peaks); and the relative weight of the two Gaussian contributions for each peak, $P6$ (again, the same for all three peaks).

obtaining $\Delta n = -1$ is about 0.25% and that the probability of obtaining $\Delta n = 1$ is about 0.125%. In more than 99.6% of the events, the determination of the event t_0 is correct.

7.1.2 Spatial calibration and resolution

A sample of $K_L \to \pi^+\pi^-\pi^0$ decays selected as described in the previous section is used to study the reconstruction quality for single-photon vertices. In particular, for each event, the distance between the track vertex and the single-photon vertex,

$$\Delta R \equiv L_{K_L} - R_{\gamma\, i}, \tag{30}$$

is calculated, where L_{K_L} is the same quantity appearing in Eq. (26) and $R_{\gamma\, i}$ is the distance between the i^{th} photon and the decay point of the ϕ . Figure 26 shows the mean value of ΔR as a function of L_{K_L} as determined from the track-vertex position. (The track-vertex position is used in order both to obtain independence from the timing measurements, which are the object of calibration, and to benefit from the finer spatial resolution of the measurement of the track-vertex position.)

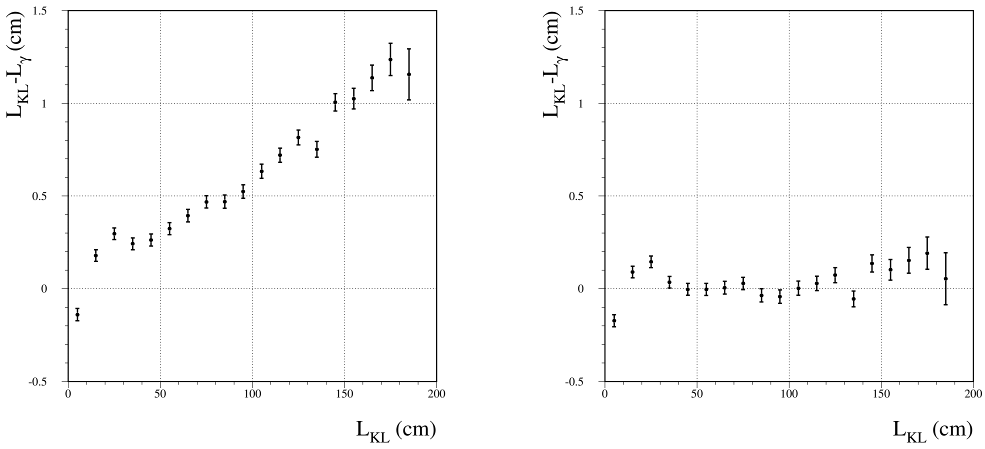

Fig. 26. Mean value of ΔR, the distance between the track vertex and the single-photon vertex, as a function of L_{K_L}, for $K_L \to \pi^+\pi^-\pi^0$ events. The points represent 10 cm bins in L_{K_L} as determined from the track-vertex position. For each point, the mean value of ΔR was obtained from a Gaussian fit to the ΔR distribution. The plot at left has been generated using the PDG value of the K_L mass; for the plot at right, the KLOE value for the K_L mass has been used. These plots were obtained without cuts to restrict the fiducial volume. However, in order to obtain reasonable fits, we required at least 400 events per 10 cm bin; as a result, some bins were eliminated.

The mean values of ΔR are very sensitive to the value of the neutral-kaon mass used for the calculation of β_{K_L}. We use the KLOE value of m_{K^0} [6]. A fractional change of 0.6% in the K_L momentum is observed if the PDG value of m_{K^0} is used:

$$\frac{\delta p}{p} \sim \frac{1}{\beta^2} \cdot \frac{\delta m_{K^0}}{m_{K^0}}.$$

Indeed, a corresponding slope of 0.6% is observed in the dependence of ΔR on L_{K_L}, as expected since $L_K \propto \beta$ in the construction of the single-photon vertex. We therefore have confirmation of the KLOE measurement of m_{K^0} from the comparison of the photon arrival-time measurements with the measurement of the position of the track vertex in $K_L \to \pi^+\pi^-\pi^0$ events.

Using the same method, we have also studied the energy calibration. We define

$$\Delta E \equiv E_{\exp\,\gamma\,i} - E_{\mathrm{cl}\,\gamma\,i}, \tag{31}$$

where $E_{\exp\,\gamma\,i}$ is the same quantity in Eq. (27) and $E_{\mathrm{cl}\,\gamma\,i}$ is the energy of the i^{th} photon measured by the calorimeter. The mean value of ΔE as a function of $E_{\exp\,\gamma\,i}$ is plotted in Fig. 27. The dependence of the mean value of ΔE on $E_{\exp\,\gamma\,i}$ is weak for both data and Monte Carlo. In data, the photon energy tends to

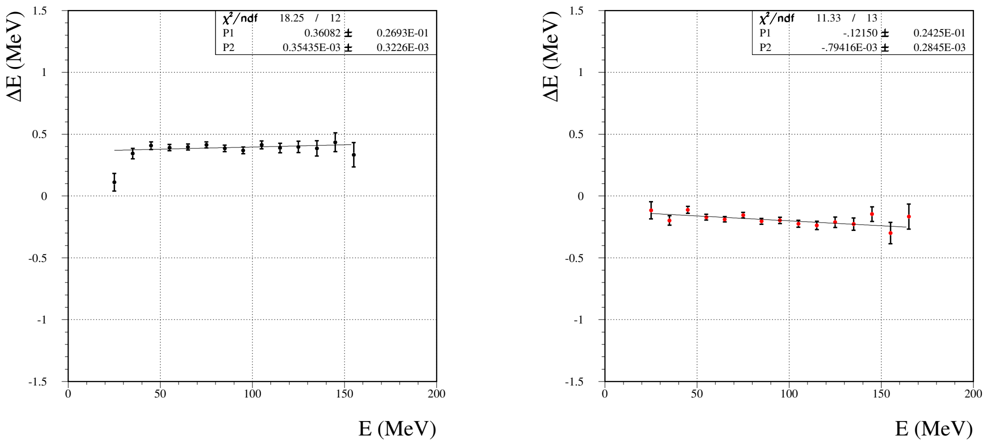

Fig. 27. Mean value of ΔE, the difference between the expected and measured photon energies, as a function of the expected photon energy, in $K_L \to \pi^+\pi^-\pi^0$ events, for data (left) and Monte Carlo (right). The points represent ~ 7 MeV bins in the expected photon energy; the means are obtained from Gaussian fits to the ΔE distributions for each bin. The black lines represent linear fits to ΔE vs. E_{exp}.

be slightly overestimated, while in Monte Carlo, the photon energy tends to be slightly underestimated; in either case, the discrepancies are below about 0.5 MeV.

In addition, $K_L \to \pi^+\pi^-\pi^0$ events have been used to study the spatial resolution for single-photon vertex reconstruction, both as a function of the radial position of the track vertex, R_t, and as a function of the measured photon energy, E_{cl}. Figure 28 shows the dependence of ΔR (Eq. [30]) on R_t. The spatial resolution for single-photon vertex reconstruction varies between 2 and 2.5 cm, and increases slightly with R_t. Good agreement between data and Monte Carlo is observed. Figure 29 shows the dependence of ΔR on E_{cl}, both for data and for Monte Carlo. The spatial resolution for single-photon vertex reconstruction is better than 2.5% for photon clusters with $E > 50$ MeV. To parameterize the spatial resolution for use in the selection of $K_L \to \pi^0\pi^0\pi^0$ events, we fit the data in the figure with an empirical function of the form

$$\sigma_{R_{\gamma\, i}} = \left(\sigma_1^2 + \frac{\sigma_2^2}{E_{\mathrm{cl}\,\gamma\, i}^{3/2}} \right)^{1/2}, \tag{32}$$

where σ_1 and σ_2 are free parameters separately obtained for each data period.

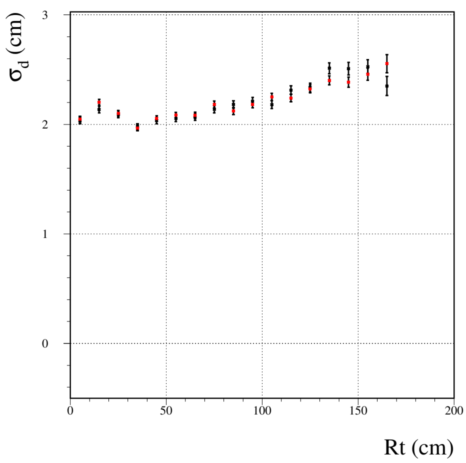

Fig. 28. Spatial resolution for single-photon vertices as a function of the radial position R_t of the track vertex in $K_L \to \pi^+\pi^-\pi^0$ events, for data (black) and Monte Carlo (red). The points represent the values obtained for the standard deviation from Gaussian fits to the ΔR distributions for 10 cm bins in R_t.

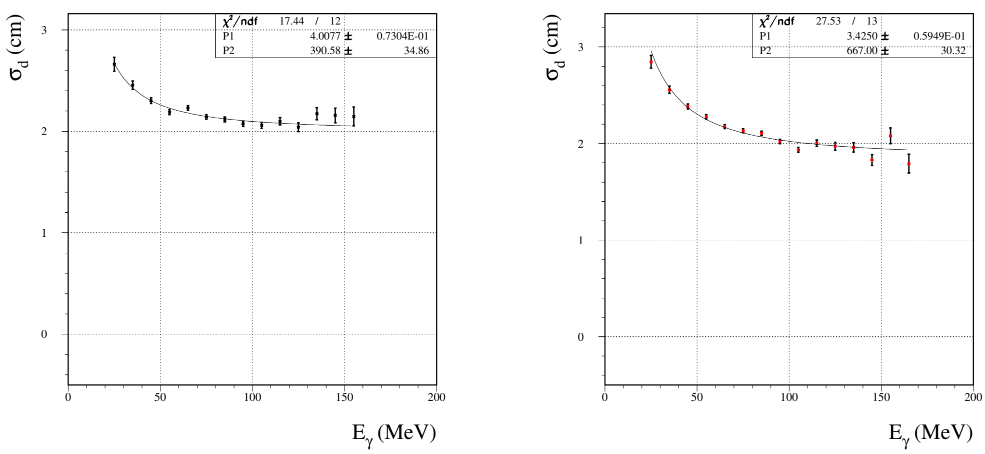

Fig. 29. Spatial resolution for single-photon vertices as a function of measured photon energy in $K_L \to \pi^+\pi^-\pi^0$ decays, for data (left) and Monte Carlo (right). The points represent the values obtained for the standard deviation from Gaussian fits to the ΔR distributions for bins of about 7 MeV in the measured photon energy. The black lines show the results of the fit with Eq. (32).

7.2 Single-photon vertex reconstruction efficiency

After calibration of the single-photon vertex position response for data and Monte Carlo, and after determination of the spatial resolution as a function of the measured photon energy, we have determined the efficiency for reconstruction of single-photon vertices. Again, we use $K_L \to \pi^+\pi^-\pi^0$ events, selected using the criteria of Sec. 7.1.1.

The single-photon vertex reconstruction efficiency is determined from the ratio of the number of $K_L \to \pi^+\pi^-\pi^0$ events in which both photons from the $\pi^0 \to \gamma\gamma$ decay are detected to the number of events in which at least one photon is detected:

$$\varepsilon_\gamma = \frac{N_{\gamma\,\mathrm{rec}}}{N_{\gamma\,\mathrm{tag}}}, \tag{33}$$

where $N_{\gamma\,\mathrm{tag}}$ is the number of events in which at least one photon is detected (we call this the *tagging* photon, γ_{tag}), and $N_{\gamma\,\mathrm{rec}}$ is the number of events in which the second photon (γ_{rec}) is detected. The algorithm is divided into two steps. First, using the measured momentum of γ_{tag} and the kinematic constraints from the $\pi^0 \to \gamma\gamma$ decay, we reconstruct the expected momentum for the second photon, γ_{exp}. Second, we search for the second photon, γ_{rec}; if found, we determine whether its momentum is compatible with that of γ_{exp}.

First, we search for the tagging photon. We select only events in which there is at least one cluster reconstructing as a single-photon vertex with $\Delta R \equiv L_{K_L} - R_\gamma$ (Eq. [30]) within a $5\sigma_R$ window of L_{K_L}, the position of the track-vertex, using Eq. (32) for the evaluation of σ_R. We treat all such photons as γ_{tag} in turn. Using the track-vertex position and the position of the cluster for γ_{tag}, we determine the unit-vector describing the momentum of the tagging photon, $\boldsymbol{\omega}_{\gamma\,\mathrm{tag}}$. We then perform the same kinematic analysis described in Sec. 7.1.1: knowing the momenta of the K_L and of the charged-pion tracks, we calculate the missing momentum and missing energy, and, assuming that the photon comes from the decay of a π^0, obtain the energy of the tagging photon as (compare Eq. [27]):

$$E_{\gamma\,\mathrm{tag}} = \frac{m_{\pi^0}^2}{2(E_{\mathrm{miss}} - \mathbf{p}_{\mathrm{miss}} \cdot \boldsymbol{\omega}_{\gamma\,\mathrm{tag}})}.$$

From these quantities, we construct the momentum vector and energy of γ_{exp}:

$$\boldsymbol{\omega}_{\gamma\,\mathrm{exp}} = \frac{\mathbf{p}_{\mathrm{miss}} - E_{\gamma\,\mathrm{tag}} \cdot \boldsymbol{\omega}_{\gamma\,\mathrm{tag}}}{E_{\mathrm{miss}} - E_{\gamma\,\mathrm{tag}}} \tag{34}$$

and

$$E_{\gamma\,\mathrm{exp}} = E_{\mathrm{miss}} - E_{\gamma\,\mathrm{tag}}. \tag{35}$$

We select events in which the direction of the expected photon does not intersect the beam pipe, and extrapolate this direction to obtain the point of impact on the calorimeter. For this purpose, we divide the calorimeter into three regions:

- the barrel, $R_{xy} > 200$ cm and $|z| < 150$ cm;
- the endcaps, 25 cm $< R_{xy} <$ 175 cm and $z >$ 170 cm or $z < -170$ cm;
- the barrel-endcap overlap region, $R_{xy} > 200$ cm and $|z| > 150$ cm, or $R_{xy} >$ 175 cm and $|z| > 170$ cm.

In order to avoid incorrectly assigning clusters from charged particles to γ_{exp}, we use the following procedure. First of all, we extrapolate the reconstructed tracks from the $K_S \to \pi^+\pi^-$ and $K_L \to \pi^+\pi^-\pi^0$ decays to the calorimeter and obtain the corresponding impact points. The smallest distance between the impact point of γ_{exp} and the impact points of any of these reconstructed tracks must be greater than 8 cm in each of the three coordinates x, y, z and greater than 30 cm in overall three-dimensional distance.

Finally, if a candidate cluster corresponding to the expected photon is found, we apply the following criteria to ensure its compatibility with γ_{exp}. The position of the corresponding single-photon vertex must satisfy $\Delta R \equiv |R_{\gamma\,\mathrm{tag}} - R_{\gamma\,\mathrm{rec}}| < 5\sigma_R$ (Eq. [30]), where σ_R is evaluated as the quadrature sum of the values from Eq. (32) for γ_{tag} and γ_{exp}. Moreover, using the position of the cluster corresponding to γ_{rec} and the position of the track vertex, we obtain the unit vector describing the momentum of γ_{rec}, $\boldsymbol{\omega}_{\gamma\,\mathrm{rec}}$, and evaulate the angle between the momenta of γ_{exp} and γ_{rec}:

$$\cos\vartheta_{\mathrm{rec\,exp}} = \boldsymbol{\omega}_{\gamma\,\mathrm{rec}} \cdot \boldsymbol{\omega}_{\gamma\,\mathrm{exp}} \tag{36}$$

To count a photon as found for the purposes of the efficiency calculation (i.e., for the numerator of Eq. [33]), we require $\cos\vartheta_{\mathrm{rec\,exp}} > 0.6$ ($\vartheta_{\mathrm{rec\,exp}} < 53°$) for data and $\cos\vartheta_{\mathrm{rec\,exp}} > 0.65$ ($\vartheta_{\mathrm{rec\,exp}} < 49°$) for Monte Carlo. (The latter cut is a little tighter because finer resolution is obtained in Monte Carlo events.) Moreover, we require that the cluster be in the same region (barrel, endcap, or overlap) in which we expect it to be.

We have estimated the single-photon vertex reconstruction efficiency for each of the three regions, both as a function of the expected photon energy and as a function of the radial position of the single-photon vertex for the tagging photon. In Figs. 30, 31, and 32, we show the comparison between the efficiencies obtained for data and Monte Carlo for the barrel, endcap, and overlap regions, respectively.

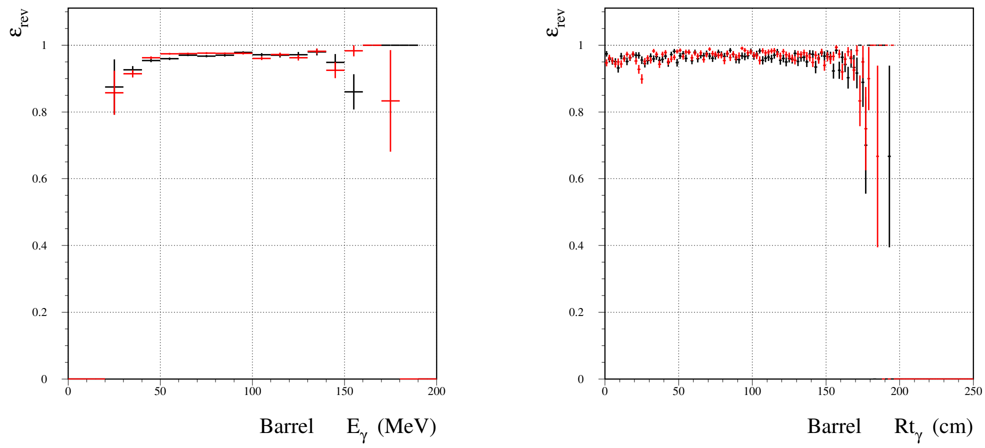

Fig. 30. Left: Single-photon efficiency for the calorimeter barrel, as a function of expected photon energy. Right: Single-photon efficiency for the barrel as a function of the radial position of the single-photon vertex for the tagging photon. In both panels, black (red) points represent data (Monte Carlo).

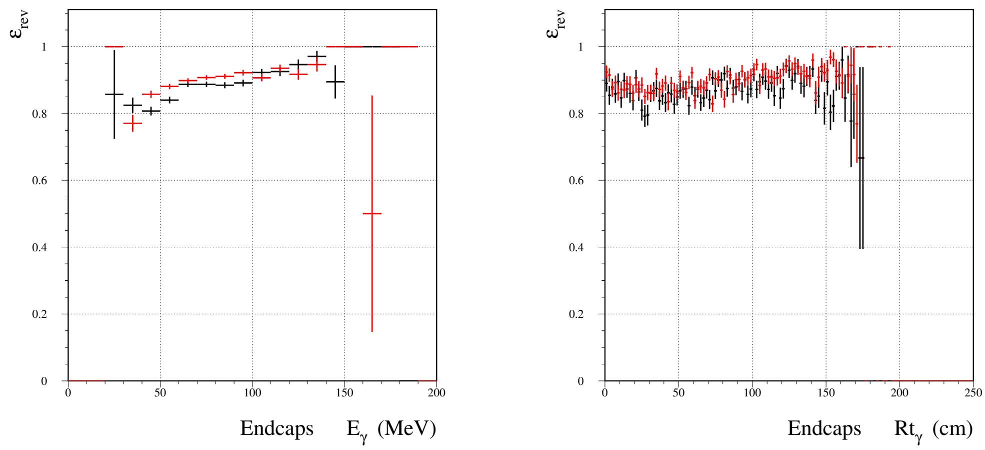

Fig. 31. Left: Single-photon efficiency for the calorimeter endcaps, as a function of expected photon energy. Right: Single-photon efficiency for the barrel as a function of the radial position of the single-photon vertex for the tagging photon. In both panels, black (red) points represent data (Monte Carlo).

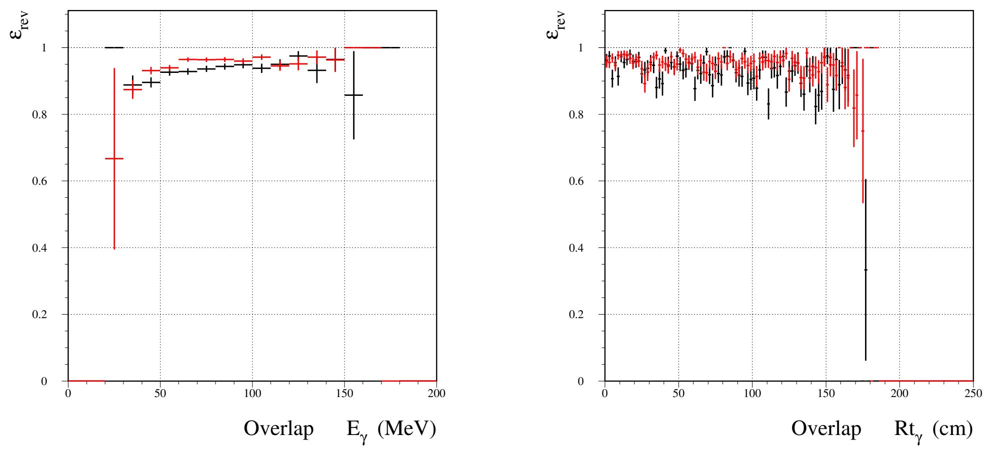

Fig. 32. Left: Single-photon efficiency for the overlap regions between calorimeter barrel and endcaps, as a function of expected photon energy. Right: Single-photon efficiency for the barrel as a function of the radial position of the single-photon vertex for the tagging photon. In both panels, black (red) points represent data (Monte Carlo).

In estimating the single-photon efficiency, we have not taken Dalitz decays ($\pi^0 \to e^+e^-\gamma$) into account. The branching ratio for such decays is about 1.2%. We therefore expect that the asymptotic value of the single-photon efficiency will be $\sim$98.8% Figures 30, 31, and 32 suggest that the limiting value at high energy is instead $\sim$95%. Evidently, the observable efficiency is not determined only by the probability for the π^0 to undergo Dalitz decay. There are indeed important geometric effects, as evinced by the dependence of the single-photon vertex reconstruction efficiency on the radial position of the π^0 decay vertex. For the barrel and overlap regions, the correlation between the single-photon efficiency and radial position of the π^0 vertex is not strong; for the endcaps, instead, a strong correlation is observed. This is a reflection of the fact that the farther the π^0 decay vertex is from dead elements such as the beam pipe or the QCALs (from which we do not use the signal for this analysis), the more likely it is that the photons will be detected. Moreover, in the algorithm for the determination of the efficiency, photons must be found in the same region of the calorimeter (barrel, endcaps, or overlap) in which they are expected to be found. This requirement is independent of the cut on $\cos\vartheta_{\rm rec\,exp}$, and therefore further restricts the spatial acceptance. The efficiencies obtained by this method cannot therefore be used to make absolute efficiency corrections; in the analysis, we form the ratio of data to Monte Carlo efficiencies and use this ratio to correct the absolute efficiency obtained from the Monte Carlo.

As expected, the efficiency increases with photon energy. The dependence of the efficiency on photon energy is seen to be different in each of the three regions. In the barrel, the efficiency quickly rises and attains a plateau value of $\sim$95% for photon energies above 50 MeV. There is a slight degradation of the measured efficiency for photon energies around 150 MeV and above. This effect can be attributed to the poor reconstruction of the very-low-energy tagging photon. In the endcaps, this pleateau does not appear to be reached except possibly for photons with the very highest energies allowed. In the overlap regions, the rise of the efficiency with respect to energy is less pronounced than it is in the endcaps, but the plateau is reached at a higher value of the energy than observed for the barrel, and the plateau efficiency is lower than 95%.

The goal of the single-photon efficiency studies is to obtain the data-MC ratio of efficiencies, which is used to correct the MC-based photon-counting efficiency estimate in the analysis. From Figs. 30, 31, and 32, it is seen that the dependence of the efficiency on the radial position of the single-photon vertex for the tagging photon is similar for data and Monte Carlo, and that the efficiency in Monte Carlo events is slightly higher than it is in data, particularly for low photon energies. The data-MC efficiency ratios as a function of expected photon energy are shown in Fig. 33 for each of the three regions. The black lines in the figure show fits to the form

$$f_{\gamma\,\mathrm{corr}} = p_1 + p_2\,E_{\mathrm{cl}\,\gamma} - \frac{p_2}{220\ \mathrm{MeV}} E_{\mathrm{cl}\,\gamma}^2 \tag{37}$$

for photon energies between 20 and 110 MeV, and

$$f_{\gamma\,\mathrm{corr}} = p_1 + 110\ \mathrm{MeV}\cdot p_2 - \frac{p_2}{220\ \mathrm{MeV}}\cdot {E_{\mathrm{cl}}}_{\gamma}^{2} \tag{38}$$

for photon energies greater than 110 MeV. p_1 and p_2 are free parameters in the fits. The function used to correct the Monte Carlo efficiency is applied during photon counting and neutral-vertex reconstruction for $K_L \to \pi^0\pi^0\pi^0$ decays, as described in Sec. 7.3.

7.3 Reconstruction of the multiphoton vertex

7.3.1 Reconstruction procedure

$K_L \to \pi^0\pi^0\pi^0$ decays are reconstructed by joining several single-photon vertices into a single multiphoton vertex. For each pair of single-photon vertices along the line of flight of the K_L, we calculate the quantity

$$D_{\gamma i \gamma j} = \frac{|R_{\gamma i} - R_{\gamma j}|}{\sigma_{\gamma i \gamma j}} \tag{39}$$

where the indices i and j run over the set of clusters not associated to tracks ($i \neq j$), $R_{\gamma i}$ is the projected distance of the i^{th} single-photon vertex along the

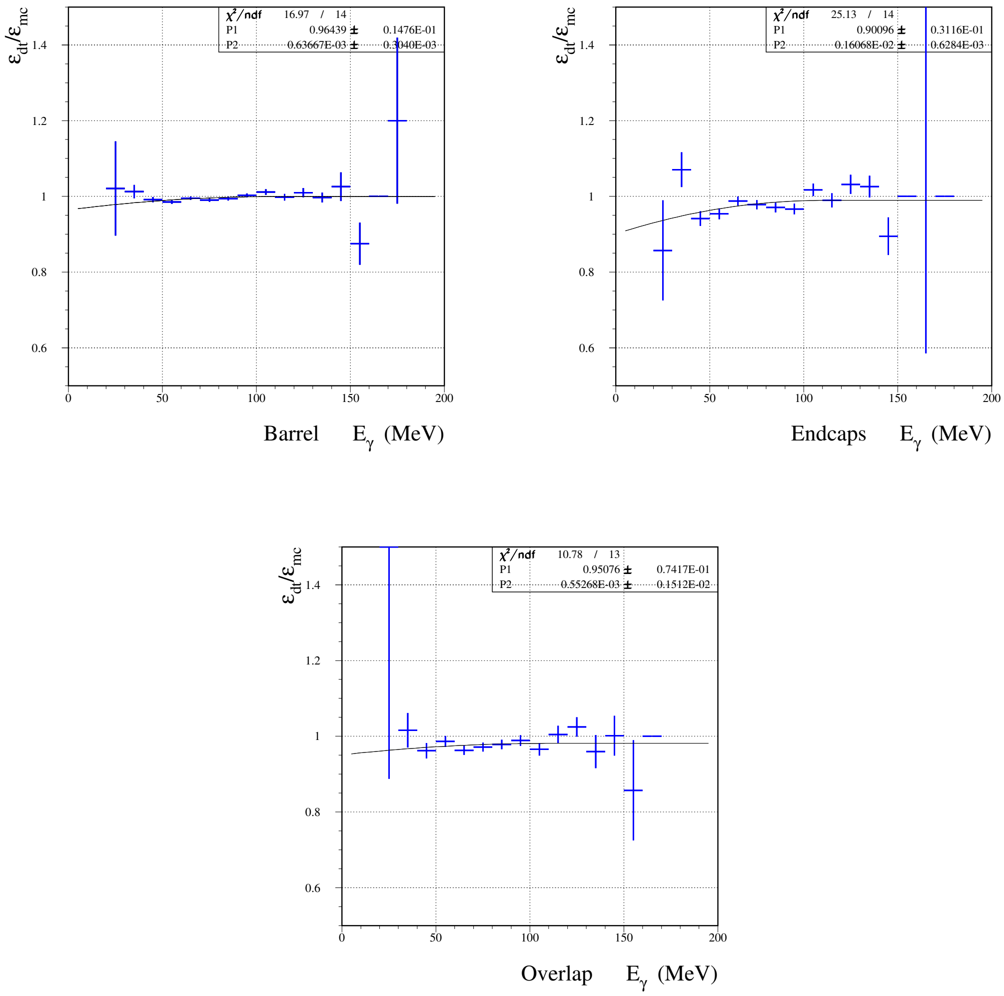

Fig. 33. Data-Monte Carlo ratio of single-photon vertex reconstruction efficiencies as a function of expected photon energy for each of the three regions (barrel, endcaps, and overlap). The black lines show the results of the fits used to obtain the corrections to the Monte Carlo efficiency for the purposes of photon counting.

K_L line of flight, and $\sigma_{\gamma i \gamma j} = (\sigma^2_{\gamma i} + \sigma^2_{\gamma j})^{1/2}$, with $\sigma_{\gamma i}$ the position resolution for the i^{th} single-photon vertex, evaluated from Eq. (32). We then combine all single-photon vertices which satisfy the condition

$$D_{\gamma i \gamma j} < 5. \tag{40}$$

The resulting collection of single-photon vertices (which we refer to as a *chain*) may contain two single-photon vertices more than 5σ apart, as long as each is within 5σ of some other vertex within the chain. If no chain can be assembled, the event is discarded. If more than one chain is successfully assembled, we select the one with the greater number of associated photons. If two chains have the same number of photons, we select that with the greater total energy, as calculated from the sum of the energies of the associated photon clusters. We refer to the number of single-photon vertices associated with the chain as the *photon multiplicity*. $K_L \to \pi^0\pi^0\pi^0$ decays are identified by selecting events with photon multiplicities greater than or equal to three.

The position of the multiphoton vertex for $K_L \to \pi^0\pi^0\pi^0$ is reconstructed as

$$\mathbf{x}_{K_L} = \mathbf{x}_\phi + \hat{\mathbf{p}}_{K_L} \left(\frac{1}{\sigma_{\gamma\,\mathrm{tot}}} \sum_{i=1}^{n} R_{\gamma\,i}/\sigma^2_{\gamma\,i} \right) \tag{41}$$

where $i \in 1 \ldots n$ indexes the single-photon vertices belonging to the chain after application of the merging procedure described in the next section,

$$\sigma_{\gamma\,\mathrm{tot}} \equiv \left(\sum_{i=1}^{n} 1/\sigma^2_{\gamma\,i} \right)^{-1/2},$$

$\sigma_{\gamma\,i}$ is given by Eq. (32), and we recall that the multiphoton vertex position must lie along the line of flight of the K_L as reconstructed from an observed $K_S \to \pi^+\pi^-$ decay (Sec. 4).

7.3.2 Photon-multiplicity distributions; merging of split clusters

In Fig. 34, left, we show the distributions of the photon-multiplicity, $N_{n\,\gamma}$, for candidate $K_L \to \pi^0\pi^0\pi^0$ events, normalized to the total number of candidate events, N_{tot}. For $n = 7$ and $n = 8$, the agreement between data and Monte Carlo is not satisfying. This is because suprious single-photon vertices sometimes result from split clusters from a single photon, and this effect is underrepresented in the simulation. The phenomenon of cluster splitting, in fact, explains the presence of a significant fraction of the events with $n = 7$ or $n = 8$ that truly contain a $K_L \to \pi^0\pi^0\pi^0$ decay.

To reduce the effect of cluster splitting and improve the data-MC agreement on the photon-multiplicity distribution, we have developed a cluster-merging algorithm. For each event, we consider the two clusters with their centroids nearest to each other. We calculate the polar angle of the average position of these two clusters, θ_{avg}, and distinguish the cases in which this angle satisfies $0.6 < |cos\theta| < 0.8$, corresponding to the interface region between the calorimeter barrel and end-caps.[3] For cluster pairs not in the interface region, the two clusters are merged into a single cluster if their relative distance, $d_{12} \equiv |\mathbf{x}_1 - \mathbf{x}_2|$, is less than 20 cm, or if the smaller of the cluster energies, $E_{\min}$ is less than 25 MeV and $d_{12} < 55$ cm.

[3] Note that this is not the same as the definition of the overlap region used in the estimation of the single-photon efficiency.

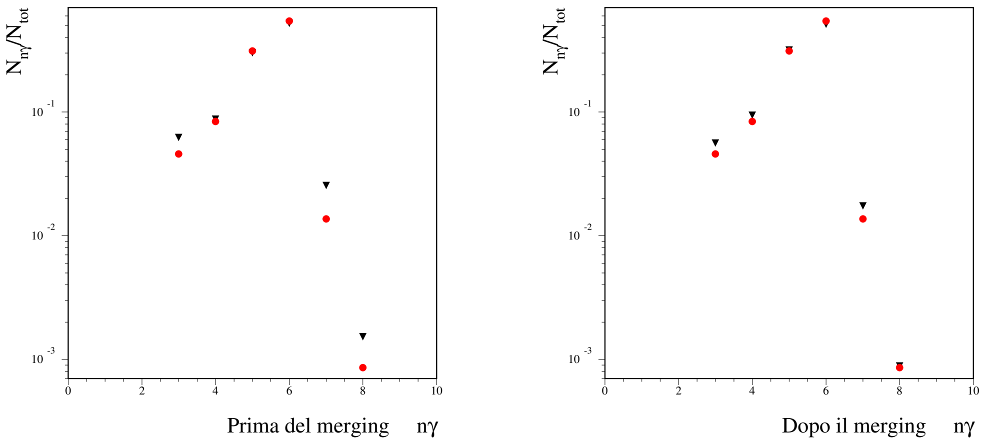

Fig. 34. Photon-multiplicity distributions before (left) and after (right) the application of the merging procedure. Black triangles represent data; red dots represent Monte Carlo. The distributions are normalized to the total number of selected events in each case.

Figure 35, left, shows the distribution of $E_{\min}$ vs. d_{12} for the nearest-centroid pairs in events with seven clusters not associated to tracks. The red line illustrates the merging criteria described above. If, on the other hand, the cluster pair is in the interface region, the clusters are merged if

$$E_{\min} \leq (60 - \frac{4}{15} d_{12}) \text{ MeV}.$$

Clusters are also merged using a second set of criteria. Again we consider the pair of clusters with their centroids nearest to each other, but we make no cut on the purely spatial separation of these two clusters. Defining

$$\beta_{12} \equiv \frac{d_{12}}{|t_1 - t_2|c},$$

with d_{12} as defined above, and t_1, t_2 the arrival times of the two clusters, we note that two clusters with $\beta_{12} < 1$ cannot arise from two distinct photons from the same K_L vertex. This is demonstrated by the following argument. Call L_1 and L_2 the distances of clusters 1 and 2 from their common decay vertex. Then the distance between clusters 1 and 2 is $(L_1^2 + L_2^2 - 2L_1L_2\cos\theta_{12})^{1/2}$, with θ_{12} the opening angle of the two clusters with respect to the K_L vertex. The two clusters will then have $\beta_{12} > 1$ if

$$L_1^2 + L_2^2 - 2L_1L_2\cos\theta_{12} < (L_1 - L_2)^2,$$

or equivalently, if $\cos\theta_{12} < 1$, which is true by construction. The condition $\beta_{12} < 1$

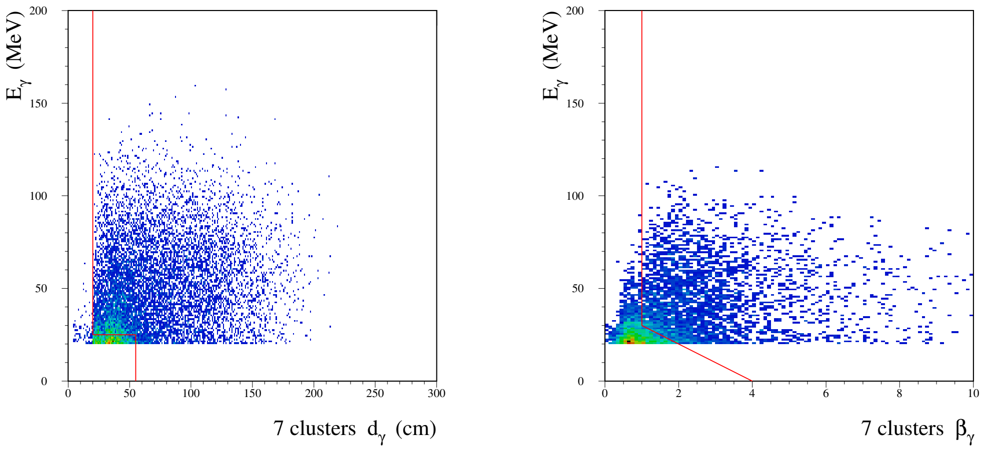

Fig. 35. Cluster-merging criteria for the pair of clusters with centrioids nearest to each other in data events with seven clusters not associated to tracks. Left: $E_{\min}$, the energy of the less energetic photon vs. d_{12}, the distance between the two centroids. Right: $E_{\min}$ vs. β_{12}, the separation velocity of the clusters. The red lines illustrate the merging criteria; cluster pairs falling below and to the left of the red lines are merged.

excludes (up to resolution effects) both cases in which the two clusters represent distinct photons from the same K_L vertex and cases in which one cluster is produced from a fragment of the other (i.e., backscatter). Cluster pairs with $\beta_{12} <$ 1 are then the result either of algorithmic or instrumental cluster splitting, or of interference from clusters in accidental coincidence with those from the K_L. The right panel of Fig. 35 shows the distribution of $E_{\min}$ vs. β_{12} for the nearest-centroid pairs in events with seven clusters not associated to tracks. The enhancement observed at low $E_{\min}$ and for $\beta_{12} < 1$ is in agreement with expectation for the effects of cluster splitting: the very low values of $E_{\min}$ in events with $\beta_{12} < 1$ suggest that the cluster of lower energy in such pairs is actually just a part of the other cluster. Based on these considerations, cluster pairs with $\beta_{12} < 1$ or $E_{\min} < (40 - 10\,\beta_{12})$ MeV are merged. These criteria are indicated by the red line in the right panel of Fig. 35.

When two clusters are merged, the position of the resulting cluster is given by the weighted average of the single centroid positions, while the time of the resulting cluster is given by the lesser of the two cluster times. The neutral-vertex position is then calculated accordingly.

7.3.3 Photon-counting systematics

The photon-multiplicity distributions after the merging procedure are shown in Fig. 34, right. There is a clear improvement in the agreement between data and Monte Carlo for events with $n = 7$ and $n = 8$. Moreover, the number of such events is reduced—the fraction of events with $n = 7$ in data drops from 2.5% to 1.7%, while the fraction of events with $n = 8$ drops from 0.15% to 0.08%.

The agreement between the photon-multiplicity distributions for data and Monte Carlo is also improved by the application of the single-photon efficiency corrections of Eqs. (37) and (38). The effect of the single-photon efficiency corrections on the multiplicity distribution can be illustrated with the following procedure. As expected from Fig. 33 and the form of Eqs. (37) and (38), for MC events, the uncorrected photon multiplicity is generally higher than it is for data. For each MC event, then, we sample n uniform deviates r_i, $i \in 1 \ldots n$ (one for each cluster in the event), and "delete" the i^{th} cluster if $r_i > f_i$, with f_i the data-MC ratio of single-photon efficiencies for a cluster of energy E_i, as calculated from Eqs. (37) or (38).

In Fig. 36, we compare the photon-multiplicity distributions after single photon efficiency corrections, for data, for an MC sample containing only signal ($K_L \to \pi^0\pi^0\pi^0$) events, and for an MC sample containing all K_L decays in their natural proportions. For the cases $n = 4$, 5, and 6, there is reasonable agreement between data and Monte Carlo. Moreover, there is reasonable agreement between the distributions for MC signal events and all MC events, which suggests that background is largely eliminated in the samples with $n = 4$, 5, and 6. There is a larger fraction of events with $n = 7$ in data than there is in either the MC signal sample or the sample of all MC events, while the fractions of events with $n = 7$ in the two MC samples are consistent. The excess in data for $n = 7$ cannot therefore be attributed to background; we suspect that this excess is due to the residual effects of cluster splitting. In any case, this discrepancy is of the order of 0.4% and can be considered negligible. The largest discrepancy between the distributions for data and MC signal is observed for the bin with $n = 3$. The fact that the agreement in the $n = 3$ bin is much better between the distributions for data and for the sample of all MC events demonstrates that the $n = 3$ bin includes a significant fraction of background events. This background is eliminated by the cuts described in the following section.

7.3.4 Background rejection for three-photon vertices

Background in the selection of events with $n = 3$ is eliminated by two types of cuts: one dealing with the photons themselves, and the other dealing with residual tracks in the events.

We first discuss the cuts made on the photons. These cuts are applied to events with $n = 3$ and $n = 4$.

We first reject events in which E_{max}, the energy of the photon with highest energy, is less than 50 MeV. We then select the pair of clusters with the smallest value

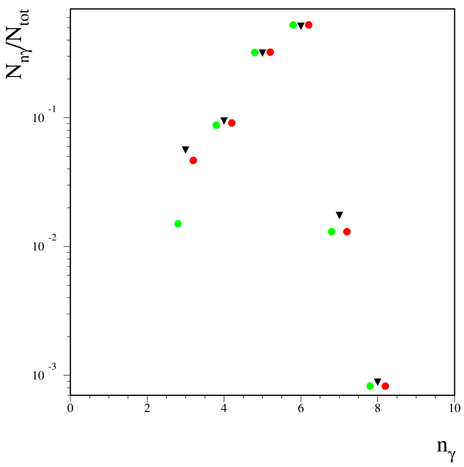

Fig. 36. Photon-multiplicity distributions after the application of the merging procedure and single-photon efficiency corrections, for data (black triangles), Monte Carlo signal events (green circles), and Monte Carlo events in which the K_L decays according to its natural branching ratios (red circles). All distributions are normalized.

of $d_{12} \equiv |\mathbf{x}_1 - \mathbf{x}_2|$, and reject events which satisfy

$$E_{\min} < [70 + 250(|\cos\theta| - 1)] \text{ MeV} \tag{42}$$

and

$$|\cos\theta| > 0.9, \tag{43}$$

where $E_{\min}$ is the energy of the cluster of lower energy, and θ is the polar angle of the point $(\mathbf{x}_1 + \mathbf{x}_2)/2$. The criteria of Eq. (42) were developed by consideration of the plots in Fig. 37. They are effective at reducing the contamination from $K_L \to \pi^+\pi^-\pi^0$ events in which an extra cluster is present due to machine background.

We next calculate the RMS pull of the single-photon vertex positions about the multiphoton vertex position,

$$\text{RMS} \equiv \left[\frac{1}{n-1}\sum_{i=1}^{n}\left(\frac{R_i - R_{K_L}}{\sigma_i}\right)^2\right]^{1/2}, \tag{44}$$

with R_i as in Eq. (41), σ_i the resolution on R_i from Eq. (32), and R_{K_L} the projected distance of the multiphoton vertex position. We reject events with $n = 3$ in which RMS > 1.2. The effect of this cut can be seen in Fig. 38, from which it is also seen that most multiphoton vertices in background events are reconstructed at transverse radii R_t so large that they are not within the fiducial volume.

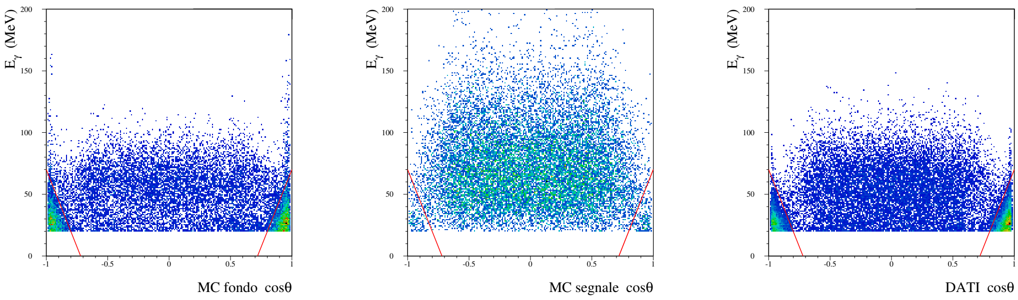

Fig. 37. Distributions of $E_{\min}$ vs. θ for the cases of MC background (including all K_L decays), MC signal, and data. The quantities $E_{\min}$ and θ are defined for the pair of clusters with the lowest value of $d_{12} \equiv |\mathbf{x}_1 - \mathbf{x}_2|$: $E_{\min}$ is the energy of the cluster of lower energy, and θ is the polar angle of the point $(\mathbf{x}_1 + \mathbf{x}_2)/2$. Events in the region below the red lines are eliminated by the criteria of Eq. (42).

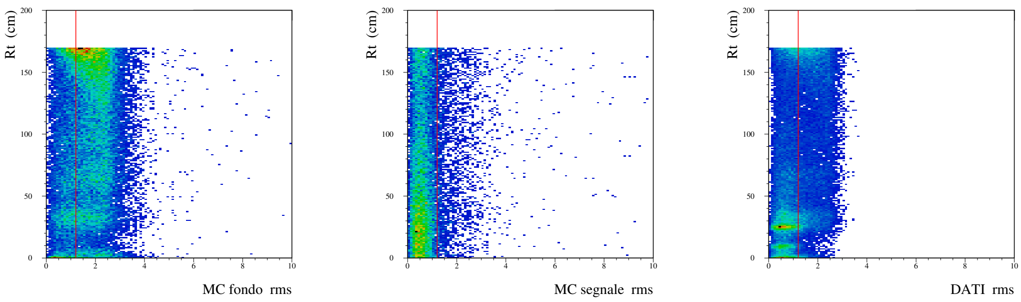

Fig. 38. Transverse radial position, R_t, for reconstructed multiphoton vertices a function of the RMS dispersion of the positions of the single-photon vertices about the multiphoton vertex (Eq. [44]), for events with $n = 3$ for (left to right) all MC events, MC signal events, and data. Events in the region to the right of the red line are eliminated by the cut on RMS described in the text.

The second type of cut used to reject background in the sample of events with $n = 3$ is based on tracking information. The analysis does not feature a general veto on the presence of tracks not associated with the $K_S \to \pi^+\pi^-$ decay, as unassociated track segments from the $K_S \to \pi^+\pi^-$ secondaries can occasionally be observed in $K_L \to \pi^0\pi^0\pi^0$ events, together with track segments from photon conversions, accidental activity, and the like. Tracks from decays of the K_L into charged secondaries, however, can be extrapolated to the line of flight of the K_L, as described in Sec. 6.1, and are found to have comparatively high values of p^*, the magnitude of the track momentum in the rest frame of the K_L, as discussed in Sec. 6.2. Figure 39 shows the distribution of $\Delta p^* \equiv p^* - 205$ MeV (the characteristic value of p^* for $K_L \to \pi^+\pi^-$ decays) vs. E_{tot}, the total energy of all clusters attached to the multiphoton vertex. On the basis of the comparison of the distributions for MC signal events and all MC events, we reject events in

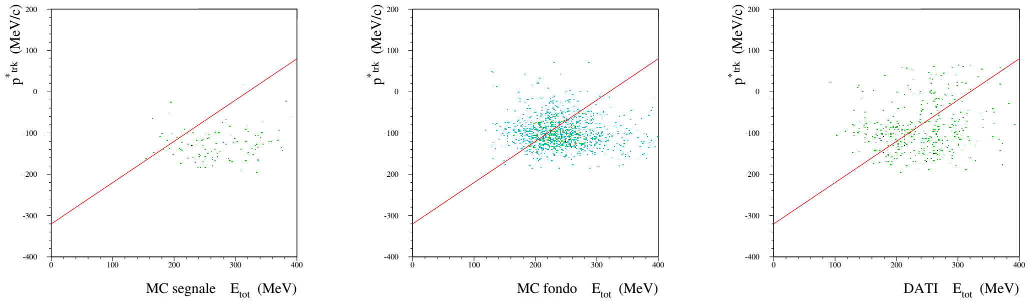

Fig. 39. Track momentum in the K_L center-of-mass frame, Δp^*, as a function of the total energy of all clusters attached to the multiphoton vertex, $E_{\rm tot}$, for events with $n = 3$ and tracks not associated to the $K_S \to \pi^+\pi^-$ decay in (left to right) the MC signal sample, the sample of all MC events, and data. Events above the red line are eliminated by the criterion of Eq. (45).

n	$N_{n\gamma}/N_{\rm tot}$, data	$\Delta(N_{n\gamma}/N_{\rm tot})$ data–MC
3	$(2.22 \pm 0.02)\%$	$(0.41 \pm 0.02) \times 10^{-2}$
4	$(9.05 \pm 0.05)\%$	$(0.18 \pm 0.06) \times 10^{-2}$
5	$(32.09 \pm 0.05)\%$	$(0.49 \pm 0.08) \times 10^{-2}$
6	$(54.71 \pm 0.08)\%$	$(-0.51 \pm 0.1) \times 10^{-2}$
7	$(1.82 \pm 0.02)\%$	$(0.36 \pm 0.02) \times 10^{-2}$

Table 5
Comparison of photon-multiplicity distributions for data and MC after all selection cuts and corrections. The values for the Monte Carlo refer to the combined sample for signal and background.

which $n = 3$ and

$$\Delta p^* > (E_{\rm tot} - 320)\ {\rm MeV}/c. \tag{45}$$

After making these selection cuts and corrections, we obtain the results listed in Table 5 for the photon-multiplicity distribution for vertices in the fiducial volume. The distributions for data and Monte Carlo are seen to agree at the 0.5% level, and after the cuts and corrections described above, we can obtain the values of $\varepsilon_{\rm FV}$ and $\varepsilon_{\rm rec}$ appearing in Eq. (1) directly from the Monte Carlo.

7.4 Reconstruction efficiency

The quantity $\varepsilon_{\rm rec}$ in Eq. (1) is evaluated as the ratio of the number of Monte Carlo $K_L \to \pi^0\pi^0\pi^0$ decays with a multiphoton vertex reconstructed within the fiducial volume to the total number of Monte Carlo $K_L \to \pi^0\pi^0\pi^0$ decays within

$\varepsilon_{\text{rec.}_{\pi^0\pi^0\pi^0}}$	purity	$\pi^0\pi^0$	$\pi^+\pi^-\pi^0$	NI
0.9930 ± 0.0003	0.9892 ± 0.0004	0.37 ± 0.02	0.34 ± 0.02	0.23 ± 0.02
0.9928 ± 0.0003	0.9887 ± 0.0004	0.40 ± 0.02	0.33 ± 0.02	0.22 ± 0.02
0.9906 ± 0.0004	0.9878 ± 0.0004	0.33 ± 0.02	0.38 ± 0.02	0.22 ± 0.02
0.9889 ± 0.0005	0.9896 ± 0.0005	0.43 ± 0.03	0.29 ± 0.03	0.20 ± 0.02
0.9904 ± 0.0003	0.9897 ± 0.0003	0.42 ± 0.02	0.31 ± 0.02	0.21 ± 0.02
0.9917 ± 0.0003	0.9892 ± 0.0004	0.38 ± 0.02	0.34 ± 0.02	0.22 ± 0.02
0.9911 ± 0.0003	0.9898 ± 0.0003	0.40 ± 0.02	0.33 ± 0.02	0.22 ± 0.02
0.9905 ± 0.0003	0.9896 ± 0.0003	0.40 ± 0.02	0.33 ± 0.02	0.23 ± 0.02
0.9916 ± 0.0003	0.9895 ± 0.0003	0.42 ± 0.02	0.30 ± 0.02	0.21 ± 0.02
0.9912 ± 0.0003	0.9901 ± 0.0003	0.41 ± 0.02	0.31 ± 0.02	0.22 ± 0.02
0.9909 ± 0.0003	0.9891 ± 0.0004	0.39 ± 0.02	0.34 ± 0.02	0.22 ± 0.02
0.9917 ± 0.0003	0.9892 ± 0.0004	0.41 ± 0.02	0.31 ± 0.02	0.23 ± 0.02
0.9903 ± 0.0003	0.9893 ± 0.0004	0.40 ± 0.02	0.31 ± 0.02	0.22 ± 0.02
0.9907 ± 0.0003	0.9897 ± 0.0003	0.41 ± 0.02	0.30 ± 0.02	0.23 ± 0.02

Table 6
Values of reconstruction efficiency and purity for $K_L \to \pi^0\pi^0\pi^0$ selection, by run period. The fraction of the background from each of the three main background processes, $K_L \to \pi^0\pi^0$, $K_L \to \pi^+\pi^-\pi^0$, and K_L undergoing nuclear interaction, are also given. The errors reflect only Monte Carlo statistics.

the fiducial volume:

$$\frac{N_{\text{rec}} \in \text{FV}}{N_{\text{sig}} \in \text{FV}} \tag{46}$$

where N_{sig} is the number of signal events in the Monte Carlo sample, and N_{rec} is the number of $K_L \to \pi^0\pi^0\pi^0$ decays reconstructed and selected by application of all of the criteria described above. The reconstruction efficiency ε_{rec} is given in Table 6 for each of the 14 data-taking periods. The average value is $\sim 99.0\%$.

7.5 Signal-event counting

For the evaluation of BR($K_L \to \pi^0\pi^0\pi^0$), we use the following procedure to count the number of decays into the signal channel (N_k in Eq. [1]).

The set of $K_L \to \pi^0\pi^0\pi^0$ candidate events contains a small amount of residual background even after all selection cuts. This can be seen from Fig. 40, which shows the distributions of the total energy of all clusters not asssociated to tracks for events with different photon multiplicities, for signal events and various categories of background, as obtained from the Monte Carlo. The purity of the $K_L \to \pi^0\pi^0\pi^0$ selection has been evaluated by Monte Carlo for each data-taking period (the validity of this approach is examined in Sec. 9.5). The values of purity and the fraction of the background from each of the three main background processes, $K_L \to \pi^0\pi^0$, $K_L \to \pi^+\pi^-\pi^0$, and K_L undergoing nuclear interaction, are given in Table 6. The average value of the sample purity is about 98.9%.

To obtain the final count of signal events in data, we multiply the number of selected $K_L \to \pi^0\pi^0\pi^0$ candidate events by the estimate of the sample purity, for each data-taking period. For each data-taking period of about 25 pb^{-1}, the number of selected events is about 5×10^4. The total number of selected events is roughly 7×10^5.

8 Measurement of K_L nuclear interactions in the detector

K_L nuclear interactions affect the evaluation of the fiducial-volume efficiency and of background levels. The fiducial-volume efficiency depends on the probability for the K_L to interact before entering the FV, as well as on the probability for interaction within the FV:

$$\varepsilon_{FV} = \frac{N_{\rm all}^{\rm FV} - N_{\rm int}^{\rm FV}}{N_{K_S}} \tag{47}$$

where N_{K_S} is the number of K_L's tagged by observation of a $K_S \to \pi^+\pi^-$ decay, $N_{\rm all}^{\rm FV}$ is the number of K_L's that decay or interact within the FV, and $N_{\rm int}^{\rm FV}$ is the number of K_L's that undergo nuclear interactions in the FV. $N_{\rm all}^{\rm FV}$ depends on the geometrical acceptance and on the number of K_L's lost due to nuclear interactions occurring before the K_L crosses the inner border of the FV, $N_{\rm loss}$. The values of $N_{\rm loss}$ and $N_{\rm int}^{\rm FV}$ are evaluated using the Monte Carlo, with corrections from data. We obtain $N_{\rm int}^{\rm FV}/N_{\rm all}^{\rm FV} = 0.0033 \pm 0.0013$ and $N_{\rm loss}/N_{K_S} = 0.0016 \pm 0.0008$.

Nuclear interaction processes in the FV are also a source of background and affect signal extraction.

The principal nuclear interaction processes, $K_L \to K_S$ regeneration, $\bar{K}^0 N \to \Sigma\pi$, and $\bar{K}^0 N \to \Lambda\pi$, are simulated in the Monte Carlo. The rates for all three types of interaction process are also determined using data, and the simulation is corrected accordingly. The predicted rate of K_L beam loss is then checked by analyzing the distribution of the reconstructed K_L-decay vertex position, both for K_L decays to charged and neutral particles.

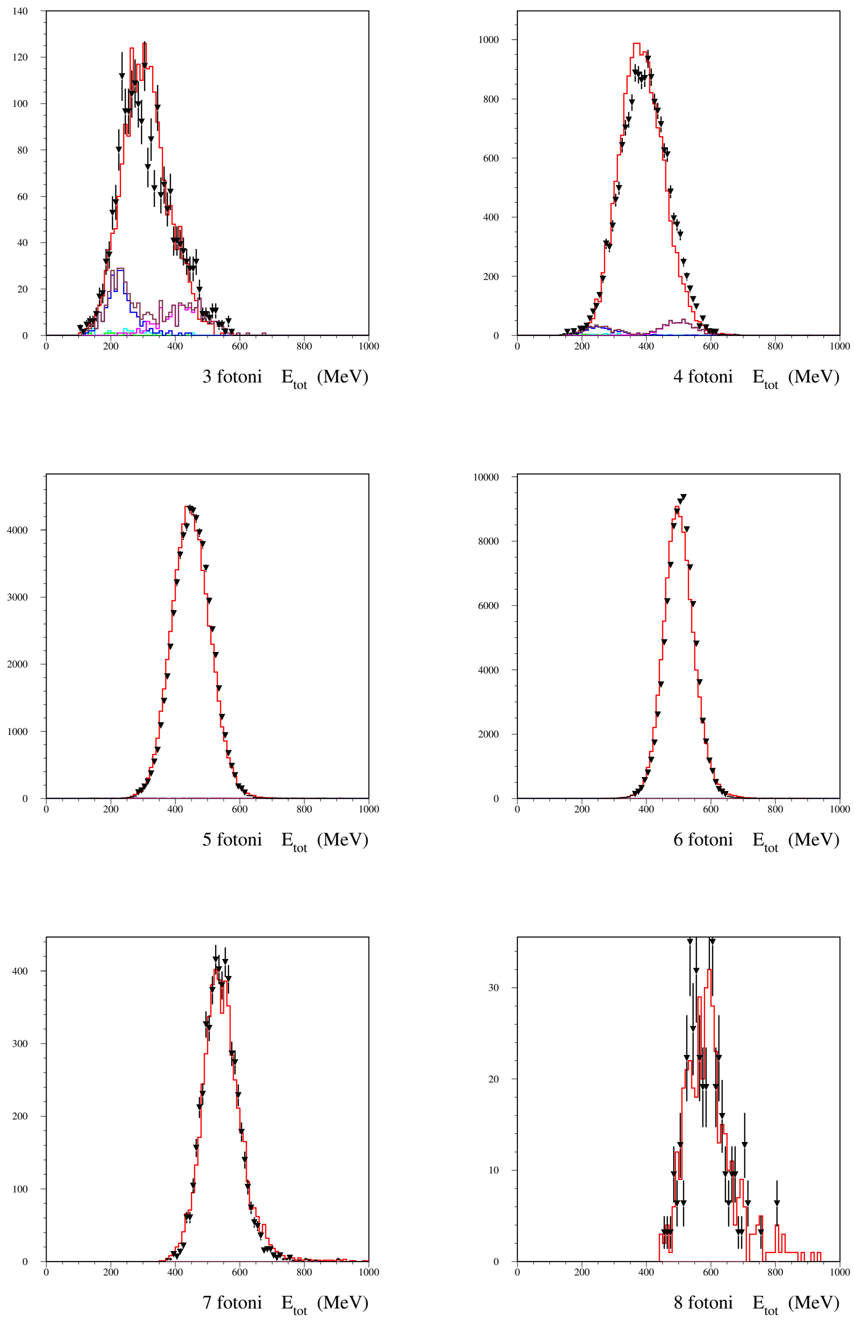

Fig. 40. Distributions of the total energy of clusters not asssociated to tracks, for events with different photon multiplicities. The multiplicity distributions for data are shown in the black triangles; those for Monte Carlo samples are shown as the colored histograms: red, signal ($K_L \to \pi^0\pi^0\pi^0$); violet, K_{e3}; green, $K_{\mu3}$; blue, $K_L \to \pi^+\pi^-\pi^0$; light blue, $K_L \to \pi^0\pi^0$; sum of all MC background events, black.

For the purposes of the studies discussed below, we normalize the Monte Carlo results using the measurement of the integrated luminosity for the data set.

8.1 $K_L \to K_S$ regeneration

The probability for $K_L \to K_S$ regeneration has been measured using the decay $K_S \to \pi^+\pi^-$. These decays are selected on the basis of the two-track invariant mass, M, evaluated by assigning both tracks the pion mass.

The coherent regeneration intensity is expected to be about 1000 times smaller than the incoherent regeneration intensity. Regenerated K_S's can therefore be distinguished from $K_L \to \pi^+\pi^-$ decays on the basis of the angle between the K_L direction and the momentum $\mathbf{p}_{\pi^+} + \mathbf{p}_{\pi^-}$. Another quantity that is useful in distinguishing the decays of regenerated K_S's is

$$q_{\text{miss}} \equiv \sqrt{E^2_{\text{miss}} + \mathbf{p}^2_{\text{miss}}},$$

where $\mathbf{p}_{\text{miss}}$ and E_{miss} are evaluated from the K_L (tagging) momentum and the momenta of the two tracks, and the charged pion mass is assumed for each track in the calculation of E_{miss}.

We have performed the measurement of the regeneration intensity in three different fiducial regions: $30 < r_{xy} < 160$ cm, containing the FV; $20 < r_{xy} < 30$ cm, around the inner wall of the drift chamber; and $5 < r < 15$ cm, around the beam pipe.

Figure 41 shows the scatter plot of $M - m_{K^0}$ vs. q_{miss} for vertices in the FV, as obtained with the Monte Carlo. The contributions from $\pi^\pm e^\mp\nu$, $\pi^\pm\mu^\mp\nu$, $K_L \to \pi^+\pi^-$, and $K_L \to K_S \to \pi^+\pi^-$ transitions are indicated separately. It can be seen that the distribution for regeneration events peaks at values of $M - m_{K^0}$ around zero, while these events have characteristically large values of q_{miss}.

To calibrate the level of regeneration events in the Monte Carlo, we compare the distributions of $M - m_{K^0}$ for Monte Carlo to those for data in each of the three regions listed above. To enhance the contribution from regeneration events, we require $q_{\text{miss}} > 60$ MeV for vertices in the FV, and $q_{\text{miss}} > 10$ MeV in the other regions. These comparisons are shown in Fig. 42. We find that the ratio of the regeneration probability in data to that in the Monte Carlo is about 0.3 inside the fiducial volume, about 0.67 at the inner DC wall, and about 1.5 at the beam-pipe wall.

We also find a disagreement between Monte Carlo and data in the scattering angle distribution for the regions about the inner DC and beam-pipe walls. The

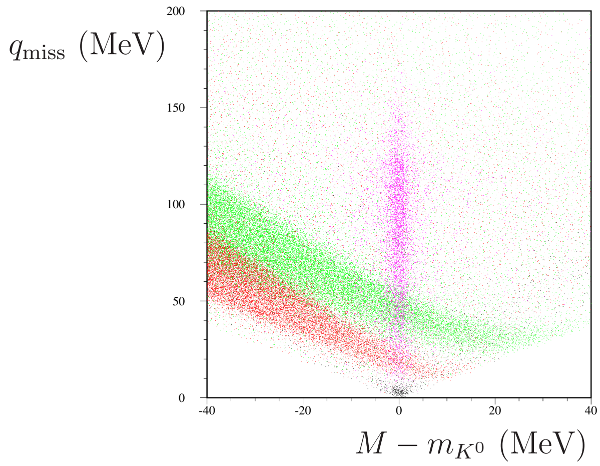

Fig. 41. Scatter plot of $M - m_{K^0}$ vs. $q_{\rm miss}$ for track vertices in the FV, from Monte Carlo. Colors represent $\pi^{\pm}e^{\mp}\nu$ (green), $\pi^{\pm}\mu^{\mp}\nu$ (red), $\pi^{+}\pi^{-}\pi^{0}$ (blue), $\pi^{+}\pi^{-}$ (black), and regeneration (pink) events.

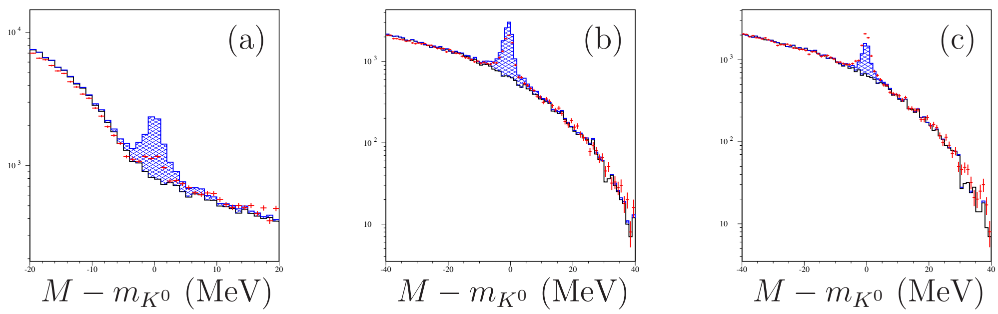

Fig. 42. Distribution of $M - m_{K^0}$ for data (red points) and Monte Carlo without (black lines) and with (blue histogram) regeneration, for samples of vertices enriched in regeneration candidates (a) in the fiducial volume; (b) near the inner DC wall; (c) near the beam-pipe wall.

distribution of the scattering angle,

$$\cos\theta_{\rm reg} \equiv \frac{\mathbf{p}_{K_L}\cdot(\mathbf{p}_{\pi^+}+\mathbf{p}_{\pi^-})}{|\mathbf{p}_{K_L}|\,|\mathbf{p}_{\pi^+}+\mathbf{p}_{\pi^-}|}$$

is shown in Fig. 43 for each of the three regions. These distributions have been obtained for vertices with $|M - m_{K^0}| < 5$ MeV (and no requirement on $q_{\rm miss}$). The disagreement is not due to the incorrect simulation of the resolution tails in the scattering angle distribution, as can be seen comparing the scattering-angle distributions for data and Monte Carlo for events in the sidebands of the $M - m_{K^0}$ distribution. The disagreement has been traced to an incorrect treatment of the inelastic kaon interaction processes in GHEISHA. Figure 44 shows the com-

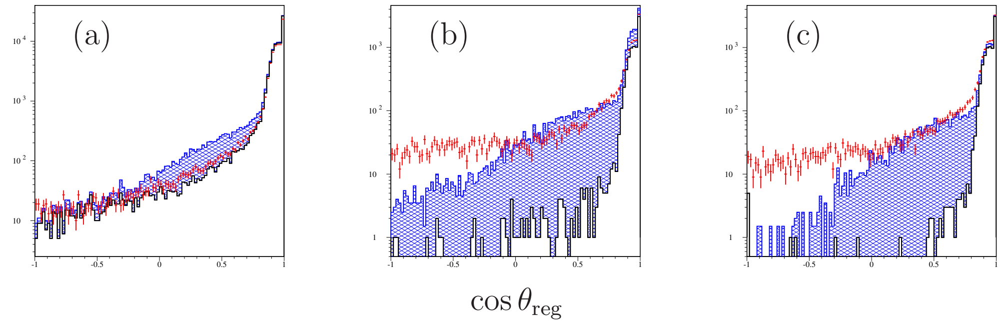

Fig. 43. Distribution of the scattering angle, $\cos\theta_{\rm reg}$, for data (red points) and Monte Carlo without (black lines) and with (blue histogram) regeneration, for vertices with $|M - m_{K^0}| < 5$ MeV (a) in the fiducial volume; (b) near the inner DC wall; (c) near the beam-pipe wall.

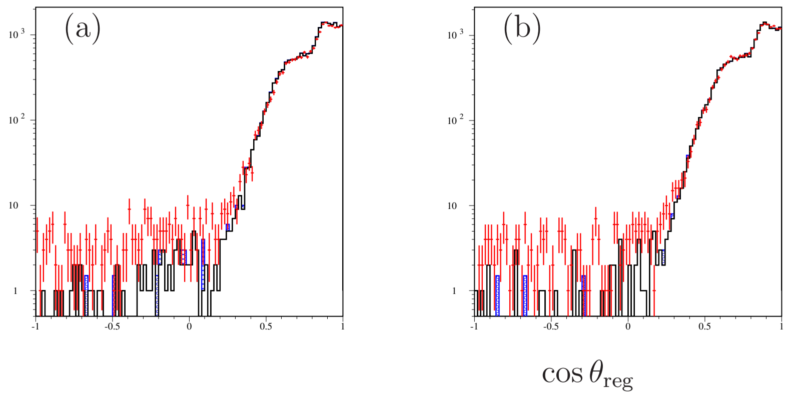

Fig. 44. Distribution of the scattering angle, $\cos\theta_{\rm reg}$, for data (red points) and Monte Carlo without (black lines) and with (blue histogram) regeneration, for vertices with -40 MeV $< |M - m_{K^0}| < -10$ MeV (a) near the inner DC wall; (b) near the beam-pipe wall.

parison of the $\cos\theta_{\rm reg}$ distributions for data and Monte Carlo for vertices with -40 MeV $> (M - m_{K^0}) > -10$ MeV. The disagreement in the scattering-angle distribution introduces a dependence of the data-Monte Carlo ratio of regeneration probabilities found from the analysis of the $M - m_{K^0}$ distributions on the value used for the cut on $q_{\rm miss}$. Changing the cut value results in a variation of about 30% in the data-Monte Carla ratio of regeneration probabilities. This variation is included in the systematic errors on the estimates of $\varepsilon_{\rm FV}$ (Sec. 9.2) and background levels (Secs. 9.3 and 9.5) for the purposes of the branching ratio measurements.

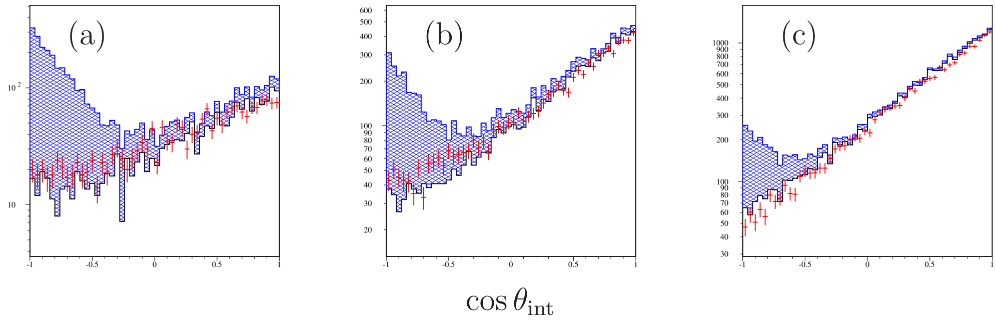

Fig. 45. Distribution of $\cos\theta_{\rm int}$, for data (red points) and Monte Carlo without (black lines) and with (blue histogram) $\Lambda\pi^0$ and $\Sigma\pi^0$ production, for events with multiphoton vertices in the region of the inner wall of the drift chamber and (a) $n = 3$, (b) $n = 4$, (c) $n = 5$.

8.2 K_L nuclear interactions

The simulation of $\Lambda\pi$, $\Sigma\pi$ production due to nuclear interactions of K_L's with detector materials is also checked using data. An accurate measurement of the rates requires dedicated selection criteria for the different final states, with background rejection factors of about 1000. However, the overall probability for such interactions is only about 5% in the KLOE detector, and for our purposes, it is therefore sufficient to know this probability with a relative accuracy of about 20%. We therefore simply use the selection of neutral events to study $\Lambda\pi^0$ and $\Sigma^0\pi^0$ production levels.

A useful variable is the angle between the momentum of the K_L and that of the vector sum of the momenta of the photons attached to the multiphoton vertex:

$$\cos\theta_{\rm int} \equiv \frac{\mathbf{p}_{K_L}\cdot\left(\sum_{i=1}^{n}\mathbf{p}_i\right)}{|\mathbf{p}_{K_L}|\,|\left(\sum_{i=1}^{n}\mathbf{p}_i\right)|},$$

where the $\mathbf{p}_i$ are the photon momenta as reconstructed from the energies and positions of the corresponding clusters. The distributions of $\cos\theta_{\rm int}$ for events with multiphoton vertices in the region of the inner wall of the drift chamber and $n = 3$, 4, and 5 are shown in Fig. 45, for data and Monte Carlo. Nuclear interactions between the K_L and the material of the inner DC wall are significantly overrepresented in the Monte Carlo; we obtain a data-Monte Carlo of about 0.15 with a precision of about 30%.

Finally, we compare the distributions of the transverse radius r_{xy} for reconstructed vertices in the vicinity of the beam pipe and inner DC walls. The distributions are shown in Fig. 46 both for photon and track vertices. The agreement between data and Monte Carlo in the regenerator regions is much better than suggested by the 30% uncertainty quoted above, except for track vertices in the vicinity of

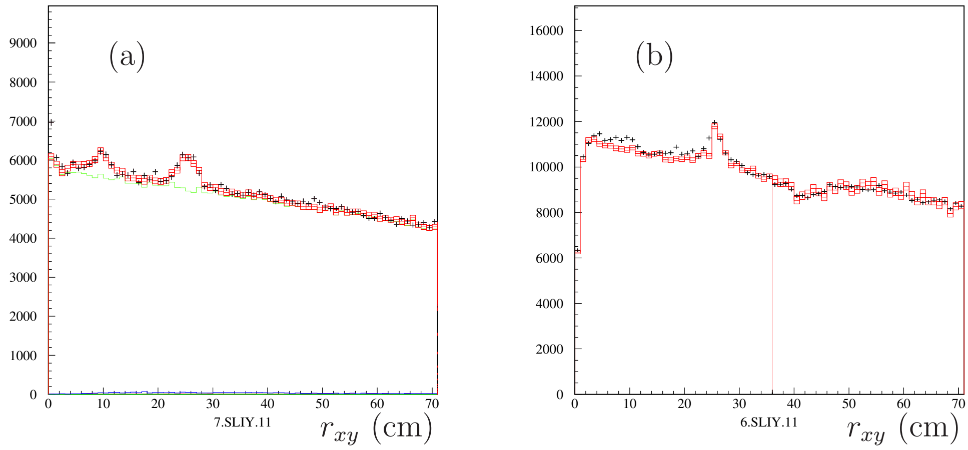

Fig. 46. Distributions of transverse radius r_{xy} for (a) reconstructed photon vertices and (b) reconstructed track vertices, for data (black) and Monte Carlo (red).

	$\pi^{\pm}e^{\mp}\nu$	$\pi^{\pm}\mu^{\mp}\nu$	$\pi^{+}\pi^{-}\pi^{0}$	$\pi^{0}\pi^{0}\pi^{0}$
Selection	0.0011	0.0007	0.0004	0.0020
Kinematic Shape	0.0006	0.0009	0.0010	-
Tag bias	0.0013	0.0008	0.0007	0.0005
K_L lifetime	0.0023	0.0017	0.0007	0.0012

Table 7
Summary of systematic uncertainties on the absolute branching ratio measurements.

the beam pipe, where a disagreement of $\sim 50\%$ is present. The uncertainty on the beam-loss fraction for the purposes of evaluating the fiducial-volume efficiency is within the value of 30% quoted.

9 Systematic uncertainties

The systematic errors due to the finite statistics in the evaluation of corrections, data-Monte Carlo inconsistencies, instabilities in the signal extraction procedure, and limited knowledge of the K_L lifetime and nuclear interaction probability are summarized in Table 7 for each K_L decay mode.

9.1 Tag bias

The systematic error on the evaluation of the tag bias arises from the uncertainties on the individual corrections and from the study of the stability of the results

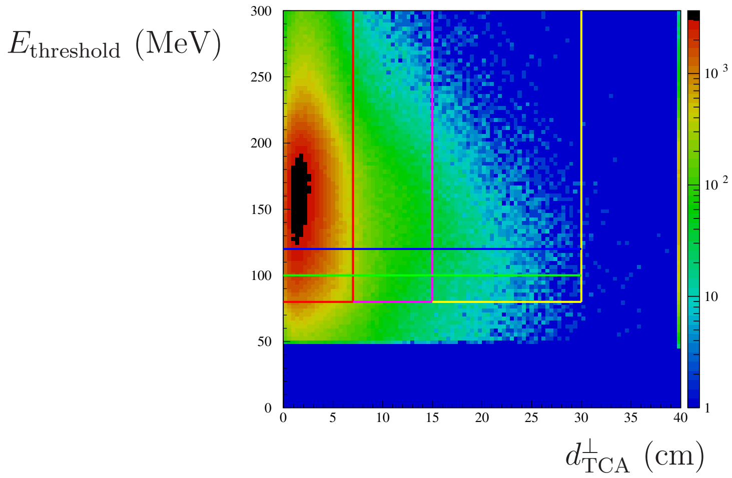

Fig. 47. Scatter plot of $E_{\rm threshold}$ vs. $d_{\rm TCA}^{\perp}$, for data. The different cuts applied to study the stability of the tag bias are indicated by the colored lines.

obtained with different tagging criteria. We have also studied the dependence of the tag bias on the K_L lifetime and nuclear interaction cross section.

As disussed in Sec. 4, the main source of the tag bias is the dependence of the trigger efficiency on the K_L behavior. The values of the cuts used to define the tag, $E_{\rm threshold} > 100$ MeV, $d_{\rm TCA}^{\perp} < 15$ cm, and $|\Delta P_{\rm track}| < 60$ MeV (see Sec. 4.3), have been varied over a wide range. We have also determined the tag bias with the requirement that the pions from $K_S \to \pi^+\pi^-$ be associated to clusters in "clean" trigger sectors. In total, we have studied the stablity of the result for 15 different tag configurations.

Figure 47 shows the scatter plot of $E_{\rm threshold}$ vs. $d_{\rm TCA}^{\perp}$. For the study of the stability of the tag bias with respect to variations in the tagging criteria, the cut on $E_{\rm threshold}$ was placed at 80, 100, and 120 MeV, while the cut on $d_{\rm TCA}^{\perp}$ was placed at 7, 15, and 30 cm. These variations are represented by the grid shown in Fig. 47. When the cuts are varied in this way, the tagging efficiency changes by $\sim \pm 50\%$ with respect to the tagging efficiency obtained with the default cuts. Corresponding fractional changes on the K_L branching ratios of 0.1% to 0.25% are observed depending on the channel.

The cut on $|\Delta P_{\rm track}|$ has been alternately tightened to 30 MeV and completely removed; the corresponding variation in the tagging efficiency is about $\pm 40\%$. Corresponding fractional changes on the K_L branching ratios of 0.1% to 0.3% are observed depending on the channel. The complete information is contained in the error matrix:

$$
\begin{array}{cc}
 & \begin{array}{cccc} K_{e3} & K_{\mu 3} & \pi^+\pi^-\pi^0 & 3\pi^0 \end{array} \\
\sigma^2_{\text{Tag}} = & \begin{pmatrix} 17.54 & -8.92 & 7.65 & 3.40 \\ -8.92 & 6.13 & -3.60 & -0.91 \\ 7.65 & -3.60 & 5.29 & 2.63 \\ 3.40 & -0.91 & 2.63 & 2.84 \end{pmatrix} \times 10^{-7}
\end{array}
$$

We have also studied the impact of the trigger efficiency on the tag bias. To better ensure the sufficiency of the K_S decay topology in generating the trigger, we test a tag configuration in which only the pions from the $K_S \to \pi^+\pi^-$ decay are present in the corresponding trigger sectors. In this configuration, we require that the trigger sectors occupied by the clusters from the pion tracks contain no additional clusters with energies above a given threshold (20 or 50 MeV) and times of arrival earlier than 30 ns. This latter criterion allows exception for clusters from the K_L interaction in the calorimeter, which are not simulated with the required accuracy. With either threshold, the change in the tag bias with respect to that obtained in the default configuration is smaller than 0.05%.

The uncertainties due to the correction for tracking interference (Sec. 4.4) have both a statistical and a systematic component. The correction is run-period dependent; its statistical error has been obtained from the average over all periods. The corresponding errors on the branching ratios are largely correlated among channels, as can be seen from the error matrix:

$$
\sigma^2_{\text{track int stat}} = \begin{pmatrix} 1.12 & 0.76 & 0.36 & -0.01 \\ 0.76 & 0.51 & 0.24 & -0.01 \\ 0.36 & 0.24 & 0.11 & 0.00 \\ -0.01 & -0.01 & 0.00 & 0.80 \end{pmatrix} \times 10^{-7}
$$

As described in Sec. 4.4, the tracking interference correction is obtained from fits to the data-Monte Carlo ratio of the distributions in r_{xy} of the K_L track vertices. The effect of using different fit functions has also been studied. The corresponding change in the tracking-interference correction is fully correlated among channels and amounts to 0.15%.

In addition, we compare the K_L proper decay time distributions (after all corrections) for events in which the K_L decays into charged particles and into $3\pi^0$, since the maximal variation of the tag bias with decay channel is between these two cases. These are shown in Fig. 48. The distribution for decays into $3\pi^0$ has been

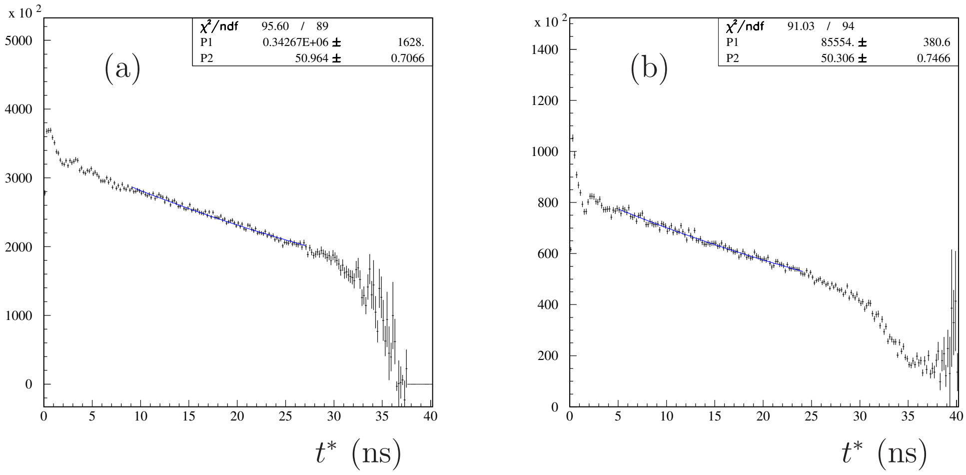

Fig. 48. Proper time distributions for K_L decays to (a) charged particles and (b) $3\pi^0$. Fits to an exponential fuction are also shown.

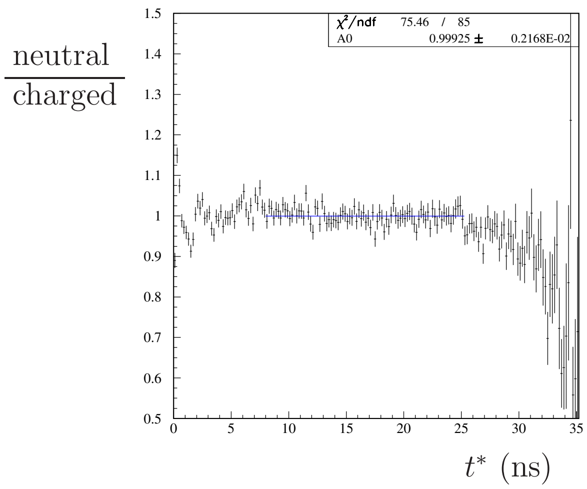

Fig. 49. Ratio of proper time distributions for K_L decays to $3\pi^0$ and to charged secondaries.

fit in the region 5–24 ns as in the KLOE analysis of the K_L lifetime [14]. The lower boundary of the fit region has been increased slightly for the fit to the distribution for K_L decays into charged particles, because of the presence of tracking-interference corrections for $r_{xy} < 25$ cm. The values of the lifetime obtained from the distributions for K_L decays into charged particles ($\tau(K_L) = 51.0 \pm 0.7$ ns) and into $3\pi^0$ ($\tau(K_L) = 50.3 \pm 0.8$ ns) are in agreement. Figure 49 shows the ratio of the proper time distributions for K_L decays into $3\pi^0$ and into charged secondaries. The distributions are normalized using the measured values of the branching ratios.

9.2 Fiducial-volume efficiency

The main sources of uncertainty on the evaluation of the fiducial-volume efficiency are the limited knowledge of the nuclear interaction cross section and the accuracy of the K_L lifetime value. The uncertainty on the fiducial-volume efficiency obviously affects the branching ratio measurements for all channels in the same way. The contribution to the uncertainty on the branching ratio measurements arising from the uncertainty on the K_L lifetime cancels out if the sum of the branching ratios is constrained to unity.

We use the Monte Carlo to obtain raw estimates of the K_L beam loss to interactions with material crossed before entering and within the fiducial volume. These raw estimates of K_L beam-loss effects are then corrected using data, as described in Sec. 8. The corrections are determined with an uncertainty of about 30%, both for regeneration and for Λ/Σ production. Propagating the uncertainty on these corrections to the uncertainty on the fiducial-volume efficiency results in a 0.15% relative contribution to the uncertainty on the latter.

The geometrical efficiency of the fiducial volume depends on the value of the K_L lifetime. A variation in the lifetime of 1% translates into a change of 0.8% in the acceptance. The 0.8% current accuracy on the K_L lifetime [1] leads to a 0.64% uncertainty on the absolute branching ratio measurements.

9.3 Tracking efficiency

The uncertainty on the tracking efficiency correction is dominated by sample statistics and by the variation of the results observed using different criteria to identify good tracks from K_L decays.

The correction is run-period dependent; its statistical error has been obtained from the average over all periods. A large correlation is observed between the corrections for the $\pi^{\pm}e^{\mp}\nu$ and $\pi^{\pm}\mu^{\mp}\nu$ decay modes, due to the overlap of the momentum distributions for the secondaries in either case (recall that the correction is applied as a function of track momentum). The corresponding error matrix is:

$$\sigma^2_{\text{track eff stat}} = \begin{pmatrix} 2.41 & 1.69 & 1.03 & 0. \\ 1.69 & 1.26 & 0.77 & 0. \\ 1.03 & 0.77 & 0.80 & 0. \\ 0. & 0. & 0. & 0. \end{pmatrix} \times 10^{-7}$$

The effect of differences in the resolution with which the variables d_c and l_c

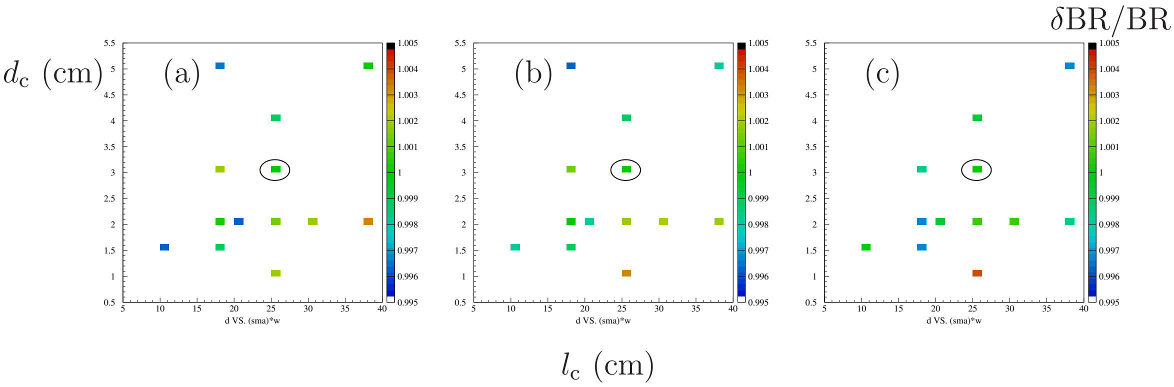

Fig. 50. Fractional change in the measured branching ratios for (left to right) the $\pi^{\pm}e^{\mp}\nu$, $\pi^{\pm}\mu^{\mp}\nu$, and $\pi^{+}\pi^{-}\pi^{0}$ modes, as a function of the cuts on d_{c} (the intercept of the red line in Fig. 8[a]) and l_{c} (the upper red line in Fig. 8[b]). The circled points represent the cut values used in the analysis.

are reconstructed (Sec. 6.1) in data and in Monte Carlo has studied by varying the values of the cuts made on these variables when associating tracks to K_L vertices. A total of 14 configurations have been studied. In particular, the cut on d_{c} is illustrated in Fig. 8(a); the intercept of the red line in the figure was varied from 1 cm to 5 cm. The cut on l_{c} illustrated by the upper red line in Fig. 8(b) was varied from 10 cm to 40 cm, and other variations were made to the contour of the region accepted below $r_{xy} = 40$ cm. These variations resulted in a variation of the tracking efficiency of about ±20%. For each configuration, the complete tracking-efficiency correction was obtained and used to evaluate the branching ratios. Figure 50 summarizes the fractional change in the results as a function of the cut values. The resulting error matrix is

$$\sigma^2_{\text{track corr syst}} = \begin{pmatrix} 12.32 & 7.62 & 2.50 & 0. \\ 7.62 & 5.54 & 2.19 & 0. \\ 2.50 & 2.19 & 1.41 & 0. \\ 0. & 0. & 0. & 0. \end{pmatrix} \times 10^{-7}.$$

9.4 Signal extraction for decays to charged particles

To assess the uncertainty on the measurements of the K_{e3} and $K_{\mu3}$ branching ratios arising from limited knowledge of the momentum resolution and of the accuracy of simulation of final-state radiation, we have performed the signal extraction with and without the shape corrections dicussed in Sec. 6.5. The resulting error matrix is

$$\sigma^2_{\text{shape}} = \begin{pmatrix} 3.62 & 1.54 & 3.84 & 0. \\ 1.54 & 7.46 & 6.68 & 0. \\ 3.84 & 6.68 & 9.28 & 0. \\ 0. & 0. & 0. & 0. \end{pmatrix} \times 10^{-7}.$$

The systematic error on the remaining background due to K_L nuclear interactions is evaluated from the variation in the results for the branching ratios corresponding to a change in the nuclear interaction rate by one standard deviation with respect to the values given in Sec. 8. The $|\mathbf{p}_{\text{miss}}| - E_{\text{miss}}$ distributions for K_{e3} and $\pi^+\pi^-\pi^0$ decays significantly overlap the $|\mathbf{p}_{\text{miss}}| - E_{\text{miss}}$ distributions from regeneration and Λ/Σ production. The 30% accuracy on the measurement of regeneration and Λ/Σ production rates translates into uncertainties of 0.02% and 0.06% on the K_{e3} and $\pi^+\pi^-\pi^0$ branching ratios, respectively.

9.5 $K_L \to \pi^0\pi^0\pi^0$ counting

The uncertainty on the determination of the number of $K_L \to \pi^0\pi^0\pi^0$ decays has been evaluated by checking the stability of the measured branching ratio with respect to modifications in the selection criteria. The effects of the photon-efficiency corrections and the cluster-splitting recovery algorithm are below 0.1%. The largest deviation occurs if the minimum number of photons required at the K_L vertex is rasied from three to five. This cut reduces the background contamination to about 0.1% while maintaining a signal efficiency of 88%. Requiring $n \geq 5$ changes the result by 1%. This variation has been conservatively taken as the systematic error on the $K_L \to \pi^0\pi^0\pi^0$ branching ratio measurement. The uncertainty on the level of background from nuclear interactions is responsible for 0.08%. An additional study has been performed by checking the result stability when the photon energy threshold is hardened. For $E^{\gamma}_{\text{threshold}} = 50$ MeV, the efficiency is about 95% and the background is reduced to 0.5%. The $K_L \to \pi^0\pi^0\pi^0$ branching ratio decreases by 0.3%.

10 Results and $|V_{us}|$ determination

10.1 Absolute K_L branching ratios

A total of about 13×10^6 tagged K_L events are used for the signal counting in the measurement of the branching ratios.

n. of tagged K_L	$\pi^\pm e^\mp \nu$	$\pi^\pm \mu^\mp \nu$	$\pi^+\pi^-\pi^0$	cl %	$\pi^0\pi^0\pi^0$
798300	43693.3 ± 287.2	28310.1 ± 237.0	9678.6 ± 135.4	25	41635
921690	49739.7 ± 306.4	32692.0 ± 255.3	11082.6 ± 144.6	42	48297
913890	50959.5 ± 308.1	33174.2 ± 255.3	11082.1 ± 143.1	21	47784
474230	26441.1 ± 221.3	17103.5 ± 182.8	6067.5 ± 106.4	17	24879
1004520	56989.5 ± 326.3	36757.4 ± 268.5	12238.5 ± 150.8	21	52999
1017760	57803.2 ± 328.5	37730.3 ± 272.9	12754.6 ± 154.3	19	53662
1017460	57582.1 ± 326.8	37654.3 ± 271.3	12933.7 ± 155.5	10	53678
1010000	57371.6 ± 326.1	37453.6 ± 270.4	12948.8 ± 154.9	20	53185
1008300	57171.4 ± 324.3	37676.1 ± 270.6	12613.5 ± 151.8	9	53914
993270	55661.3 ± 319.3	36458.7 ± 265.4	12663.9 ± 151.8	5	53156
998100	55785.8 ± 320.2	36288.3 ± 264.3	12060.7 ± 148.0	13	52022
985610	55574.5 ± 318.6	35619.0 ± 260.9	12218.7 ± 148.5	10	52241
954590	53523.3 ± 311.8	34760.8 ± 257.8	11940.8 ± 147.0	9	50490
1002670	56214.9 ± 321.5	37296.4 ± 269.4	12623.5 ± 152.9	55	52685

Table 8
Numbers of tagged K_L events and selected events by channel, for all run periods. Errors are statistical only. For decays into charged particles, the errors are evaluated from fits and include a contribution from finite Monte Carlo statistics.

The numbers of tagged K_L events and selected events for each channel are listed by run period in Table 8. The branching ratios are obtained using the data in Table 8, the efficiencies in Tables 3 and 6, and the tag bias values in Table 2, and are plotted in Figure 51 as a function of run period. The value of the K_L lifetime $\tau_{K_L} = 51.54 \pm 0.44$ ns [15] has been used to evaluate the fiducial-volume efficiency. The error bars in Figure 51 represent only the uncorrelated statical errors [4] for each run period, and illustrate the stability of the measurements.

The final values for the absolute branching ratios are obtained from the averages over all run periods:

$$\begin{aligned}
&\mathrm{BR}(K_L \to \pi^\pm e^\mp \nu) = \\
&\qquad 0.4049 \pm 0.0006_{\mathrm{stat}} \pm 0.0008_{\mathrm{syst-stat}} \pm 0.0018_{\mathrm{syst}} \pm 0.0025_{\mathrm{corr-syst}}, \\
&\mathrm{BR}(K_L \to \pi^\pm \mu^\mp \nu) = \\
&\qquad 0.2726 \pm 0.0006_{\mathrm{stat}} \pm 0.0006_{\mathrm{syst-stat}} \pm 0.0014_{\mathrm{syst}} \pm 0.0017_{\mathrm{corr-syst}}, \\
&\mathrm{BR}(K_L \to \pi^0\pi^0\pi^0) = \\
&\qquad 0.2018 \pm 0.0003_{\mathrm{stat}} \pm 0.0004_{\mathrm{syst-stat}} \pm 0.0023_{\mathrm{syst}} \pm 0.0012_{\mathrm{corr-syst}}, \\
&\mathrm{BR}(K_L \to \pi^+\pi^-\pi^0) = \\
&\qquad 0.1276 \pm 0.0004_{\mathrm{stat}} \pm 0.0004_{\mathrm{syst-stat}} \pm 0.0014_{\mathrm{syst}} \pm 0.0008_{\mathrm{corr-syst}}.
\end{aligned}$$

For the decays into charged particles, the statistical errors quoted are evaluated from fits and include a contribution from finite Monte Carlo statistics in addi-

[4] These include the statistcal uncertainties due to the limited knowledge of the corrections and the effects of finite Monte Carlo statistics.

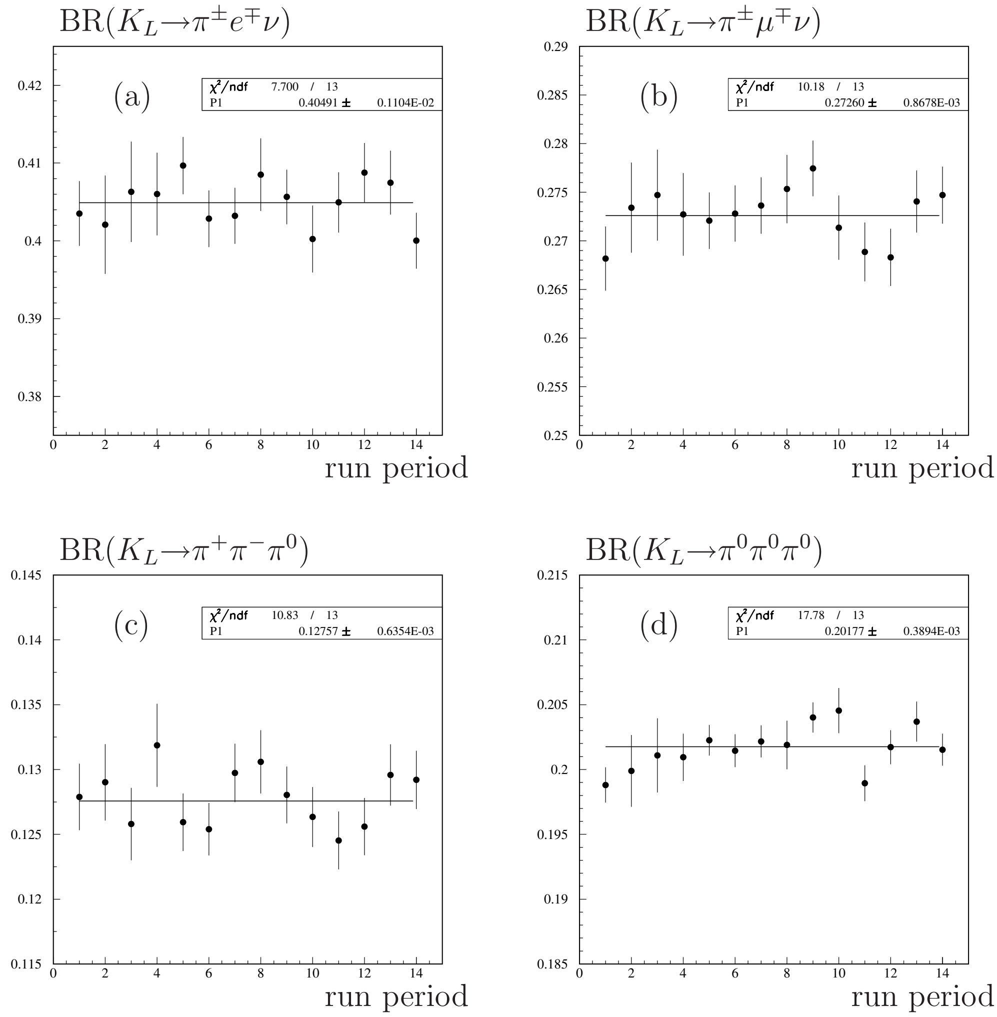

Fig. 51. Branching ratio results vs. run period for (a) $K_L \to \pi^\pm e^\mp \nu$, (b) $K_L \to \pi^\pm \mu^\mp \nu$, (c) $K_L \to \pi^0 \pi^0 \pi^0$, and (d) $K_L \to \pi^+ \pi^- \pi^0$ decays. The error bars illustrate only the uncorrelated statistical errors for each run period.

tion to that from signal statistics, with both sources contributing about equally to the total statistical error. The systematic-statistical error includes the statistical uncertainties associated with the determination of the various corrections. The correlated systematic error includes all contributions to the uncertainties on the branching ratios that are 100% correlated between channels, such as the uncertainty in the value of the K_L lifetime.

The sum of all of the measured branching ratios listed above, plus the sum of the PDG values for the decays to $\pi^+\pi^-$, $\pi^0\pi^0$, and $\gamma\gamma$ (0.0036) [1], is $1.0104 \pm 0.0018_{\mathrm{stat}} \pm 0.0074_{\mathrm{syst}}$, where the result, as remarked earlier, depends on the K_L lifetime.

10.2 K_L branching ratios and lifetime

The dependence of the absolute branching ratios on the K_L lifetime can be exploited to obtain a value for the K_L lifetime by normalizing the sum of the measured branching ratio values to unity (see Eq.5):

$$\tau_{K_L} = 50.72 \pm 0.11_{\mathrm{stat}} \pm 0.13_{\mathrm{syst-stat}} \pm 0.33_{\mathrm{syst}} \text{ ns.}$$

Alternately, normalizing the sum of the branching ratio measurements to $1 - 0.0036 = 0.9964$ removes the dependence on the K_L lifetime and gives the following values for the individual branching ratios:

$$\begin{aligned}
&\mathrm{BR}(K_L \to \pi^\pm e^\mp \nu) = \\
&\qquad 0.4007 \pm 0.0005_{\mathrm{stat}} \pm 0.0004_{\mathrm{syst-stat}} \pm 0.0014_{\mathrm{syst}}, \\
&\mathrm{BR}(K_L \to \pi^\pm \mu^\mp \nu) = \\
&\qquad 0.2698 \pm 0.0005_{\mathrm{stat}} \pm 0.0004_{\mathrm{syst-stat}} \pm 0.0014_{\mathrm{syst}}, \\
&\mathrm{BR}(K_L \to \pi^0\pi^0\pi^0) = \\
&\qquad 0.1997 \pm 0.0003_{\mathrm{stat}} \pm 0.0004_{\mathrm{syst-stat}} \pm 0.0019_{\mathrm{syst}}, \\
&\mathrm{BR}(K_L \to \pi^+\pi^-\pi^0) = \\
&\qquad 0.1263 \pm 0.0004_{\mathrm{stat}} \pm 0.0003_{\mathrm{syst-stat}} \pm 0.0011_{\mathrm{syst}}.
\end{aligned}$$

With this normalization, the complete error matrix is:

$$\begin{pmatrix}
K_L \to \pi^\pm e^\mp \nu & K_L \to \pi^\pm \mu^\mp \nu & K_L \to \pi^+\pi^-\pi^0 & K_L \to \pi^0\pi^0\pi^0 & \tau_{K_L}(\mathrm{ns}) \\
2.39 \times 10^{-6} & -0.57 \times 10^{-6} & -0.12 \times 10^{-6} & -1.71 \times 10^{-6} & 1.36 \times 10^{-4} \\
 & 2.17 \times 10^{-6} & -0.35 \times 10^{-6} & -1.26 \times 10^{-6} & 1.17 \times 10^{-4} \\
 & & 1.39 \times 10^{-6} & -0.91 \times 10^{-6} & -1.64 \times 10^{-4} \\
 & & & 3.88 \times 10^{-6} & -1.49 \times 10^{-4} \\
 & & & & 1.27 \times 10^{-1}
\end{pmatrix}$$

The ratio $\mathrm{BR}(K_L{\to}\pi^\pm e^\mp\nu)/\mathrm{BR}(K_L{\to}\pi^\pm\mu^\mp\nu)$ can be predicted from the measurement of the form factor slopes assuming the universality of the weak couplings for electrons and muons. From our branching ratio measurements, we obtain

$$\mathrm{BR}(K_L \to \pi^\pm e^\mp \nu)/\mathrm{BR}(K_L \to \pi^\pm \mu^\mp \nu) = 1.485 \pm 0.013,$$

to be compared with the expected value of

$$\mathrm{BR}(K_L \to \pi^\pm e^\mp \nu)/\mathrm{BR}(K_L \to \pi^\pm \mu^\mp \nu) = 1.506 \pm 0.009$$

obtained using the average of the KTeV and ISTRA+ measurements of the form factor slopes (see next section).

The ratio $\mathrm{BR}(K_L \to \pi^0\pi^0\pi^0)/\mathrm{BR}(K_L \to \pi^+\pi^-\pi^0)$ can be evaluated from the determination of the isospin amplitudes based on measurements of the branching ratios and Dalitz-plot slopes for $K \to 3\pi$ decays. We obtain

$$\mathrm{BR}(K_L \to \pi^0\pi^0\pi^0)/\mathrm{BR}(K_L \to \pi^+\pi^-\pi^0) = 1.582 \pm 0.027,$$

to be compared with the prediction of Ref. 16

$$\mathrm{BR}(K_L \to \pi^0\pi^0\pi^0)/\mathrm{BR}(K_L \to \pi^+\pi^-\pi^0) = 1.579$$

10.3 $|V_{us}|$ determination

Measurements of $|V_{us}|$ and $|V_{ud}|$ provide the most precise test of the unitarity of the CKM mixing matrix, $|V_{ub}|$ contributing only at the level of 10^{-5}. $|V_{us}|$ is proportional to the square root of the partial width for semileptonic kaon decays. Many other factors enter into the calculation of $|V_{us}|$ as well [17]:

$$|V_{us}| \times f_+^{K^0}(0) = \left[\frac{192\,\pi^3\Gamma}{G^2M^2\,S_{\mathrm{ew}}\,I_i(\lambda'_+, \lambda''_+\lambda_0, 0)}\right]^{1/2} \times \frac{1}{1+\delta^i_{\mathrm{em}}+\Delta I_i/2}$$

where $f_+^{K^0}$ is the normalization of the form factors at zero momentum transfer, and $I_i(\lambda', \lambda'', \lambda_0)$ is the integral of the phase space density, factoring out $f_+^{K^0}$ and without radiative corrections. Short distance radiative corrections are in the universal term S_{ew} [18]. In addition, long distance radiative corrections [19,20] to the form factor and phase-space density are included as δ^i_{em} and $\Delta I_i(\lambda)$. λ' and λ'' are the slope and curvature of the vector form factor f_+. λ_0 is the slope of the scalar form factor. Using the values $\lambda'_+ = 0.0221 \pm 0.0011$, $\lambda''_+ = 0.0023 \pm 0.0004$ and $\lambda_0 = 0.0154 \pm 0.0008$, from KTeV [21], we obtain

$$f_+^{K^0} \times |V_{us}| = 0.2160 \pm 0.0011 \text{ from } K_{e3},$$
$$f_+^{K^0} \times |V_{us}| = 0.2170 \pm 0.0011 \text{ from } K_{\mu 3}.$$

A precise estimate of $f_+^{K^0}(0)$, 0.961 ± 0.008, was first given in 1984 [22]. More recent estimates are subject to large uncertainties [23,20]. Very recently however, lattice calculations [24] have given $f_+^{K^0}(0) = 0.960 \pm 0.009$, in excellent agreement with Ref. 22. Using the value from Ref. 22, we find:

$$|V_{us}| = 0.2250 \pm 0.0025 \text{ from } K_{e3},$$
$$|V_{us}| = 0.2260 \pm 0.0026 \text{ from } K_{\mu 3}.$$

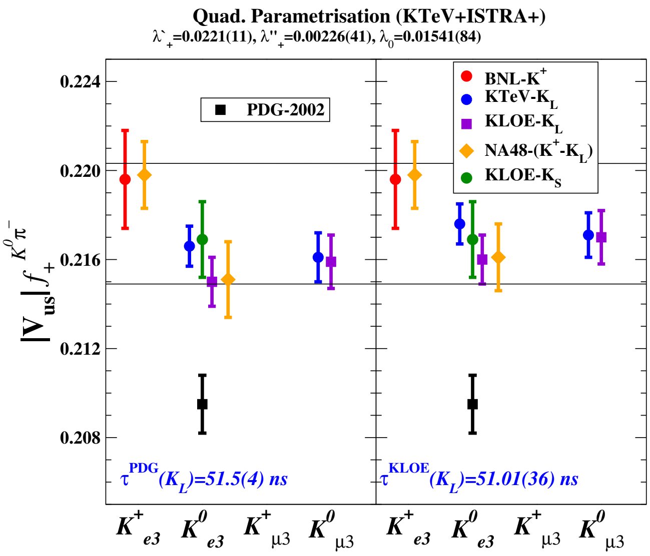

Fig. 52. KLOE results for $V_{us} \times f_+^{K^0}(0)$ from semileptonic decays of K_S [26] and K_L mesons. The recent KTeV results [21] are also shown.

The average of the above values is 0.2255±0.0022, taking into account the fact that the full error on $f_+^{K^0}$ must be used for the mean. This result can be compared with the value 0.2265±0.0021 obtained from unitarity if $V_{ud} = 0.9740 \pm 0.005$ [25].

11 Conclusions

Figure 5 summarizes KLOE results for the value of the product $V_{us} \times f_+^{K^0}(0)$ (see also Ref. 26), together with the results published recently by the KTeV collaboration [21]. The violation of unitarity in the first row of the CKM matrix suggested by the value for BR(K_{e3}) in the PDG listings [1] is no longer evident. We eagerly await improved estimates of the value of the form factor at $t = 0$. There are still questions surrounding the form factor parameters, λ. We have used the average of the KTeV [27] and ISTRA+ [28] values for the form factors. The recent form-factor measurements by NA48 [29] are not precise enough to disprove the existence of a $(\lambda''/2)(t/m_\pi^2)$ term.

Acknowledgements

We wish to thank Federico Mescia and Gino Isidori for their help throughout this work.

References

[1] Particle Data Group, K. Hagiwara, et al., Phys. Rev. D 66 (2002) 010001.

[2] KTeV Collaboration, T. Alexopolous, et al., Phys. Rev. D 70 (2004) 092006.

[3] NA48 Collaboration, A. Lai, et al., Phys. Lett. B 602 (2004) 41.

[4] F. Ambrosino, et al., Data handling, reconstruction, and simulation for the KLOE experiment, Nucl. Instrum. Meth. A 534 (2004) 403.

[5] C. Gatti, MC generators for radiative kaon decays, KLOE Note 194 (2004).
URL http://www.lnf.infn.it/kloe/pub/knote/kn194.ps

[6] M. Antonelli, M. Dreucci, Measurement of the K^0 mass from $\phi \to K_S K_L, K_S \to \pi^+\pi^-$, KLOE Note 181 (2002).
URL http://www.lnf.infn.it/kloe/pub/knote/kn181.ps

[7] T. Spadaro, C. Gatti, Measurement of BR($K_S \to \pi e \nu$), KLOE Note 176 (2002).
URL http://www.lnf.infn.it/kloe/pub/knote/kn176.ps

[8] M. Adinolfi, et al., The KLOE electromagnetic calorimeter, Nucl. Instrum. Meth. A 482 (2002) 364.

[9] M. Adinolfi, et al., The trigger system of the KLOE experiment, Nucl. Instrum. Meth. A 492 (2002) 134.

[10] A. Antonelli, et al., The KLOE field map revisited, KLOE Memo 233 (2001).

[11] M. Jelasity, J. Dombi, Artificial Intelligence 99 (1998) 1.

[12] M. Testa, Some thesis on K_L decays **update when available**, PhD thesis, Università di Roma La Sapienza (in preparation).

[13] J. Schwindling, B. Mansoulié, O. Couet, Using multi-layer perceptrons in PAW (1999).
URL http://cern.ch/paw/mlpfit/pawmlp.html

[14] KLOE Collaboration, Measurement of the K_L meson lifetime with the KLOE detector, hep-ex/0507088.

[15] K. G. Vosburgh, et al., Phys. Rev. D 6 (1972) 1834.

[16] J. Bijnens, F. Borg, Eur. Phys. J. C 40 (2005) 383.

[17] M. Battaglia, et al., The CKM Matrix and the Unitarity Triangle, Proceedings of the Workshop on the CKM Unitarity Triangle, Geneva, Switzerland, February 13–16, 2002, CERN report 2003-002, hep-ph/0304132 (2003).

[18] A. Sirlin, Nucl. Phys. B 196 (1982) 83.

[19] V. Cirigliano, et al., Eur. Phys. J. C 23 (2002) 121.

[20] V. Cirigliano, H. Neufeld, H. Pichl, Eur. Phys. J. C 35 (2004) 53.

[21] KTeV Collaboration, T. Alexopolous, et al., Phys. Rev. Lett. 93 (2004) 181802.

[22] H. Leutwyler, M. Roos, Z. Phys. C 25 (1984) 91.

[23] J. Bijnens, P. Talavera, Nucl. Phys. B 669 (2003) 341.

[24] D. Becirevic, et al., Nucl. Phys. B 705 (2005) 339.

[25] A. Czarnecki, W. J. Marciano, A. Sirlin, Phys. Rev. D70 (2004) 093006.

[26] KLOE Collaboration, A. Aloisio, et al., Measurement of the branching ratio for the decay $K_S \to \pi^{\pm} e^{\mp} \bar{\nu}(\nu)$ with the KLOE detector, Contributed paper to the 32nd International Conference on High Energy Physics (ICHEP), 16–22 August 2004, Beijing, China, paper number 8-0811 (2004).
URL http://ichep04.ihep.ac.cn/papers.htm

[27] KTeV Collaboration, T. Alexopolous, et al., Phys. Rev. D 70 (2004) 092007.

[28] O. P. Yushchenko, et al., Phys. Lett. B 589 (2004) 111.

[29] NA48 Collaboration, A. Lai, et al., Phys. Lett. B 606 (2004) 1.

A Agreement of kinematic distributions for data and Monte Carlo

The data-Monte Carlo agreement between the distributions for several kinematic variables has been checked for events in which the $K_L$decays into charged particles. events. Overall, good agreement is observed. Some examples of such comparisons are shown here.

The distributions of the transverse and total momentum of charged secondaries from K_L decay are shown in Fig. A.1. Figure A.2 shows the distribution of the polar angle and the track length for such particles. The distribution of the angle between the particles and the two-track invariant mass in the electron mass hypothesis are shown in Fig. A.3.

B Additional test of tracking efficiency systematics

An additional test has been performed to investigate the robustness of the evaluation of the systematic uncertainty on the tracking efficiency. Corrections to the Monte Carlo tracking efficiency value have been obtained from data using control samples (see Sec. 6.2). The results show that the correction value depends on the particle momentum. Therefore, the tracking efficiency has been evaluated by folding the correction with the momentum distributions of the K_L decay products.

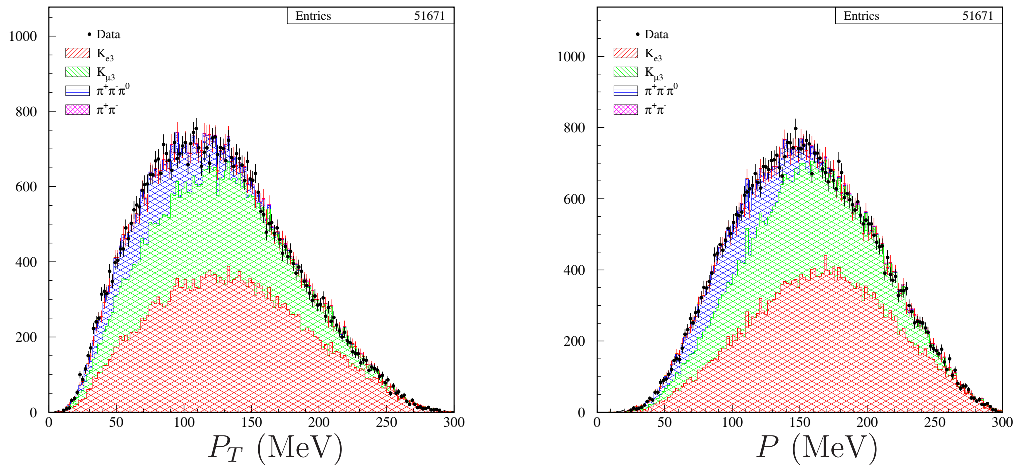

Fig. A.1. Total (left) and transverse (right) momentum distributions for charged secondaries from K_L decay, for data and Monte Carlo.

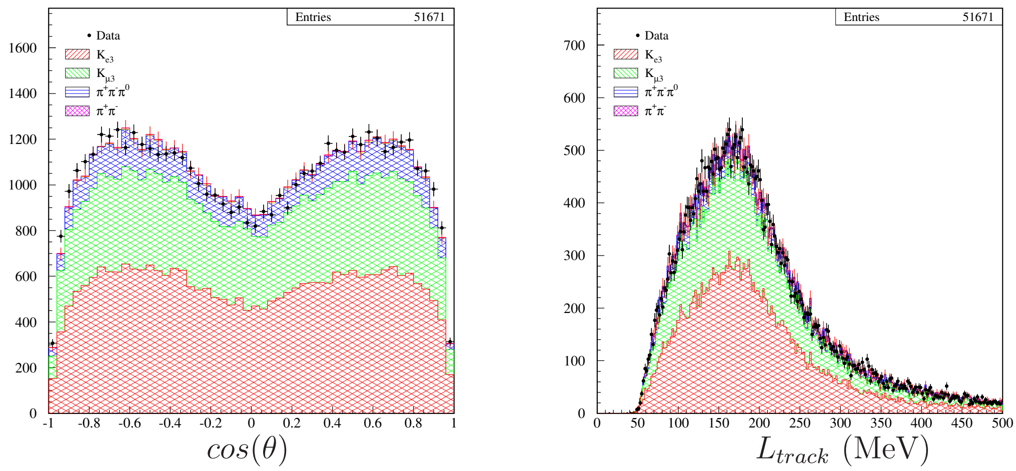

Fig. A.2. Polar angle (left) and track-length (right) distributions for charged secondaries from K_L decay, for data and Monte Carlo.

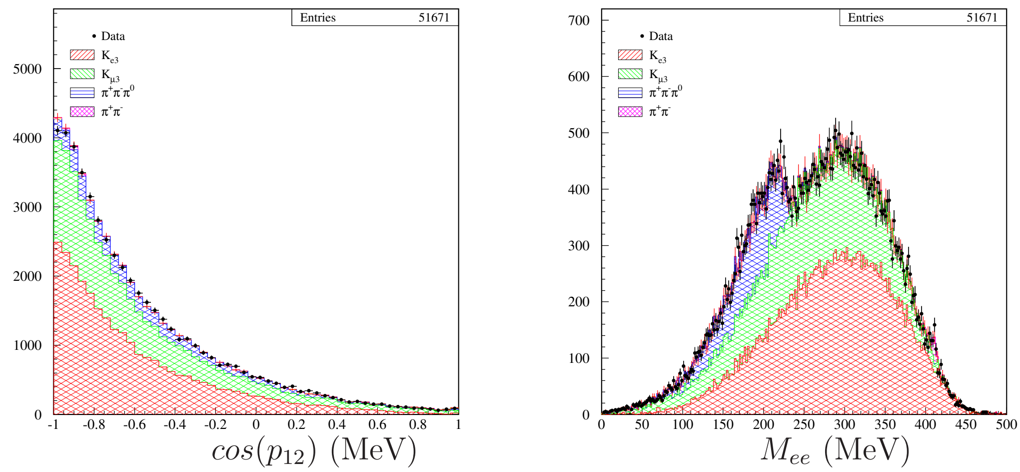

Fig. A.3. Distribution of the opening angle between tracks for charged secondaries from K_L decay (left), and the invariant mass for such track pairs calculated in the electron mass hypothesis (right), for data and Monte Carlo.

This method accounts for the main dependence of the correction. The systematic uncertainty due to minor dependences has been evaluated by studying the stability of the result when the definition of the track acceptance cuts is changed (see Sec. 9.3).

The uncertainty due to this effect is expected to be of the order of:

$$\delta\varepsilon = |(\varepsilon_{\rm true}^{\rm MC} - \varepsilon_{\rm cs}^{\rm MC}) \times \frac{\varepsilon_{\rm cs}^{\rm MC} - \varepsilon_{\rm cs}^{\rm data}}{\varepsilon_{\rm cs}^{\rm MC}}|$$

where $\varepsilon_{\rm true}^{\rm MC}$ is the efficiency for the Monte Carlo sample used for the analysis and $\varepsilon_{\rm cs}^{\rm MC(data)}$ is the efficiency for the MC (data) control sample. The formula given above is not sufficient for the evaluation of the systematic uncertainty because there might be cancellation effects that make the value of $\varepsilon_{\rm cs}^{\rm MC}$ close to that of $\varepsilon_{\rm true}^{\rm MC}$. The value of $\delta\varepsilon$ represents a lower limit on the systematic uncertainty evaluated in Sec. 9.3.

The value of the efficiency as a function of particle momentum is shown in Fig. B.1 for $K_L \to \pi^\pm e^\mp \nu$, $K_L \to \pi^\pm \mu^\mp \nu$, $K_L \to \pi^+\pi^-\pi^0$, and the control sample.

Figure B.2 shows the value $\delta\varepsilon$ as a function of track momentum weighted with the momentum distributions for $K_L \to \pi^\pm e^\mp \nu$, $K_L \to \pi^\pm \mu^\mp \nu$, and $K_L \to \pi^+\pi^-\pi^0$.

The value of $\delta\varepsilon$ is smaller than 10^{-4} for $K_L \to \pi^\pm e^\mp \nu$, 2×10^{-4} for $K_L \to \pi^\pm \mu^\mp \nu$, and 10^{-3} for $K_L \to \pi^+\pi^-\pi^0$. These values are smaller than the systematic uncertainties evaluated in Sec. 9.3. The largest value of $\delta\varepsilon$ is seen for $K_L \to \pi^+\pi^-\pi^0$ at low momentum where the tracking efficiency is low, and both the

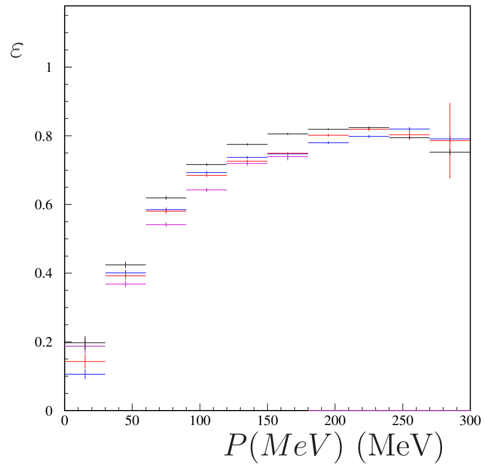

Fig. B.1. Tracking efficiency as a function of particle momentum for $\pi^{\pm}e^{\mp}\nu$ (red), $\pi^{\pm}\mu^{\mp}\nu$ (blue), $\pi^{+}\pi^{-}\pi^{0}$ (pink), and control (black) samples.

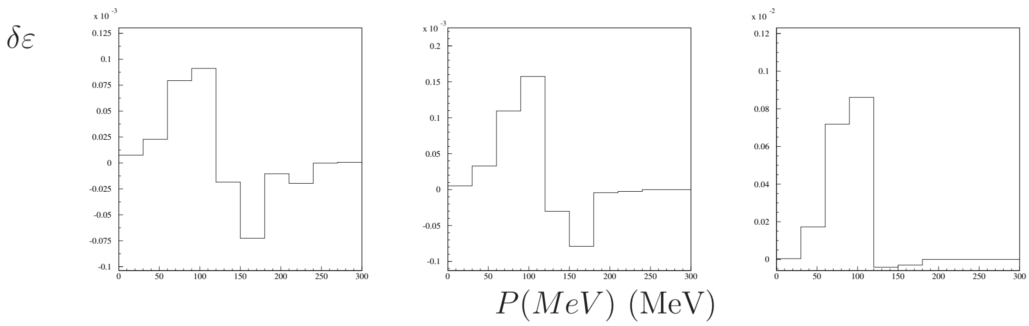

Fig. B.2. $\delta\varepsilon$ as a function of particle momentum for $\pi^{\pm}e^{\mp}\nu$, $\pi^{\pm}\mu^{\mp}\nu$, and $\pi^{+}\pi^{-}\pi^{0}$, from left to right.

value of $|(\varepsilon^{\text{MC}}_{\text{true}} - \varepsilon^{\text{MC}}_{\text{cs}})|$ and the value of the tracking efficiency correction are large (see Sec. 6.2).

C Evaluation of the error matrix

We measure the four dominant K_L absolute branching ratios, $BRa|_{\tau=51.54\ ns}$ with error matrix δBRa_{ij} , and we wish to transform to branching ratio measurements BR with the constraint $\sum BR = 1$ and lifetime τ:

$$BR_i = \frac{BRa_i}{\sum_i BRa_i}; \qquad \tau = 51.54 - \frac{\sum_i BRa_i - 1}{0.0128}$$

The transformation matrix is:

$$T = \begin{pmatrix} \frac{dB_1}{dBa_1} & \frac{dB_2}{dBa_1} & \frac{dB_3}{dBa_1} & \frac{dB_4}{dBa_1} & \frac{d\tau}{dBa_1} \\ \frac{dB_1}{dBa_2} & \frac{dB_2}{dBa_2} & \frac{dB_3}{dBa_2} & \frac{dB_4}{dBa_2} & \frac{d\tau}{dBa_2} \\ \frac{dB_1}{dBa_3} & \frac{dB_2}{dBa_3} & \frac{dB_3}{dBa_3} & \frac{dB_4}{dBa_3} & \frac{d\tau}{dBa_3} \\ \frac{dB_1}{dBa_4} & \frac{dB_2}{dBa_4} & \frac{dB_3}{dBa_4} & \frac{dB_4}{dBa_4} & \frac{d\tau}{dBa_4} \end{pmatrix}$$

The error matrix δB for the new set of measurements is derived from:

$$\delta B = T^T \delta Ba T$$

Using the values of BRa and δBRa_{ij} given in Secs. 9 and 10.1 we obtain:

$$\begin{pmatrix} K_L \to \pi^{\pm} e^{\mp} \nu & K_L \to \pi^{\pm} \mu^{\mp} \nu & K_L \to \pi^{+} \pi^{-} \pi^{0} & K_L \to \pi^{0} \pi^{0} \pi^{0} & \tau_{K_L}(\mathrm{ns}) \\ 2.39 \times 10^{-6} & -0.57 \times 10^{-6} & -0.12 \times 10^{-6} & -1.71 \times 10^{-6} & 1.36 \times 10^{-4} \\ & 2.17 \times 10^{-6} & -0.35 \times 10^{-6} & -1.26 \times 10^{-6} & 1.17 \times 10^{-4} \\ & & 1.39 \times 10^{-6} & -0.91 \times 10^{-6} & -1.64 \times 10^{-4} \\ & & & 3.88 \times 10^{-6} & -1.49 \times 10^{-4} \\ & & & & 1.27 \times 10^{-1} \end{pmatrix}$$